



**IDENTIFYING HIGH-TRAFFIC PATTERNS IN THE WORKPLACE WITH
RADIO TOMOGRAPHIC IMAGING IN 3D WIRELESS SENSOR NETWORKS**

THESIS

Thea S. Danella, Captain, USAF

AFIT-ENG-14-M-24

**DEPARTMENT OF THE AIR FORCE
AIR UNIVERSITY**

AIR FORCE INSTITUTE OF TECHNOLOGY

Wright-Patterson Air Force Base, Ohio

DISTRIBUTION STATEMENT A:
APPROVED FOR PUBLIC RELEASE; DISTRIBUTION UNLIMITED

The views expressed in this thesis are those of the author and do not reflect the official policy or position of the United States Air Force, the Department of Defense, or the United States Government.

This material is declared a work of the U.S. Government and is not subject to copyright protection in the United States.

AFIT-ENG-14-M-24

IDENTIFYING HIGH-TRAFFIC PATTERNS IN THE WORKPLACE WITH RADIO
TOMOGRAPHIC IMAGING IN 3D WIRELESS SENSOR NETWORKS

THESIS

Presented to the Faculty
Department of Electrical and Computer Engineering
Graduate School of Engineering and Management
Air Force Institute of Technology
Air University
Air Education and Training Command
in Partial Fulfillment of the Requirements for the
Degree of Master of Science in Electrical Engineering

Thea S. Danella, B.S.E.E.

Captain, USAF

March 2014

DISTRIBUTION STATEMENT A:
APPROVED FOR PUBLIC RELEASE; DISTRIBUTION UNLIMITED

AFIT-ENG-14-M-24

IDENTIFYING HIGH-TRAFFIC PATTERNS IN THE WORKPLACE WITH RADIO
TOMOGRAPHIC IMAGING IN 3D WIRELESS SENSOR NETWORKS

Thea S. Danella, B.S.E.E.
Captain, USAF

Approved:

//signed//
Richard K. Martin, PhD (Chairman)

11 March 2014
Date

//signed//
Julie A. Jackson, PhD (Member)

11 March 2014
Date

//signed//
Michael A. Temple, PhD (Member)

11 March 2014
Date

Abstract

The rapid progress of wireless communication and embedded micro-sensing electro-mechanical systems (MEMS) technologies has resulted in a growing confidence in the use of wireless sensor networks (WSNs) comprised of low-cost, low-power devices performing various monitoring tasks. Radio Tomographic Imaging (RTI) is a technology for localizing, tracking, and imaging device-free objects in a WSN using the change in received signal strength (RSS) of the radio links the object is obstructing. This thesis employs an experimental indoor three-dimensional (3-D) RTI network constructed of 80 wireless radios in a 100 square foot area. Experimental results are presented from a series of stationary target localization and target tracking experiments using one and two targets. Preliminary results demonstrate a 3-D RTI network can be effectively used to generate 3-D RSS-based images to extract target features such as size and height, and identify high-traffic patterns in the workplace by tracking asset movement.

Acknowledgments

I'd like to thank my family and especially my husband for all their love, support, and patience through every late night and 12-hour day, they kept me motivated and focused. I also want to thank my friends for all of the love and laughter; both new and old. They provided much needed distraction, and made this process a little bit easier and all the more enjoyable. It is because of my friends and family that I am the person I am today, and I am so blessed to have every one of them in my life. I want to also thank my advisor, Dr. Richard K. Martin, and fellow student, Mr. Jason Pennington. They were critical in my success; with their guidance I learned more than I ever expected to and can say I have successfully completed this journey. Lastly, thank you to the sponsors

Thea S. Danella

Table of Contents

	Page
Abstract	iv
Acknowledgments	v
Table of Contents	vi
List of Figures	viii
List of Tables	xi
List of Symbols	xii
List of Acronyms	xix
 I. Introduction	 1
1.1 Background	1
1.2 Radio Tomographic Imaging	2
1.3 Problem Statement	4
1.4 Thesis Structure	4
 II. Related Work	 6
2.1 Notational Conventions	7
2.2 Radio Frequency Device-Based Localization	7
2.2.1 Measurement Modality	8
2.2.2 Localization Methods	10
2.2.3 Limiting Factors	14
2.3 Self-Localization	15
2.4 Passive, Device-Free Localization	16
2.4.1 Ultra-Wideband Radar	17
2.4.2 Received Signal Strength Fingerprinting	18
2.4.3 Received Signal Strength Tomography	19
2.4.3.1 Linear Signal Propagation Model	22
2.4.3.2 Measurement Modalities	24
2.4.3.3 Weighting Models	29
2.4.3.4 Signal Recovery & Solving the Inverse, Ill-posed Problem	34
2.4.3.5 Cylindrical Human Model	43

	Page
2.4.3.6 Cramer-Rao Lower Bound	43
2.5 Chapter Summary	44
III. Methodology	45
3.1 Equipment and Tools	45
3.2 Assumptions	47
3.3 System Models	48
3.4 Network Setup	49
3.5 Choosing Model and Experiment Parameters	55
3.6 Simulated Truth Data	55
3.7 Experiment Design	63
3.8 Data Analysis	69
3.9 Chapter Summary	72
IV. Results and Discussion	73
4.1 Stationary Target Localization	73
4.2 Motion Tracking	102
4.3 Spatial Pattern Monitoring	108
4.4 Chapter Summary	117
V. Conclusion and Future Work	118
Bibliography	123

List of Figures

Figure	Page
1.1 Illustration of the links created in a RTI network.	3
2.1 ToA Trilateration.	11
2.2 TDoA Multilateration.	12
2.3 AoA Triangulation.	13
2.4 Illustration of the links created in a RTI network. $K=36$ nodes.	21
2.5 Illustration of a single obstructed link in an RTI network.	23
3.1 TelosB Mote.	46
3.2 Size Demonstration.	46
3.3 Experimental RTI network structure.	50
3.4 Aerial view of mote topology.	50
3.5 Lateral and three-dimensional views of mote topology.	51
3.6 Three-dimensional views of link coverage.	52
3.7 Two-dimensional views of link coverage.	53
3.8 \sqrt{CRLB} volume $[\frac{dB}{ft^2}]$	54
3.9 Analysis of the \sqrt{CRLB} along the vertical dimension.	55
3.10 Truth Images: Single Stationary Target.	58
3.11 Truth Images: Single Stationary Target.	59
3.12 Truth Images: Two Stationary Targets.	60
3.13 Truth Images: Two Stationary Targets.	61
3.14 2-D Truth Images: Triangular Motion Tracking.	62
3.15 True Path: Motion Tracking.	67
3.16 Truth Images: Motion Tracking and Spatial Pattern Monitoring	68
4.1 Part 1: 2-D Position and aerial attenuation images of a single stationary target. .	81

Figure	Page
4.2 Part 2: 2-D Position and aerial attenuation images of a single stationary target. .	82
4.3 Part 3: 2-D Position and aerial attenuation images of a single stationary target. .	83
4.4 Part 1: 2-D Lateral attenuation images of a single stationary target.	84
4.5 Part 2: 2-D Lateral attenuation images of a single stationary target.	85
4.6 3-D Position estimates of a single stationary target.	86
4.7 Part 1: 3-D attenuation images of a single stationary target.	87
4.8 Part 2: 3-D attenuation images of a single stationary target.	88
4.9 Part 1: Target height extraction using 2-D lateral attenuation images $\alpha = 150.0$. .	89
4.10 Part 2: Target height extraction using 3-D attenuation images $\alpha = 150.0$	90
4.11 Part 3: Target height extraction using 2-D aerial attenuation images $\alpha = 150.0$. .	91
4.12 Part 4: Target height and 3-D position estimates $\alpha = 150.0$	92
4.13 Part 5: Target height extraction using 2-D lateral attenuation images $\alpha = 500.0$. .	93
4.14 Part 6: Target height extraction using 3-D attenuation images $\alpha = 500.0$	94
4.15 Part 7: Target height extraction using 2-D lateral attenuation images $\alpha = 1000.0$. .	95
4.16 Part 8: Target height extraction using 3-D attenuation images, $\alpha = 1000.0$	96
4.17 2-D attenuation images of two stationary targets.	97
4.18 Estimate comparisons based on target location.	98
4.19 Part 1: Estimate comparisons with obstructions for $(x, y)_{sT} = (3, 6)$ ft.	99
4.20 Part 2: Estimate comparisons with obstructions for $(x, y)_{sT} = (7, 5)$ ft.	100
4.21 Part 3: Estimate comparisons with obstructions of two targets.	101
4.22 Single target motion tracking experiments: $\overline{NMS E_R}$	103
4.23 Estimates: Motion tracking $(x, y)_{mT,tri} = (2, 8) - (2, 2) - (8, 2)$	104
4.24 Estimates: Motion tracking $(x, y)_{mT,2} = (3, 4) - (7, 8)$	105
4.25 Estimates: Motion tracking $(x, y)_{mT,2} = (7, 3) - (7, 8)$	106
4.26 Histogram Results: Single target motion tracking.	107

Figure	Page
4.27 Spatial pattern monitoring with a single target: $\overline{NMS\bar{E}_R}$	110
4.28 Estimates & Histogram Results: Single target spatial pattern monitoring $(x, y)_{mT,1}$.	111
4.29 Estimates & Histogram Results: Single target spatial pattern monitoring $(x, y)_{mT,2}$.	112
4.30 Spatial pattern monitoring with two targets: $\overline{NMS\bar{E}_R}$	113
4.31 Spatial Pattern Monitoring: Comparison of $\overline{NMS\bar{E}_R}$	114
4.32 Image Estimates: Two-target spatial pattern monitoring	115
4.33 Histogram Results: Two-target spatial pattern monitoring	116

List of Tables

Table	Page
3.1 CRLB Construction Parameters.	53
3.2 Stationary Localization Experiments.	64
3.3 Motion Tracking Experiments.	65
3.4 Spatial Pattern Monitoring Experiments.	66
4.1 Stationary target experiments: $\bar{\epsilon}_{D,\alpha}$	74
4.2 Stationary target experiments: $\sigma_{\epsilon_D}^2$	76
4.3 Single target motion tracking experiments: \overline{NMSE}_R & $\sigma_{\overline{NMSE}_R}$	102

List of Symbols

Symbol	Definition
$\mathbf{0}$	Vector or Matrix of Zeros
A	Area (ft ²)
α	Tunable Regularization Parameter
β	Tunable <i>Total Variation Regularization</i> Sharpness Parameter
c	Speed of Light (m/s)
c_H	Center Cartesian Coordinates of Human Cylindrical Model (ft)
\mathbf{C}	Covariance Matrix [$M \times N$]
d	Distance (ft)
\mathbf{D}	Difference Operator Matrix [$M \times N$]
δ_c	Pixel or Voxel Correlation Constant (ft)
Δ	Change or Difference
Δ_p	Pixel or Voxel Side Length (ft)
$\mathbf{\Lambda}$	Diagonal Matrix of Singular Values (Non-negative Real Numbers) [$M \times N$]
ϵ_D	<i>Euclidean Distance</i> Position Estimate Error (ft)
η_p	Path Loss Parameter
F	Fading Loss from Constructive and Destructive Interference of Narrow-band Signals in a Multipath Environment (dB)

Symbol	Definition
γ	Tunable CRLB Surface Parameter
\mathbf{I}	Identity Vector or Matrix
J	Regularization Operator
\mathbf{J}	<i>Fisher Information Matrix</i>
k	Signal Channel
K	Number of Wireless Nodes
l	Link Counter
L	Static Loss Due to Distance, Antenna Patterns, Device Inconsistencies, etc... (dB)
L_x, L_y, L_z	Number of Pixels or Voxels in Respective Cartesian Dimension
λ	Width of Weighting Ellipse (ft)
λ_i	Diagonal Entries of $\mathbf{\Lambda}$ (Square Root of Non-zero Eigenvalue)
λ_T	Resource Monitoring Trip Frequency
m	Time Window Under Consideration
M	Number of Unique Two-way Links
μ	<i>Ledoit-Wolf Estimator</i> Identity Matrix Scaling Parameter
n	Node Counter
\mathbf{n}	Noise (dB) [$M \times 1$]
N	Number of Pixels or Voxels

Symbol	Definition
∇	Gradient
ν	<i>Ledoit-Wolf Estimator</i> Covariance Matrix Shrinkage Parameter
Ω	Signal Attenuation Weight Assigned to Pixel or Voxel (scalar)
p	Pixel or Voxel Counter
P	Signal Power (dB)
$p_X(x)$	Probability Density/Mass Function
$p_Y(y x)$	Conditional Probability Density/Mass Function
Π	Linear Transformation Matrix
Π_0	Power Loss (dB) at a Short Reference Distance, d_0 (ft)
\mathbf{Q}	<i>Tikhonov Regularization</i> Matrix Operator $[M \times N]$
r	RSS Measurement (dB)
R_H	Radius for Human Cylindrical Model (ft)
\mathbf{S}	Affected Pixel or Voxel Binary Selection Matrix $[M \times N]$
S	Shadowing Loss Due to Objects that Attenuate the Signal (dB)
σ^2	Variance (dB ²)
σ	Standard Deviation (dB)
Σ	Sum
t	Time

Symbol	Definition
t_f	Duration of Measurement Frame (s)
t_r	Time of Current Real-time Measurement (s)
t_c	Calibration Time Frame Measurement (s)
T	Time of Arrival (s)
u_i	Orthonormal Vector Entries of the Unitary Matrix \mathbf{U} (Eigenvector Corresponding to λ_i)
\mathbf{U}	Unitary Matrix $[M \times M]$
$\hat{\mathbf{U}}$	Intrinsic Subspace
$\tilde{\mathbf{U}}$	Extrinsic Subspace
ν	Measurement Noise (dB)
v_p	Propagation Speed (m/s)
\mathbf{V}	Unitary Matrix $[N \times N]$
\mathbf{W}	Transfer Matrix of Pixel or Voxel Signal Attenuation Weight Model Parameters, $\mathbf{\Omega} \cdot \mathbf{S} [M \times N]$
x	Pixel or Voxel Signal Attenuation (dB/ft)
\mathbf{x}	Collection of Pixel or Voxel Signal Attenuation (dB/ft) $[N \times 1]$
\mathbf{y}	Collection of Calibrated RSS Link Measurements (dB) $[M \times 1]$
$\hat{\mathbf{x}}$	Attenuation Image Estimate (dB/ft)
$\hat{\mathbf{y}}$	Intrinsic Signal Component

Symbol Definition

$\tilde{\mathbf{y}}$ Extrinsic Signal Component

Z Total Static Fading Loss (dB)

\sim Distributed As

(x, y) 2-D Cartesian Coordinates

(x, y, z) 3-D Cartesian Coordinates

$(\bar{\bullet})$ Ensemble or Sample Mean of the Argument

$(\hat{\bullet})$ Estimate of the Argument

$\|\bullet\|_{l_1}$ l_1 Norm of the Argument

$\|\bullet\|_{l_2}$ l_2 Norm or *Euclidean Distance* of the Argument (ft)

$\|\bullet\|_{weight}$ Weighted Least Squares of the Argument

$(\bullet)^{-1}$ Matrix or Vector Inverse of the Argument

$(\bullet)^T$ Matrix or Vector Transpose of the Argument

$f(\bullet)$ Objective Cost Function of the Argument

$Var(\bullet)$ Variance of the Argument

$Cov(\bullet)$ Covariance of the Argument

$\mathcal{N}(\bullet, \bullet)$ *Gaussian Distribution*

Symbol Definition

Subscripts

c	Calibration
$chan$	Channel
CHM	Cylindrical Human Model
D	Distance
E	Extrinsic
$fade$	Fade-Level
H	Human
i	Receiving Node
I	Intrinsic
j	Transmitting Node
k	Channel
l	Link
l_1	l_1 Norm
l_2	Euclidean Norm
mT	Moving Truth
mC	Clean Path
M	Number of Unique Two-way Links
n	Noise
N	Number of Wireless Nodes or Normalized
O	Obstructed
p	Pixel or Voxel
r	Real-time RSS Measurement
reg	Regularized Term
R	RSS or Real-Time

Symbol Definition

RLS Regularized Least Squares

sT Stationary Truth

SUB SubVRT Estimation

t time

T Transmit

TIK Tikhonov Regularization

WLS Weighted Least Squares

x Pixel or Voxel Signal Attenuation

X Transverse Horizontal Direction (width)

Y Horizontal Direction (depth)

Z Vertical Direction (height)

Superscripts

T matrix transpose

-1 matrix inverse

δ + or - Sign of Change

List of Acronyms

Acronym	Definition
2-D	two-dimensional
3-D	three-dimensional
AFIT	Air Force Institute of Technology
AFRL	Air Force Research Laboratory
AoA	Angle of Arrival
BPM	beats per minute
BSD	Berkely Software Distribution
CAT Scan	Computed Axial Tomography
CRLB	Cramer-Rao Lower Bound
CT	Computed Tomography
dB	decibels
DFL	Device-Free Localization
EM	electro-magnetic
FIM	Fisher Information Matrix
GHz	gigahertz
GPS	Global Positioning System
GUI	Graphical User Interface
ICD	Informed Consent Document
IEEE	Institute of Electrical and Electronics Engineers
IFA	Inverted-F Antenna
Inc.	Incorporated
IRB	Institutional Review Board
ISM	Industrial, Scientific and Medical

Acronym	Definition
ITU	International Telecommunication Union
kB	kilobyte
kbps	kilobits per second
LASSO	Least Absolute Shrinkage and Selection Operator
LOS	Line-of-Sight
mA	milliamp
MAP	Maximum A-posteriori Probability
MCL	Monte Carlo Localization
MCU	Microcontroller Unit
MEMS	Micro Electro-Mechanical Systems
MHz	megahertz
MIMO	Multiple Input, Multiple Output
MISO	Multiple Input, Single Output
MLE	Maximum Likelihood Estimate
MRI	Magnetic Resonance Imaging
MSE	Mean Squared Error
mW	milliwatt
NeSh	Network Shadowing
NLOS	Non-Line-of-Sight
NMSE	Normalized Mean Squared Error
OS	Operating System
PCA	Principal Component Analysis
PET	Positron Emission Tomography
PVC	Polyvinyl Chloride
PRR	Packet Reception Rate

Acronym	Definition
RAM	Random Access Memory
RF	Radio Frequency
RFIC	Radio Frequency Integrated Circuit
RFID	Radio Frequency Identification
RTI	Radio Tomographic Imaging
RSS	Received Signal Strength
RSSI	Received Signal Strength Indicator
SIMO	Single Input, Multiple Output
SISO	Single Input, Single Output
SMC	Sequential Monte Carlo
SNR	Signal to Noise Ratio
SOCHE	Southwestern Ohio Council for Higher Education
SPAN	Sensing and Processing Across Networks
SVD	Singular Value Decomposition
TDoA	Time Difference of Arrival
ToA	Time of Arrival
TSVD	Truncated Singular Value Decomposition
TV	Total Variation
UC	University of California
USB	Universal Serial Bus
UWB	Ultra-Wideband
VRTI	Variance-based Radio Tomographic Imaging
WSN	Wireless Sensor Network

IDENTIFYING HIGH-TRAFFIC PATTERNS IN THE WORKPLACE WITH RADIO TOMOGRAPHIC IMAGING IN 3D WIRELESS SENSOR NETWORKS

I. Introduction

THIS chapter provides background on the nature and application of Wireless Sensor Networks (WSNs) and Radio Tomographic Imaging (RTI). It describes the problem statement, assumptions, research objectives, a brief description of the approach used, and closes by describing the structure of this thesis.

1.1 Background

The rapid progress of wireless communication and embedded micro-sensing Micro Electro-Mechanical Systems (MEMS) technologies has resulted in a growing confidence in the use of low-cost, low-power wireless sensors in various monitoring tasks [1]. A WSN is a collection of Radio Frequency Integrated Circuits (RFICs) acting as nodes or connection points capable of sending, receiving, and forwarding information over a wireless communication channel. A variety of applications exists using WSNs supporting both civilian and military needs each of which can be categorized into one of the following areas: quality and inventory monitoring, surveillance, classification, and localization. Such networks are mobile, highly flexible, and easily implemented due to their low cost and relatively low sustainment needs. WSNs are comprised of densely populated sensor nodes deployable in large numbers, and are capable of instrumenting the surrounding environment via wireless communication [2].

1.2 Radio Tomographic Imaging

There exist various methods for implementing WSNs. This paper focuses on the use of Received Signal Strength (RSS) measurements from a network of RFICs. In an established WSN, sensor nodes are deployed in an estimated or known topology. They transmit non-specific Radio Frequency (RF) signals across the network to each of the other nodes via a wireless communication “link.” An illustration can be seen in Figure 1.1. A single radio connected to a computer acts as a basestation. It listens to network traffic and records RSS measurements for processing. The area of interest is initially calibrated by recording RSS measurements of the empty network—free of targets. This means the area may include walls and furniture if they are a permanent fixture; this is the topography of the area. As a result of permanent obstructions, links can be Line-of-Sight (LOS) or Non-Line-of-Sight (NLOS). Following calibration, the network monitors the changes in RSS over time [3]. When a physical change is introduced into the WSN (i.e., a person walks in), each signal passing through the obstruction is essentially interrupted; each affected signal is attenuated and the signal’s RSS is reduced [3, 4]. The difference in RSS between the current and calibrated network is then used to image the area using a color-map where each color represents an RSS intensity. This process is known as Radio Tomographic Imaging (RTI). In a WSN, the encompassed area is divided into a grid consisting of pixels (two-dimensional (2-D)) or voxels (three-dimensional (3-D)). The objective of an RTI system is to estimate a discretized attenuation field using the difference in RSS from a real-time measurement versus the calibration measurement [5].

RTI networks rely on changes in the established environment to locate and monitor movement, and they can do so without requiring people to actively participate in the network or to wear a device [6]. This is greatly beneficial in situations where it may be invasive or uncomfortable for an individual to wear a device, such as in an elderly person’s home, a retirement community, or a hospital [7–9]. Likewise, the nature of an RTI

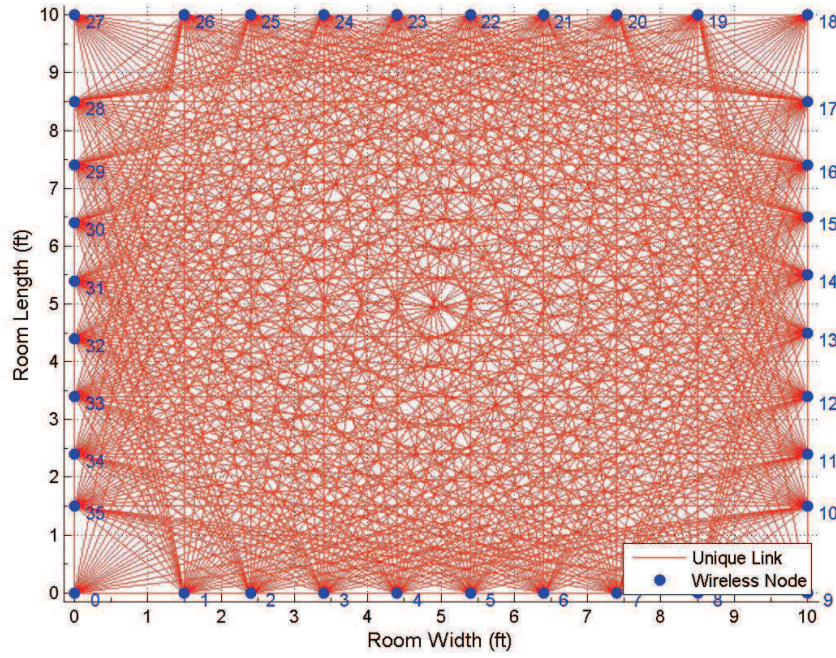


Figure 1.1: Illustration of the links created in a RTI network.

image illustrates the location and movement of an obstruction but cannot be used to identify detailed features of an obstruction. This is important in situations where privacy concerns exist. Additionally, in networks used for security, persons of interest seek to avoid being detected and therefore try to minimize their presence [10]. While in emergency response situations, it is necessary to locate humans and falling obstructions with ad-hoc networks where it would be impossible to provide rescue assets with a device [11].

As opposed to optical or infrared imaging systems, RTI is advantageous because RF signals can travel through obstructions such as walls, trees, and smoke, and do not require a well lit environment [12]. Technologies like GPS and active RF are limited by the need for persons to carry an electronic device [13, 14]. Other technologies that have been used in this area are related to classical multi-static radar tracking and Multiple Input,

Multiple Output (MIMO) radar; these systems generally require substantial infrastructures and would not be feasible [10].

RTI is an effective and efficient means of providing a situational awareness picture to aid personnel in making safe, informed decisions on how to act in an unsafe or dangerous situation such as a fire, natural disaster, hostage situation, or terrorist attack.

1.3 Problem Statement

Can an indoor 3-D RTI network be used to monitor resource usage within a room and extract target features?

In today's fiscal environment, it is critical to find ways to become a leaner workforce while not compromising mission effectiveness. It is a time where less has to be more, and efficient use of space and resources is a must. The purpose of this research is to understand and present the effectiveness and limitations of an indoor RTI network as a means to monitor resource usage, by tracking movement within an area. Data are presented using a series of images and histograms illustrating observed movement patterns such that an informed decision can be made to rearrange, remove, or relocate equipment and furniture within a work-space. Additional results include the analysis of 2-D lateral and 3-D attenuation images of targets with various heights to identify target height, size, and density.

1.4 Thesis Structure

The remainder of this document is organized into four chapters. Chapter Two (II) provides a comprehensive literature review of related work in the area of WSNs and RTI. Chapter Three (III) describes the methodology that will be used in this research, and the details of simulation and experiment setup. Chapter Four (IV) contains simulated and experimental results, and the analytic discussion of those results relative to the problem statement. Chapter Five (V), the final chapter, summarizes this research through a

discussion of the significance of what was accomplished and provides recommendations for additional areas to be explored in the future.

II. Related Work

THIS chapter provides an introduction to the theory and history of various RF-based localization methods and the background of RTI. Research efforts have expanded the world of RF-based localization; and as a result have opened the realm of RTI. The use of RF as a medium in these applications is appealing due to the low maintenance and cost requirements. Possible applications for RTI in security, surveillance, and emergency response have triggered growing interests to improve the cost, accuracy, efficiency, and simplicity of employing WSNs. More recently, research has illustrated the effectiveness of using RF-based localization to not only locate an emitting target, but also to locate and track the position and motion of a passive, device-free target also known as Device-Free Localization (DFL). Research areas needed to bolster employing RTI consist of exploring signal propagation in various environments, measurement modalities, weighting models, and estimation techniques along with regularization methods needed to counteract the sparsity and ill-posed nature of RTI. In the latter half of this chapter, a focus is placed on exploring the umbrella of linearly modeled RTI following the discussion of topics including traditional source localization, self-localization, and comparable DFL systems. Each of the various models that form the RTI problem are discussed to provide a breadth of knowledge; however, models used in this research include the *Linear Signal Propagation Model* as a system and measurement model, the *Line Model* for the purpose of attenuation weighting, and *Regularized Least Squares* with *Tikhonov Regularization* for image estimation and reconstruction.

Localization, also known as geolocation, is the process of determining the real-world geographic location of an object or person. It is a relatively mature field, and is continuing to adapt with changing technologies and new, dynamic approaches. RF geolocation can be discussed in three ways: locating and tracking an active RF emitting

source; network self-localization; and locating and tracking a passive, device-free target. Traditional localization techniques such as video, pressure, infrared, and ultrasound, are generally not feasible for the applications discussed earlier due to large support, energy, and cost requirements [14, 15]. More specifically, in particular applications envisioned to benefit from RF localization, it may not be practicable to include a Global Positioning System (GPS) receiver on each sensor or emitting source, and it would defeat the benefits and purpose of passive, device-free localization [7–9].

2.1 Notational Conventions

Throughout the paper, $(\cdot)^{-1}$ and $(\cdot)^T$ denotes a matrix, or vector, inverse and transpose respectively. A hat (e.g. \hat{x}) indicates an estimate of its argument and a bar (e.g. \bar{x}) represents the ensemble or sample mean of the argument. All column vectors are indicated with **bold** lower case letters, row vectors are denoted with a transpose operator, and matrices are denoted by capital **BOLD** letters.

2.2 Radio Frequency Device-Based Localization

There are many ways to localize an RF emitting source which is known as source localization or device-based localization. This process is often thought of in the more specific context of radio-location. As opposed to radio-navigation, where radio waves are used to actively seek one’s own position, radio-location refers to determining the location of an object or person who is emitting radio waves. Radio-location is most commonly seen in cellular telephone networks and through the use of GPS. Device-based source localization generally uses one or a combination of common measurement methods consisting of Time of Arrival (ToA), Time Difference of Arrival (TDoA), Angle of Arrival (AoA), and RSS information. These measurements are then utilized in one of four common techniques: trilateration, multilateration, triangulation, and Received Signal Strength Indicator (RSSI) [16]. Furthermore, RF device-based localization can be separated into two cases: the

active case where the source is actively participating or willing to be located and is cooperating with the system, or the passive case, when the source is not cooperating with the system such that it does not know it is being tracked or has no desire to be tracked [17]. As far as models and techniques are concerned, they can be applied similarly for each case, and therefore the following discussion is presented in a generic manner. Lastly, a brief description of the respective limiting factors attributed to these measurements and techniques is provided.

2.2.1 Measurement Modality.

Many measurements can be made during the transmission of a signal from a transmitter to a receiver. These measurement modalities are not limited to RF signals, and can provide useful information on other sensor media including electromagnetic, acoustic, and optical.

Time of Arrival. The first is the ToA, which is the absolute arrival time of a transmitted signal to a receiver. ToA is the time of transmission plus a propagation-induced time delay dependent upon the medium through which the signal is traveling [15]. To determine ToA, the transmitter and receiver require synchronized clocks, and the propagation speed in the medium has to be known. The distance to the source is then calculated by

$$d = (T_2 - T_1)v_p, \quad (2.1)$$

where T_2 is the ToA, T_1 is the transmission time, and v_p is the propagation speed.

Time Difference of Arrival. The second measurement type is TDoA. Unlike ToA, TDoA is a relative time measurement which requires at least two receivers. The benefit of TDoA is that only the receivers need to be synchronized, not the transmitter, because the time of transmission is not needed nor is the propagation speed. TDoA is calculated using sensor pairs to determine the constant difference, k , in ToA between each sensor in the pair

as

$$TDoA_{B-A} = (T_B - T_A) = k. \quad (2.2)$$

The difference in ToA can be expressed in units of distance by multiplying k by the speed of light, $c = 3.0 \times 10^8 \frac{m}{s}$.

Angle of Arrival. The third type of measurement is AoA, or the angle between a signal's direction of propagation and some reference direction [16]. AoA information can be used in addition to ToA and RSS data. Two methods exist to collect AoA data, each of which has specific hardware requirements. This approach can induce additional costs and require larger sensor setups. The most common of the two uses an array of two or more media specific sensors with a built in signal processing capability. Each sensor has a known position in relationship to the sensor array. The AoA is then estimated from the difference in arrival times to each sensor using signal processing techniques similar to those used with ToA information. The sensors, or antennas for RF signals, in each array must be synchronized to the other sensors within that array. The second method involves rotating two or more directional antennas pointed in different directions and determining the ratio of the RSS data collected from the two antennas [15].

Received Signal Strength. The final measurement type is RSS. Commonly reported as the measured signal power, it is the receiver's received signal strength reported by the RSSI circuit [15]. No additional hardware is required for RSS based localization systems, because most sensors already have RSSI circuitry built-in as opposed to the hardware and software requirements needed for many of the previously discussed measurement modalities. Additionally, RSS systems are simple to implement because they do not require specific messages or data packets be transmitted. The received power P_l over a wireless channel is typically modeled as log-normal, with a Gaussian distribution in the decibels (dB) scale having an ensemble mean of $\bar{P}(d_l)$ (dB) which is found using the *Path*

Loss Model [15, 18–20]:

$$P_l \sim \mathcal{N}(\bar{P}(d_l), \sigma^2). \quad (2.3)$$

In Equation (2.3), $\bar{P}(d_l)$ is calculated using the *Path Loss Model* which attempts to describe the environment without any site-specific information:

$$\bar{P}(d_l) = P_T - \Pi_0 - \eta_p 10 \log_{10} \left(\frac{d_l}{d_0} \right), \quad (2.4)$$

The *Path Loss Model* incorporates free space path loss and extends to practical multipath environments which typically include many obstructions such as walls and furniture [20]. In Equation (2.4), P_T is the transmitted power in dBm, η_p is the estimated path loss parameter in free space, Π_0 is the loss measured at a short reference distance d_0 , and d_l is the Euclidean distance (i.e., *l2-norm*) between the receiver i and transmitter j for link l :

$$\begin{aligned} d_l &= \sqrt{(x_i - x_j)^2 + (y_i - y_j)^2}, \\ &= \|(x, y)_i - (x, y)_j\|. \end{aligned} \quad (2.5)$$

The number of sensors required in a WSN for RSS localization is dependent upon the size of the area to be monitored. The sensor network used in this research employs a token ring protocol, where each receiver reports respective RSS values to a base station in a sequential manner. The base station then reports the data to a processing unit which employs estimation techniques such as a Maximum Likelihood Estimate (MLE) to estimate emitter position.

2.2.2 *Localization Methods.*

As previously mentioned, the four main localization methods are trilateration, multilateration, triangulation, and RSSI. These techniques are applicable for both radio-location, where one or more receivers are attempting to locate a transmitter, and radio-navigation, where a single receiver is utilizing one or more transmitters to determine its own position. For simplicity, these techniques will be explained in terms of radio-location.

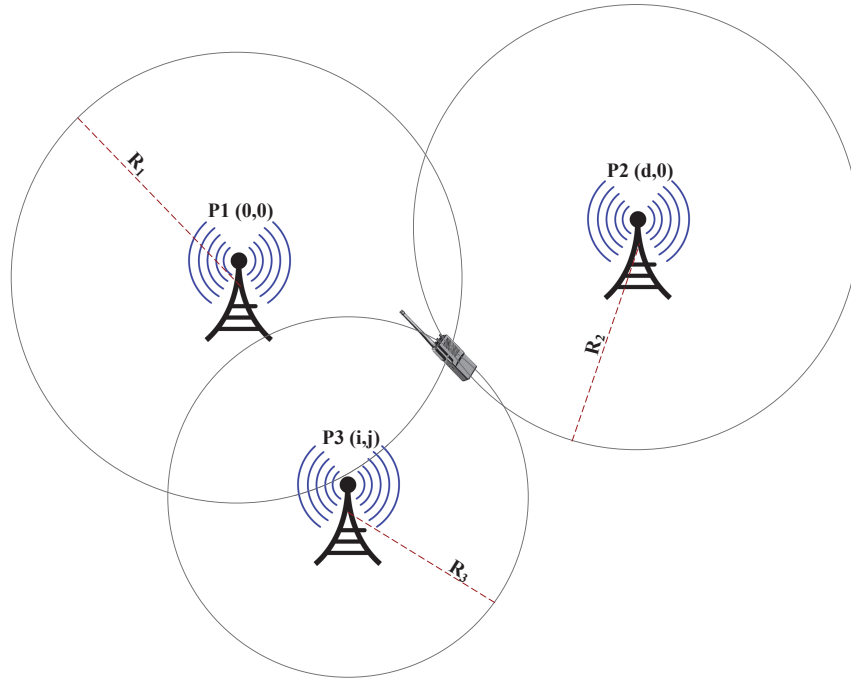


Figure 2.1: ToA Trilateration.

Trilateration. Trilateration is the process of using ToA data to determine the absolute distance to the source, and then applying the geometry of circles, triangles, or spheres to estimate emitter position. For example, when only one receiver is available one can determine the relative distance of an emitter. This distance is used to draw the radius of a circle whose perimeter represents the number of possible emitter positions. If the number of receivers is increased to two, then two circles are generated; narrowing the possibilities down to two, located at the intersections of the two circles. Furthermore, if three receivers are available, an emitter's position can be narrowed to one choice. Each of these scenarios can determine only a 2-D position estimate. A 3-D position estimate can be achieved if four or more receivers are available. An illustration trilateration using ToA measurements can be seen in Figure 2.1.

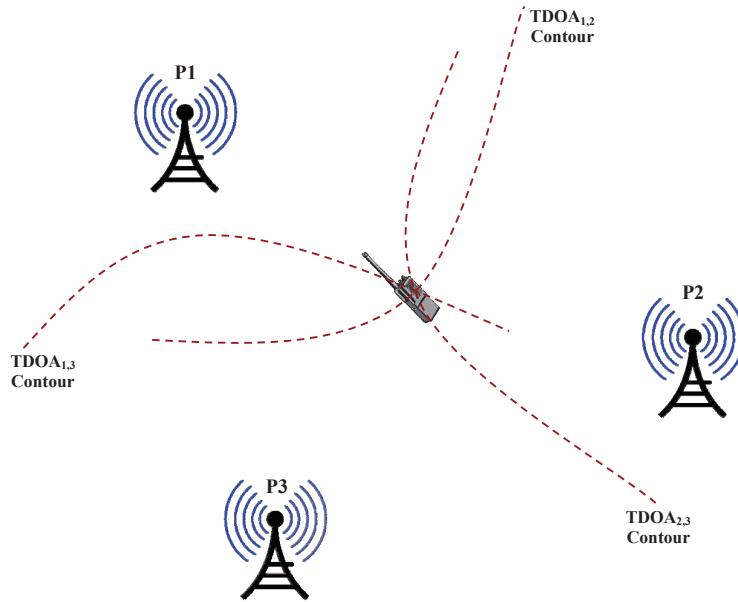


Figure 2.2: TDoA Multilateration.

Multilateration. In multilateration, TDoA data are used to determine the relative distances from the transmitter to a respective receiver pair. This relationship can be graphically represented as a hyperbola. In multilateration, at least one sensor pair, or two receivers, is required; however, with four receivers, the possible emitter positions can be narrowed to one position. And similarly compared to trilateration, with five receivers a 3-D position estimate can be achieved. An illustration of multilateration using TDoA measurements can be seen in Figure 2.2.

Triangulation. The last method, triangulation, uses AoA information to estimate emitter position. This method requires at least two sensor arrays. Each array estimates the direction the signal is coming from and determines the angle to that direction relative to a predetermined reference line. The distance between each sensor array is also already

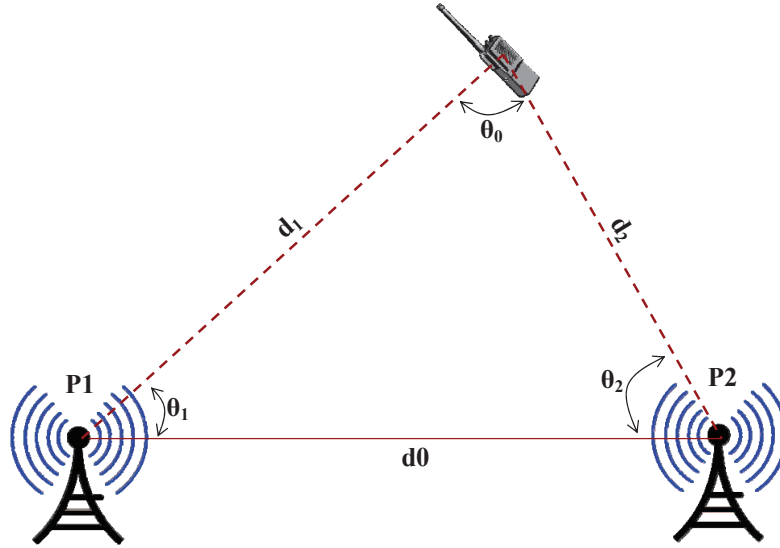


Figure 2.3: AoA Triangulation.

known. This information is graphically represented as a triangle with the values of two known angles and one side, making it possible to use geometry to determine the distance to the emitter. Increasing the number of sensor arrays used provides further precision. An illustration of triangulation using AoA measurements can be seen in Figure 2.3.

Received Signal Strength Indicator. In many cases RSSI data can be incorporated and used to bolster the three previously discussed methods [21]. However, RSSI based localization can stand on its own and be approached in three different ways. The first requires the target object to carry a transmitter, periodically transmitting while deployed nodes listen and record RSS [14, 21]. In the second method, the roles of the target object and sensor nodes are reversed, similar to radio-navigation methods [14]. The last method consists of deployed sensor nodes, as well as the target object, having a transceiver

[14]. With this method, the target object essentially becomes a part of the sensor network, participating within the network traffic by passing RSS measurements with the rest of the nodes.

2.2.3 Limiting Factors.

Both ToA and TDoA measurements suffer from additive noise and multipath effects. In order to combat additive noise, correlation techniques can be used; however, knowledge of the signal and noise power spectra is required [15]. Additional range errors can also be introduced by multipath when the absolute arrival time of the signal must be discernible. When using a correlation-based process, multipath can cause the true LOS signal to be lost because it has either been greatly attenuated resulting in decreased Signal to Noise Ratio (SNR) or unintended multipath signals have arrived shortly after, blurring the true signal peak. Even minor arrival time errors can result in very large distance errors. Another limiting factor of ToA is the need for each receiver and transmitter to have synchronized clocks. TDoA also is slightly limited by the need for at least the receivers to be synchronized.

AoA also suffers from additive noise and multipath to some extent but is also limited by the requirement for additional antennas, sensors, and processing power; inducing additional cost and maintenance requirements.

Signal power decays as the distance between the emitter and receiver increases. This alone does not limit RSS localization networks, but can compound the two common sources of error in WSNs [15]. The first is multipath, which can be difficult to mitigate, especially as the number of sensors employed grows to cover a vast area. Multipath results in frequency-selective fading, a phenomenon that exists when multiple signals with different amplitudes and phases arrive at a receiver at the same time. In scenarios where these networks are envisioned to be employed, it would not be feasible or cost effective to surround the area with absorbent materials. Frequency-selective fading can be diminished by averaging the

received power over a wide range of frequencies [15]. The second is signal attenuation due to shadowing caused by physical obstructions naturally present in the environment. These effects are random and dependent on the topography where the network is employed. However, they can be modeled in an attempt to minimize the impact. Research in [22] has shown that by modeling the radio propagation specifically for the intended environment, a 15% improvement in localization precision is possible.

2.3 Self-Localization

Another important area to consider is the ability for a WSN to accurately self-localize. In other words, a network's inherent ability to determine the location of participating nodes, based on only a few nodes' *a priori* known location information (called anchor nodes). Without precise node positioning, the accuracy of the data later collected from the network can be significantly affected [23]. This is often also referred to as either node localization or cooperative localization. In cooperative localization, sensors work together to make measurements and form a map of the network using estimation techniques [15, 24]. In sensor networks where an algorithmic localization approach isn't used, it can either be done manually—opening the door for human error, or with specialized hardware (GPS, ultra-sound, acoustic, laser) which can be costly [23]. Self-localization is also appealing to communities who are more likely to employ ad-hoc networks, such as in emergency and military situations when timeliness and multitasking is of the essence.

The measurement-based methods described in Section 2.2.2 are also applied in self-localization among other iterative estimation schemes. The same limiting factors similarly affect the process of self-localization as well. There are two main classes of localization schemes: centralized—measurements and processing is done by a single computer, and decentralized—splitting the work with the deployed nodes. The benefits of RFIC sensor networks include low maintenance requirements, small footprints, and low costs; however, nodes have limited processing and memory capabilities. Therefore, localization schemes

must take sensor limitations into account. Another benefit of employing self-localization schemes is the ability to develop location-based routing protocols, saving significant energy and improving caching behavior [25].

To combat the unreliable nature of RSS based methods, [23] presents a probabilistic, decentralized localization scheme which assumes the targeted network topology, in most employments, will form a grid. By exploiting knowledge of the intended topology, they are able to implement a probability grid matrix in which each node searches to find the position that has the highest probability. Stoleru and Stankovic were inspired by a similar solution called DV-Hop [26], which relies on hop-counts between sensors and does not employ *a priori* information about network topology.

Hu and Evans present a Sequential Monte Carlo (SMC) localization method and argue that it has the ability to take advantage of mobile networks to improve accuracy and precision without relying on evenly distributed seed nodes or prior knowledge of the network topology [25]. Their method was adapted from the Monte Carlo Localization (MCL) method originally developed for the use of robotics, and has been previously found successful in the areas of target tracking using RTI [27].

Lastly, a distinct category of localization algorithms includes those based on connectivity rather than range measurements like those in Section 2.2.1 [28]. Such algorithms rely on the knowledge of which nodes are within transmit distance and how many successful transmissions there are over a specific period of time.

2.4 Passive, Device-Free Localization

As an emerging and highly desirable capability, RF-based DFL using WSNs supports potential applications in intrusion detection, rescue-assistance, and inventory monitoring [6]. In scenarios such as these, it is unreasonable to expect persons of interest to actively participate in the system by carrying some type of radio device [7–9, 29]. Up until the past decade, common radar imaging systems used for tracking moving objects indoors included

video, pressure, infrared, and ultrasound [14]. The majority of these systems transmit some form of electro-magnetic (EM) wave and utilize signal echoes off of an object to determine range, altitude, direction, and speed. Such technologies typically require large scale hardware structures and complicated software operating systems, which are costly and challenging to maintain and are often limited by the environments in which they may be applied [14]. In many situations, the logistics challenges of using common radar systems prevent them from being a viable candidate for situational awareness and monitoring.

It is in these cases where WSNs consisting of RFICs stand out. They are relatively inexpensive, do not take up much physical space, and communicate wirelessly. Additionally, advances in peer-to-peer data networking have made it feasible to employ large-scale RF sensor networks on the order of hundreds to thousands of simple radio devices [12, 30, 31]. Such WSNs are employed by surrounding a physical area with RFICs, commonly referred to as nodes or motes. Each node pair communicates wirelessly, transmitting radio signals via a link, l , as illustrated in Figure 2.4. Most RFICs have the inherent ability to collect RSS measurements from the network. There are various methods in which this information can be exploited and are discussed in detail below. To paint an accurate picture of the field of DFL, related work in the areas of Ultra-Wideband (UWB) radar and RSS Fingerprinting is covered in Sections 2.4.1 and 2.4.2 respectively.

2.4.1 Ultra-Wideband Radar.

Another form of DFL is UWB radar which uses WSN structures similar to those in RTI applications, except the network consists of UWB radio sensors and employs radar-based ranging and imaging techniques [32–35]. Through-wall penetration and high resolution detection and localization are possible over short distances with the lower frequencies used in the UWB spectrum [32]. These networks illuminate the environment by transmitting UWB signals and collect information about the environment by recording backscattered waves in which the signals are delayed, phase shifted, or attenuated. Using larger RF

bandwidths, UWB networks overcome many of the multipath fading losses that occur in narrow-band networks like those used in RTI because they do not rely on RSS [33].

A variety of sensor types are used in specific capacities in UWB networks. Sensors consisting of a single transmitter act as illuminators of the environment, sensors consisting of a single receiver act as observers acquiring information about the structure of the environment, and Single Input, Single Output (SISO) sensors act as anchor nodes placed at verified positions to aid in self-localization. Then there are Single Input, Multiple Output (SIMO), Multiple Input, Single Output (MISO), or MIMO nodes referred to as “scouts” [32] which have the inherent ability to estimate directions of arrival. Sensor deployments use various combinations of the previously described sensors depending on the radar approach (i.e., bistatic or multistatic) [32, 35].

2.4.2 Received Signal Strength Fingerprinting.

Another form of RSS based localization uses a method known as fingerprinting. These systems have been demonstrated in self-localization [36], active localization (targets carry Radio Frequency Identification (RFID) or electronic devices) [22, 37–39], and in DFL [30, 40]. This section briefly discusses RSS fingerprinting for DFL.

Fingerprint-based methods use a database of training measurements collected while the system is offline and then compares real-time RSS measurements with the database to estimate a target’s location [13, 30, 41]. In simple terms, training measurements are collected by creating a passive radio map of the resulting attenuation field when a target stands in each possible position. Measurements are taken as an entity walks through the network, moving through a predefined grid. This area of research also seeks to employ effective signal propagation models and further explore more efficient and effective database search and estimation algorithms [13].

A strength in fingerprint-based localization as opposed to RTI is the ability to take advantage of the dynamic nature of RF signal propagation, and the resulting multipath

in an indoor environment; such effects result in very distinctive attenuation fields which make it easier to detect location while using a training database [30]. Offline training can be extensive depending on the network structure, and therefore is not an option for mobile networks. Training requirements and calibration efforts change and increase when the number of targets increases or when the network or physical area is altered such as a door being opened while training data is collected then closed when the system is online [29].

2.4.3 Received Signal Strength Tomography.

Tomography techniques were discovered and harnessed by the medical community for use in medical imaging. The work resulted in the development of such well known systems as the Computed Tomography (CT), Computed Axial Tomography (CAT Scan), Magnetic Resonance Imaging (MRI), Positron Emission Tomography (PET), and Ultrasound. These systems utilize various signal mediums. Modern tomography consists of gathering projection data in a series of 2-D cross-sectional cuts from multiple angles and using it to reconstruct a 3-D image. The results of which are integrated using tomographic reconstruction software to form the final image by applying the Radon Transform derived from the Projection Slice Theorem [42].

Ultimately, the use of tomographic methods and RSS data lead to the world of RTI. RTI is a method in which imagery is created by mapping the change in attenuation in a WSN as a function of space for the purpose of indicating the position and movement of an object [12]. Essentially, the wireless communication over M links in the network creates many projections that can be used to reconstruct an image of the objects that lie within the sensed area [12]. Images provide a medium for humans and computers to interpret the information and react. RTI is achievable using little power and with relatively small bandwidths, making it appealing in a world where limited bandwidth is available.

As opposed to RSS fingerprint-based DFL, there also exists model-based RSS DFL, where the algorithm used applies a forward model in which the statistical distribution of signal propagation is considered in determining RSS behavior when a target is present. One advantage of model-based RSS DFL systems is that they are not dependent upon a training measurement database which can require additional resources, setup, and maintenance [29]. Propagation model-based RTI can be further categorized into linear and non-linear models.

In a 2-D sensor network, the area is surrounded by K deployed wireless motes and divided into N pixels that are $\Delta_p \times \Delta_p$ ft² in size (3-D networks are divided into voxels of size: $\Delta_p \times \Delta_p \times \Delta_p$ ft³). The location of each node is either known or estimated and the location of each pixel/voxel is known. Each mote transmits a radio signal which passes through the physical area, experiencing absorption, reflection, diffraction, or scattering from objects within and around the area [12]. A basestation collects RSS data from the WSN. The wireless communication path between two nodes is called a link. Figure 2.4 illustrates the links created in a WSN. There are $M = \frac{K^2-K}{2}$ unique two-way links within the entire network such that a link between a node pair is counted only once.

Mathematically, the RSS of any one link, l at time t can be described as [12]:

$$r_l(t) = P_T - L_l(t) - S_l(t) - F_l(t) - v_l(t), \quad (2.6)$$

where

- P_T : Transmitted power (dB).
- $L_l(t)$: Static losses due to distance, antenna patterns, device inconsistencies, etc (dB).
- $S_l(t)$: Shadowing loss due to objects attenuating the signal (dB).
- $F_l(t)$: Fading loss caused by constructive and destructive interference of narrow-band signals in multipath environments (Non-Shadowing Loss) (dB).
- $v_l(t)$: Measurement Noise (dB).

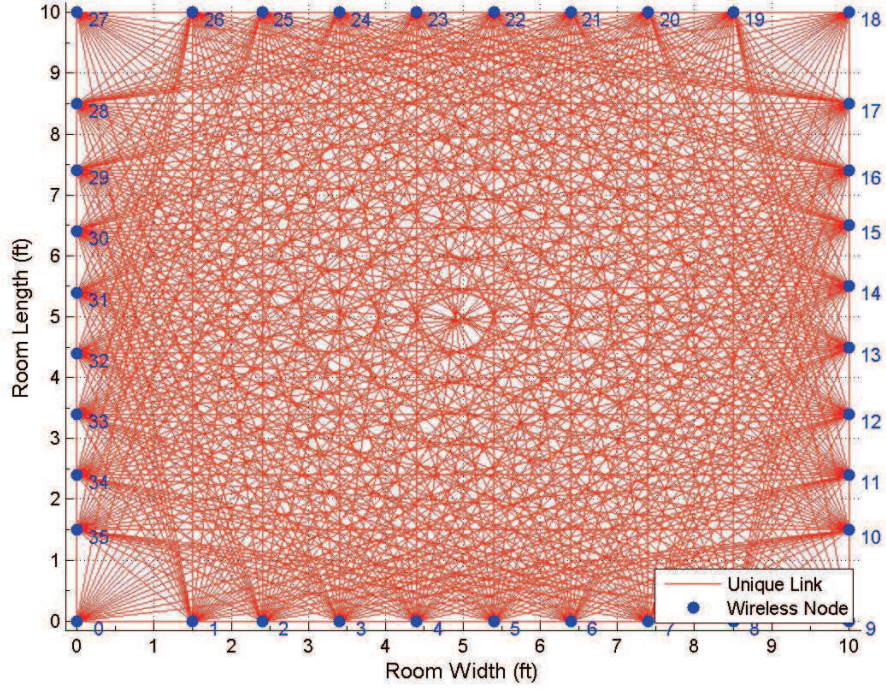


Figure 2.4: Illustration of the links created in a RTI network. $K=36$ nodes.

Typically, for model-based systems, calibration data are required but may be unnecessary depending on the measurement modality, discussed in Section 2.4.3.2. When the network is initially established, any obstructions existing in the area that are considered “common-place” become a part of the baseline. Calibration data, \mathbf{y}_c , are collected by measuring RSS for each link of the target-free network for a specified number of passes, m . Each pass refers to the time it takes for each mote to transmit once; yielding one frame of link measurements, $\mathbf{y} = [r_1, r_2, \dots, r_M]^T$. The duration of one frame t_f is dependent on the number of motes and the pass rate is defined in the token protocol. The calibration data

is an average over m frames for each link l :

$$\bar{r}_{c,l} = \frac{1}{m} \sum_{i=0}^{m-1} r_l(t_c - i), \quad (2.7)$$

$$\mathbf{y}_c = [\bar{r}_{c,1}, \bar{r}_{c,2}, \dots, \bar{r}_{c,M}]^T.$$

The resulting calibration measurements provide insight into the static environment void of any targets, and can be seen as the average signal strength for each link. During calibration, static losses are averaged out and no shadowing losses are experienced [12]. The calibration data are then used to determine the difference in RSS for each link between an “empty” network and real-time measurements taken when a target is present (i.e., the shadowing losses $S_l(t)$ incurred for each link passing through any new obstructions).

2.4.3.1 Linear Signal Propagation Model.

The most common RTI system model used to describe changes in the propagation field is linear, and is based on the effects of correlated shadowing modeled in [20, 43]. This method can be referred to as shadowing-based RTI, where only the changing attenuation from the current time and the time of calibration is of concern [18]. However, the work in [18] models the changes in RSS due to the movement of an obstruction using the skew-Laplace distribution (explained in Section 2.4.3.2), and applies a non-linear model with an iterative particle filter algorithm to estimate the location of an obstruction. The difference in RSS for one link l is calculated by subtracting the link RSS obtained during calibration from a current link RSS measurement, $\Delta r_l = r_l(t_r) - r_l(t_c)$ where t_r is the frame currently being evaluated. A link measurement can be further decomposed to illustrate each component contributing to the RSS:

$$\Delta r_l = S_l(t_r) - S_l(t_c) + F_l(t_r) - F_l(t_c) + v_l(t_r) - v_l(t_c). \quad (2.8)$$

All static losses can be removed over time and the remaining loss terms are grouped together in a single noise term:

$$n_l = F_l(t_r) - F_l(t_c) + v_l(t_r) - v_l(t_c), \quad (2.9)$$

resulting in the final definition of the change in RSS:

$$\Delta r_l = S_l(t_r) - S_l(t_c) - n_l. \quad (2.10)$$

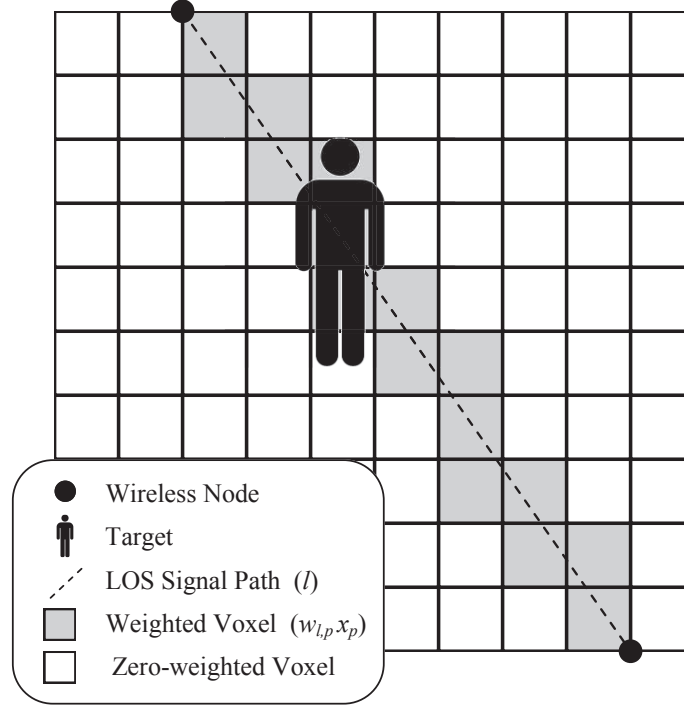


Figure 2.5: Illustration of a single obstructed link in an RTI network.

The shadowing loss experienced in an obstructed link can be approximated as a weighted sum of the signal attenuation x experienced in each pixel p at time t ,

$$S_l(t) = \sum_{p=1}^N w_{l,p} x_p(t). \quad (2.11)$$

A precalculated weight $w_{l,p}$ is applied to each pixel based upon the chosen weighting model. The weighting model is used to determine the amount of link attenuation that is distributed in each pixel the link crosses. An illustration of an obstructed link and the affected pixels is shown in Figure 2.5. There are many different options for weight models which are

discussed in greater detail in Section 2.4.3.3. Thus, the change in RSS of each link can be described as a linear sum of the change occurring in each pixel:

$$\Delta r_l = \sum_{p=1}^N w_{l,p} \Delta x_p + n_l, \quad (2.12)$$

where Δx_p is the change in attenuation from the calibration period t_c for pixel p caused by the presence of a target,

$$\Delta x_p = x_p(t_r) - x_p(t_c). \quad (2.13)$$

The entire network of RSS links can be described in matrix form [12]:

$$\mathbf{y} = \mathbf{W}\mathbf{x} + \mathbf{n}. \quad (2.14)$$

where each variable is defined as:

$$\begin{aligned} \mathbf{y} &= [\Delta r_1, \Delta r_2, \dots, \Delta r_M]^T \text{ (dB)}, \\ \mathbf{x} &= [\Delta x_1, \Delta x_2, \dots, \Delta x_N]^T, \\ \mathbf{n} &= [n_1, n_2, \dots, n_M]^T \text{ (dB)}, \\ [W]_{l,p} &= w_{l,p}. \end{aligned} \quad (2.15)$$

The units of \mathbf{W} and \mathbf{x} are dependent upon the weighting model used as discussed in Section 2.4.3.3. The change in attenuation in any particular pixel represents the presence of a target; therefore, the ultimate goal is to reconstruct a radio tomographic image by estimating \mathbf{x} . Various estimation techniques are discussed in Section 2.4.3.4. The reconstructed image can then be used to determine target location and possibly other details such as size and orientation [7, 12].

2.4.3.2 Measurement Modalities.

Multiple measurement modalities exist as a means to utilize RSS. Standard RTI relies on a single measurement of the change in RSS as previously defined in Equation (2.12). The following methods take advantage of various statistical definitions to manipulate the raw RSS measurements prior to image reconstruction as a means to eliminate noise.

Mean-based Received Signal Strength. The simplest approach is to use the sample mean of differenced RSS measurements in the presence of a target. For m frames, link RSS is described as:

$$\bar{r}_{l,t} = \frac{1}{m} \sum_{i=0}^{m-1} r_l(t_b - i), \quad (2.16)$$

$$\Delta \bar{r}_{l,t} = \bar{r}_{l,t} - r_{c,l}, \quad (2.17)$$

$$\mathbf{y}_{mean} = [\Delta \bar{r}_{1,t}, \Delta \bar{r}_{2,t}, \dots, \Delta \bar{r}_{M,t}]^T. \quad (2.18)$$

The vector of RSS measurements \mathbf{y} in Equations (2.14) and (2.15) is replaced with the vector of sample means for each link $\mathbf{y}_{mean} = \mathbf{W}\mathbf{x} + \mathbf{n}$ prior to solving the inverse problem to estimate x . Doing so reduces the effects of noise and loss due to motion [43]. The sample mean is useful in locating both static and moving targets. It is more effective in smaller networks when the time it takes to record one frame of RSS measurements is minimal and when targets within the network move at a comparable pace.

Variance-based Received Signal Strength. Another modality of RTI is termed Variance-based Radio Tomographic Imaging (VRTI), which takes advantage of the motion-induced variance of RSS caused by the movement of an object within a sensor network [29, 44, 45]. In a WSN it is common to experience high amounts of multipath, because a wireless signal travels along many different paths before reaching the receiver, causing constructive and destructive interference. When motion occurs near a wireless link, a number of those multipath components are affected and the RSS variance will fluctuate. The effect will be greater where there is a higher density of links, specifically closer to a node.

The RSS at a node is dependent upon the power contained in its multipath components; [45] quantifies this relationship of the fading environment with a Ricean distribution. Two types of multipath are considered in this problem; that of changing or non-static multipath which consists of the multipath components affected by the motion of some

object, and those static multipath components that are unaffected by the same object's motion. Ultimately, the variance in RSS due to motion in the network can be used to locate and track an object.

Applying the linear model described in Equation (2.14) the measurement used is the sample variance defined over window $m = t_b - t_a$ as [29, 44]:

$$\begin{aligned} Var[r_{l,t}] &= \frac{1}{m-1} \sum_{i=0}^{m-1} (\bar{r}_{l,t} - r_l(t-i))^2, \\ r_l(t) &= \sum_{p=0}^N w_{l,p} (x_p(t_b) - x_p(t_a)) + n_l, \\ \mathbf{y}_{var} &= [Var[r_{1,t}], Var[r_{2,t}], \dots, Var[r_{M,t}]]^T. \end{aligned} \quad (2.19)$$

where $m-1$ is used because the population mean is unknown and $\bar{r}_{l,t}$ is still defined as in Equation (2.16). Finally, the vector of RSS measurements \mathbf{y} in Equations (2.14) and (2.15) is replaced with the vector of sample variances for each link $\mathbf{y}_{var} = \mathbf{W}\mathbf{x} + \mathbf{n}$ prior to solving the inverse problem to estimate x . Note in the second part of Equation (2.19), the change in RSS is determined for each time step rather than between the current time and the calibration period. In VRTI there is no need to collect calibration data because only the variance in RSS is of concern, not necessarily the change in RSS, Δr_l . But, it is also for this reason that VRTI has proven to be less accurate at locating a static object as compared to shadowing and mean-based RTI [44, 45].

The sample definitions of the mean and variance are used in mean-based and variance-based RSS because they represent unbiased estimates of the actual mean and variance which are unknown.

Channel Diversity. Research in [5] shows the localization accuracy of RTI can be dramatically improved by exploiting multichannel communication among the nodes. Two selection methods are used in collecting RSS measurements from multiple channels for each link. The measured RSS for link l shown in Equation (2.6) is modified as:

$$r_{l,k} = P_{T,k} - L_{l,k} - S_{l,k}(t) + F_{l,k}(t) - v_{l,k}(t), \quad (2.20)$$

where k represents the frequency channel [5]. The *Channel Diversity* model still requires a calibration period as described by Equation (2.7); however, a calibration measurement is taken for each channel (i.e., $\bar{y}_{c,k}$). The sum of the change in fade loss on channel k and the change in measurement noise from the calibration period is $\Delta n_{l,k}$; therefore the linear model in Equation (2.12) is now written as:

$$\Delta r_{l,k} = \sum_{p=1}^N w_{l,p} \Delta x_{p,k} + \Delta n_{l,k}. \quad (2.21)$$

Channel selection is based on one of two models, the *Packet Reception Rate (PRR)* method and the *Fade Level Method* [5]. The *PRR* method selects the m channels for each link $l \in \{1, 2, \dots, M\}$ that have the highest PRRs and forms the set Set_l containing the respective channel indices. The *Fade Level* method sorts all the channels for link l by fade level $F_{l,c}$ and selects the top m channels forming the set Set_l .

The total change in RSS for link l is the sample average of the measured changes in RSS for each channel k of the link which is written as:

$$y_l = \frac{1}{m} \sum_{k \in Set_l}^m \Delta r_{l,k}, \quad (2.22)$$

and the collection of link measurements is the vector,

$$\mathbf{y}_{chan} = [y_{1,Set_1}, y_{2,Set_2}, \dots, y_{M,Set_M}]^T. \quad (2.23)$$

The *PRR* method selects channels maximizing the communication reliability of the links and the *Fade Level* method selects channels maximizing the fade level of the link opting for channels that are either in antifade or removing channels experiencing deeper fade levels [5].

Fade Level-Based Measurement Model. Wilson and Patwari in [18], discovered that each link in a network experienced unique shadowing effects based on its multipath components. Through extensive measurements, they found the fade level of a link to be a measurable quantity of the fading experienced on the static link when the network was

empty, essentially leading to the discovery that each link demonstrated drastically different behavior when obstructed as a function of the fade level [18].

When a LOS link is directly obstructed, it is safe to assume the link will be attenuated, experiencing a reduction in RSS. However, in congested environments, most links are NLOS and there is a significant presence of multipath. Thus, the presence of an obstruction near a link affects only a subset of multipath components and therefore an obstruction on a LOS link will have less predictable effects [18]. Using calibration data as defined by Equation (2.7), the fade level experienced in link l can be quantified as the difference between the path loss prediction described by Equation (2.4) for that link and the calibration mean:

$$F_l = \bar{y}_{c,l} - \bar{P}(d_l). \quad (2.24)$$

Links with negative fade levels are said to be in *Deep Fade*, meaning that they experience destructive multipath interference, and those with positive fade levels are in *Antifade* which means they experience constructive multipath interference. As a result, links in deep fade tend to experience a high variance of RSS when an obstruction is in the network while links in antifade are less predictable, where the RSS will vary less if at all, and may even increase [18]. Even so, Wilson et al. found links in antifade to be more informative. The introduction of fade loss in an RTI measurement model is expanded on in [17] by implementing the *Channel Diversity Measurement Model* described previously, in addition to considering the effects of fade losses as a result of multipath. The fade level can be determined for each link and each channel as represented by $F_{l,k}$.

The *Fade Level-based Measurement Model* uses the estimated probability of an obstruction being within a modeled ellipse (more details are provided in Section 2.4.3.3), and relies on both the magnitude and the sign of the measured change in RSS [17]. Kaltiokallio et al. reported that with larger changes in RSS the probability increases for both deep fade and antifade links; however, with deep fade links the modeled ellipse is

larger. They also found that the probability of an obstruction being located within the modeled ellipse for an antifade link was significantly higher than that of a deep fade link for positive changes in measured RSS. Using an exponential model, the probability of an obstruction being located within the modeled ellipse at time t with the measured change in RSS $\Delta r_{l,k}$ for link l on channel k can be described by:

$$p_{l,k}^{\delta}(t) = 1 - \exp\left(\beta_{l,k}^{\delta} |\Delta r_{l,k}(t)|\right), \quad (2.25)$$

where δ indicates the sign of the change in RSS, such that δ is - for measured decreases in RSS and δ is + for measured increases. And lastly, $\beta_{l,k}^{\delta}$ is the decay rate related to the fade level,

$$\beta_{l,k}^{\delta} = b^{\delta} \exp\left(\frac{F_{l,k}}{k^{\delta}}\right), \quad (2.26)$$

where the model parameters b^{δ} and k^{δ} are derived using a least-squares fit to the experimental data collected in [18]. The set of measurement vectors on channel k for all links are defined by:

$$\begin{aligned} \mathbf{y}_k^{-} &= [p_{1,k}^{-}, p_{2,k}^{-}, \dots, p_{L,k}^{-}], \\ \mathbf{y}_k^{+} &= [p_{1,k}^{+}, p_{2,k}^{+}, \dots, p_{L,k}^{+}], \end{aligned} \quad (2.27)$$

where channels experiencing attenuation are \mathbf{y}_k^{-} and the channels experiencing an increase in RSS are \mathbf{y}_k^{+} . Thus the measurement vector for channel k is $\mathbf{y}_k = [\mathbf{y}_k^{+} | \mathbf{y}_k^{-}]$, and the overall measurement vector including measurements for every channel is:

$$\mathbf{y}_{fade} = [\mathbf{y}_1 | \dots | \mathbf{y}_C]^T, \quad (2.28)$$

where C is the total number of frequency channels used.

2.4.3.3 Weighting Models.

In an RTI network each pixel is assumed to have a constant attenuation loss over its entire area (voxel→volume). The weighting model \mathbf{W} can be decomposed into two distinct pieces, the selection of affected pixels, sometimes referred to as the spatial impact area,

using a binary selection matrix \mathbf{S} , and the scalar magnitude of the weight assigned to the pixel $\mathbf{\Omega}$ [46]:

$$\mathbf{W} = \mathbf{\Omega} \odot \mathbf{S}, \quad (2.29)$$

where \odot indicates Hadamard (element-wise) multiplication. There have been several models explored in the literature. The following paragraphs contain descriptions of several of them.

NeSh Normalized Ellipse Model. As shown in Equation (2.6), the received power for any link suffers from path loss caused by three phenomena other than measurement noise v_l . As previously explained, static losses L_l can generally be removed over time. Therefore, the received power for a particular link will vary from the ensemble mean $\bar{P}(d_l)$ described by Equation (2.4) mostly due to F_l and shadowing S_l losses [20, 43]. The total fading loss Z_l is represented mathematically by [20, 43, 47]

$$P_l = \bar{P}(d_l) - Z_l, \quad (2.30)$$

$$Z_l = F_l + S_l. \quad (2.31)$$

The large-scale path loss described above includes average fading loss at the distance d (shown in Equation (2.4)) by allowing values for free space path loss, $\eta_p = 2$ [47]. This model considers links within geographical proximity of each other to experience significant non-zero correlation or covariance. Shadowing losses experienced in each link l are determined to be a function of the resulting shadowing field $p(x)$. The shadowing of link l is modeled as an integral over the spatial field between the endpoints x_i and x_j :

$$S_l \triangleq \frac{1}{d_{i,j}^{\frac{1}{2}}} \int_{x_i}^{x_j} p(x) dx, \quad (2.32)$$

such that the endpoints in terms of RTI would represent the transmitting and receiving nodes and the normalization factor relates to the distance between the two nodes [47]. On its own, this model termed as the *Network Shadowing (NeSh) Model* was introduced in [47] and [20] as a means to describe the relationship between shadowing and fading losses

on links in a multi-hop network. However, it has more recently been expanded [43] and utilized in [5, 12, 29, 44, 45, 48]. The model is adapted, using the normalization factor as a weight $\mathbf{\Omega}^{NeSh} = \frac{1}{\sqrt{d_l}}$ to take into account that the variance of link shadowing does not change with distance, and adding a selection matrix to adapt it for RTI networks:

$$w_{l,p}^{NeSh} = \frac{1}{\sqrt{d_l}} \begin{cases} 1 & \text{if } d_1(l, p) + d_2(l, p) < d_l + \lambda \\ 0 & \text{otherwise} \end{cases}, \quad (2.33)$$

where $w_{l,p}$ is the weight assigned to pixel p for link l , d_l is the distance between nodes d_1 and d_2 , and λ is a tunable parameter to set the width of the weighting ellipse defined by the selection matrix shown in Equation (2.33). This model assumes each pixel falling within the ellipse defined by $d_l + \lambda$ has equal weight. Relating to Equation (2.29) the *NeSh Normalized Ellipse Model* is decomposed by $\mathbf{W}^{NeSh} = \mathbf{\Omega}^{NeSh} \odot \mathbf{S}^{Ellipse}$.

Line Model. The *Line Model* is decomposed as $\mathbf{W}^{Line} = \mathbf{\Omega}^{Line} \odot \mathbf{S}^{Line}$ represented by:

$$w_{l,p}^{Line} = L_{l,p} \begin{cases} 1 & \text{if link } l \text{ traverses voxel } p \\ 0 & \text{otherwise} \end{cases}, \quad (2.34)$$

where $L_{l,p}$ is the length of the section of link l passing through pixel p . The *Line Model* \mathbf{W}^{Line} resembles the model used in CT scans in medical imaging, but was demonstrated in its entirety in the area of RTI in [49] and [50]. The *Line Selection Matrix* \mathbf{S}^{Line} has been demonstrated in [11, 51–53]. In this model, the weight assigned to the attenuation is dependent on the actual length of the link passing through the obstruction as opposed to the *NeSh Model* which is based on the length of the entire link [46, 49]. Of the models discussed in this chapter, the *Line Model* is the cheapest computationally [46].

NeSh Line Model. The *NeSh Line Model* is a hybrid of the two previously discussed models first. The weighting factor $\mathbf{\Omega}^{NeShLine}$ accounts for link length and the length of link passing through the obstruction. It was first demonstrated in [51] and [11] in combination

with the *Line Selection Matrix* \mathbf{S}^{Line} , such that $\mathbf{W}^{NeShLine} = \mathbf{\Omega}^{NeShLine} \odot \mathbf{S}^{Line}$ where:

$$w_{l,p}^{NeShLine} = \frac{L_{l,p}}{\sqrt{d_l}} \begin{cases} 1 & \text{if link } l \text{ traverses voxel } p \\ 0 & \text{otherwise} \end{cases}. \quad (2.35)$$

Exponential Decay Model. The *Exponential Decay Model* considers an elliptical model similar to that proposed in [47]; however, the width of the ellipse adapts with respect to the object's distance from link l [27]. For each link l , the width of the ellipse is defined by:

$$\lambda_{l,p}(t) \triangleq d_{1,l}(x_t) + d_{2,l}(x_t) - d_l, \quad (2.36)$$

where $d_{1,l}(x_k)$ and $d_{2,l}(x_k)$ are the distances of the obstruction at time t from the transmitting and receiving nodes for link l respectively. The ellipse is used to define the area affected by the obstruction, where the width of the ellipse is defined by the situation such that it is the smallest it can be to include the center of pixel p [46], as opposed to the width of the ellipse in the *NeSh Normalized Ellipse Model* which is set by λ as defined by the user. However, it is incorporated into the assigned weight $\mathbf{\Omega}$ rather than in the selection matrix \mathbf{S} such that:

$$w_{l,p}^{ExpDec} = \exp\left(\frac{\lambda_{l,p}}{2\sigma_\lambda}\right) \begin{cases} 1 & \lambda_{l,p} \geq 0 \\ 0 & \text{otherwise} \end{cases}, \quad (2.37)$$

where σ_λ controls the rate of decay of attenuation with respect to λ [27]. Taking a closer look at the selection matrix above, it can alternatively be written as $\mathbf{S}^{All} = 1$ for all pixels because $\lambda_{l,p}$ will always be positive; therefore $\mathbf{W}^{ExpDec} = \mathbf{\Omega}^{ExpDec} \odot \mathbf{S}^{All}$. A weight is assigned to each pixel in the network. In this model, the pixel weighting values decrease as the ellipse size increases [27, 46]. Essentially, pixels further away from the obstructed link approaching the edge of the ellipse will be assigned a lower weight than those closer to the obstructed link.

Inverse Area Elliptical Model. The *Inverse Area Elliptical Model* is similar to the *Exponential Decay Model*; however, the weighting function is proportional to the inverse

area of the smallest ellipse that includes the pixel in consideration [54, 55]. The selection matrix is bounded by setting minimum and maximum semi-minor axis lengths controlled by $\lambda_{l,p}$ so the weight for points falling outside of the largest ellipse are set to 0. The *Inverse Area Elliptical Model* is described by $\mathbf{W}^{InvArea} = \mathbf{\Omega}^{InvArea} \odot \mathbf{S}^{Ellipse}$, such that

$$w_{l,p}^{InvArea} = \left[\frac{\pi}{4} (d_l + \lambda_{l,p}) \sqrt{2d_l \lambda_{l,p} + \lambda_{l,p}^2} \right]^{-1} \begin{cases} 1 & \text{if } d_1(l, p) + d_2(l, p) < d_l + \lambda_{l,p} \\ 0 & \text{otherwise} \end{cases}, \quad (2.38)$$

where $\lambda_{l,p}$ is the same as was defined in Equation (2.36) [46, 54, 55]. The model applied in [56] is a modified form of the *Inverse Area Ellipse Model*. It uses the ellipse described in Equation (2.33) such that the model is decomposed by $\mathbf{W}^{InvArea} = \mathbf{\Omega}^{InvArea} \odot \mathbf{S}^{Ellipse}$ and:

$$w_{l,p}^{InvArea} = \frac{1}{A_l} \begin{cases} 1 & \text{if } d_1(l, p) + d_2(l, p) < d_l + \lambda \\ 0 & \text{otherwise} \end{cases}, \quad (2.39)$$

where $\mathbf{\Omega}^{InvArea} = \frac{1}{A_l}$, and A_l is the area of the ellipse defined by $d_l + \lambda$. The weights within the ellipse are constant for each pixel. The model used in [18] also uses the inverse of the area of the ellipse. It is described in more detail in the next section.

Fade Level-Based Spatial Weight Model. The previously mentioned models do not account for multipath and assume any signal attenuation to be the result of shadowing losses alone. Work in [18] suggests environments rich in multipath, and those containing long link distances, experience effects that are more complex. The *Fade Level-based Spatial Weight Model* accounts for fade loss in addition to choosing a selection matrix, or spatial model, which adapts for each link based on the specific links the target is currently obstructing [17]. Thus the spatial impact area of affected pixels may be larger or smaller, depending on the fade-level classification of the obstructed links dependent on the target's position within the network.

The results in [17] indicate that links in deep fade measured decreases in RSS within a large area such that $\lambda_l(t)$ in Equation (2.36) increased, while it decreased for links in antifade. Conversely, when an increase in RSS was measured, $\lambda_l(t)$ decreased for links

in deep fade, meaning the change in RSS induced by an obstruction was measured in a smaller area than the antifade links. However, the difference in the increase in $\lambda_l(t)$ for different fade levels was relatively small compared to the differences in the decrease in $\lambda_l(t)$ [17].

Using an exponential decay function to model decreases in ellipse width and an exponential growth function to model increases in ellipse width, $\lambda(t)$ can be determined separately for each link, frequency channel and sign of RSS change based on F_l ,

$$\lambda_{l,k}^\delta = b^\delta \exp\left(\frac{F_{l,k}}{k^\delta}\right), \quad (2.40)$$

where k represents the frequency channel [18]. The *Fade Level-based Spatial Weight Model* parameters are derived using a least-squares fit to the experimental data collected in [18]. The resulting weight model $\mathbf{W}^{Fade-Spatial}$ is described as:

$$w_{l,k,p}^\delta = \frac{1}{A_l} \begin{cases} 1 & \text{if } d_1(l, p) + d_2(l, p) < d_l + \lambda_{l,k}^\delta, \\ 0 & \text{otherwise} \end{cases}, \quad (2.41)$$

where $\Omega^{Fade-Spatial}$ is the inverse area of the ellipse such that $A_l = n_p \Delta p$; n_p is the number of pixels within the ellipse of link l and Δp is the area of the pixel [18]. In summary, the weight assigned to pixel p for link l on channel k is dependent upon the fade level of the link and the sign of the measured change in RSS. Using the inverse of the area of the ellipse assigns less weight to links that have larger spatial impact areas as discussed in Section 2.4.3.2. This model was also used in [57].

2.4.3.4 Signal Recovery & Solving the Inverse, Ill-posed Problem.

Regularized Least Squares. One of the more common estimation techniques used to recover the image \mathbf{x} is a *Least Squares* solution which is equivalent to an *MLE* if the noise is assumed to be zero-mean Gaussian [12, 29, 44, 45, 48]:

$$\hat{\mathbf{x}}_{LS} = \underset{\mathbf{x}}{\operatorname{argmin}} \|\mathbf{W}\mathbf{x} - \mathbf{y}\|_2^2. \quad (2.42)$$

Setting the gradient of the cost function $\|\mathbf{W}\mathbf{x} - \mathbf{y}\|_2^2$ to $\mathbf{0}$ and solving for \mathbf{x} yields the estimate $\hat{\mathbf{x}}$ described by

$$\hat{\mathbf{x}}_{LS} = (\mathbf{W}^T \mathbf{W})^{-1} \mathbf{W}^T \mathbf{y}. \quad (2.43)$$

However, a *Least Squares* solution is only valid if \mathbf{W} is full-rank; therefore, the solution must be regularized, leading to a *Regularized Least Squares* solution. Multiple regularization methods have been explored in the literature and are discussed below.

Regularization. Due to the inherent nature of RTI, it is an ill-posed, inverse problem [58]. Fortunately, it is also modeled linearly, making the task of regularization simpler. An inverse problem is one that is used to determine the cause of a desired or an observed effect or outcome [59]. It often does not fulfill the postulates described by Jacques Hadamard when he defined *well-posedness*. He believed mathematical models of physical phenomena should be subject to the following properties [59, 60]:

1. A solution exists.
2. The solution is unique.
3. The solution behavior changes continuously.

When a problem does not meet these properties it is considered ill-posed, meaning it may not have a unique solution or that the solution is highly sensitive to changes in the final data. Regularization can be useful as it can help to solve ill-posed problems by introducing additional information. The additional information is determined in accordance with the approximate nature of the initial data to promote stability. Regularization techniques include penalizing erratic changes in the data, smoothing or eliminating small singular values, or imposing prior distributions. In RTI, the transfer matrix, \mathbf{W} , contains small singular values which when inverted through algebraic manipulation as in Equation (2.43), cause unwanted or noisy spectral components to grow out of control [58]. Below are a few methods that have been researched in the field of RTI.

Tikhonov

One of the most common forms of regularization, and one that has been vastly utilized in the world of RTI is *Tikhonov Regularization*, which in statistics is also referred to as ridge regression. It is appealing due to the flexibility to force desired properties in the solution through a linear transformation of the measurement data [58]. In *Tikhonov Regularization* a term is introduced into the cost function prior to minimization,

$$f_{TIK}(x) = \frac{1}{2} \|\mathbf{W}\mathbf{x} - \mathbf{y}\|^2 + \alpha (\|\mathbf{D}_x\mathbf{x}\|^2 + \|\mathbf{D}_y\mathbf{x}\|^2), \quad (2.44)$$

$$\hat{\mathbf{x}}_{TIK} = \underset{x}{\operatorname{argmin}} \left(\frac{1}{2} \|\mathbf{W}\mathbf{x} - \mathbf{y}\|^2 + \alpha (\|\mathbf{D}_x\mathbf{x}\|^2 + \|\mathbf{D}_y\mathbf{x}\|^2) \right), \quad (2.45)$$

$$\hat{\mathbf{x}}_{TIK} = (\mathbf{W}^T \mathbf{W} + \alpha \mathbf{Q})^{-1} \mathbf{W}^T \mathbf{y}, \quad (2.46)$$

where \mathbf{Q} is the *Tikhonov Matrix* and α is a tunable scaling parameter controlling the amount of influence the regularization operator \mathbf{Q} has [58, 61]. There exist two popular forms of *Tikhonov regularization* in the literature, the first is defining \mathbf{Q} as the first order difference operator \mathbf{D} for each dimension, such that:

$$\mathbf{Q} \triangleq \mathbf{D}_x^T \mathbf{D}_x + \mathbf{D}_y^T \mathbf{D}_y. \quad (2.47)$$

This method is sometimes referred to as *H1 Regularization*, and was used in [12, 29, 44–46, 49] and expanded on in [58] and [61]. The modified cost function is defined by:

$$f_{TIK}(\mathbf{x}) = \frac{1}{2} \|\mathbf{W}\mathbf{x} - \mathbf{y}\|^2 + \alpha (\|\mathbf{D}_x\mathbf{x}\|^2 + \|\mathbf{D}_y\mathbf{x}\|^2), \quad (2.48)$$

and the regularized MLE is:

$$\hat{\mathbf{x}}_{TIK} = (\mathbf{W}^T \mathbf{W} + \alpha (\mathbf{D}_x^T \mathbf{D}_x + \mathbf{D}_y^T \mathbf{D}_y))^{-1} \mathbf{W}^T \mathbf{y}, \quad (2.49)$$

$$\hat{\mathbf{x}}_{TIK} = \mathbf{\Pi}_{TIK} \mathbf{y},$$

$$\mathbf{\Pi}_{TIK} = (\mathbf{W}^T \mathbf{W} + \alpha (\mathbf{D}_x^T \mathbf{D}_x + \mathbf{D}_y^T \mathbf{D}_y))^{-1} \mathbf{W}^T. \quad (2.50)$$

Since the calculation of \mathbf{Q} does not require instantaneous measurements, it may be calculated in advance [12]. As Equation (2.50) shows, the image estimate $\hat{\mathbf{x}}_{TIK}$ can be decomposed by a linear transformation matrix $\mathbf{\Pi}$ and the RSS measurement vector \mathbf{y} .

The second method defines \mathbf{Q} as the inverse of the *a priori* covariance matrix \mathbf{C}_x , where \mathbf{x} is modeled as zero-mean multi-variate Gaussian $\mathbf{x} \sim \mathcal{N}(\mathbf{0}, \mathbf{C}_x)$, and the movement of targets within a network is assumed to resemble a Poisson process such that,

$$[\mathbf{C}_x]_{p_1, p_2} = \sigma_x^2 \exp\left(-\frac{d(p_1, p_2)}{\delta_c}\right), \quad (2.51)$$

where $d(p_1, p_2)$ is the distance between pixel p_1 and pixel p_2 , σ_x^2 is the variance of pixel attenuation or \mathbf{x} , and δ_c is a pixel correlation parameter that can be used to control the amount of smoothness in the linear transformation matrix [5]. This method is equivalent to assuming a Bayesian prior on \mathbf{x} where $f(x|y) = f(y|x)f(x)$, and solving for the Maximum A-posteriori Probability (MAP) estimate [49] such that:

$$\begin{aligned} \hat{\mathbf{x}}_{MAP} &= \underset{x}{\operatorname{argmin}} f(\mathbf{y}|\mathbf{x})f(\mathbf{x}), \\ \hat{\mathbf{x}}_{MAP} &= \underset{x}{\operatorname{argmin}} \left(\|\mathbf{W}\mathbf{x} - \mathbf{y}\|^2 + \sigma_x^2 \|\mathbf{x}\|_{\mathbf{C}_x^{-1}}^2 \right), \end{aligned} \quad (2.52)$$

where $\mathbf{y}|\mathbf{x} \sim \mathcal{N}(\mathbf{W}\mathbf{x}, \sigma_n^2 \mathbf{I}_M)$ and M is the number of unique two-way links. The linear transformation matrix is now defined by:

$$\mathbf{\Pi}_{MAP} = (\mathbf{W}^T \mathbf{W} + \sigma_n^2 \mathbf{C}_x^{-1})^{-1} \mathbf{W}^T, \quad (2.53)$$

where σ_n^2 is the noise variance and

$$\hat{\mathbf{x}}_{MAP} = \mathbf{\Pi}_{MAP} \mathbf{y}. \quad (2.54)$$

This form of regularization or estimation, was used in [5, 8, 17, 55–57]. Alternatively, [58] suggests the root inverse of the covariance matrix, $\mathbf{C}_x^{-\frac{1}{2}}$ in place of \mathbf{C}_x^{-1} in Equation (2.53).

Choosing α . In [29, 44, 45, 58], and [12], the regularization parameter α is chosen arbitrarily. However, in [49], the MAP estimate is not used as the final solution but as a means to derive a value for α that is based on the statistics of the environment. The larger α is, the impact of the regularization term is greater and less information is kept from the estimate, and vice versa. In *Tikhonov Regularization* where \mathbf{Q} is the inverse of the covariance matrix (i.e., MAP estimation assuming a *Bayesian* prior), α is chosen to be σ_n^2 .

The work in [61] proposes multiple methods for choosing α that incorporate known information from weight model matrix \mathbf{W} ; these methods are modified forms of *Tikhonov Regularization*, called *Scalar Regularization* and *Vector Regularization*. A new matrix that is a function of α is formed,

$$\mathbf{R}(\alpha) = \mathbf{W}^T \mathbf{W} + \alpha \mathbf{Q}, \quad (2.55)$$

and the linear transformation matrix becomes:

$$\mathbf{\Pi} = \mathbf{R}^{-1}(\alpha) \mathbf{W}^T \mathbf{y}. \quad (2.56)$$

Scalar Regularization

The Singular Value Decomposition (SVD) of $\mathbf{W}^T \mathbf{W}$ is used to impart further known information in to the estimation problem. The SVD is written as $\mathbf{U} \mathbf{\Lambda} \mathbf{V}^T$ where \mathbf{U} and \mathbf{V} are real unitary matrices, and $\mathbf{\Lambda} = \text{diag}(s_1, s_2, \dots, s_N)$ is the diagonal matrix containing the singular values of $\mathbf{W}^T \mathbf{W}$.

In *Scalar Regularization*, there are three options for the selection of α [61],

- *Mean* (s_i)
- *Mean* ($s_i \neq 0$)
- *Median* ($s_i \neq 0$)

Values of α chosen in the manner described above will displace zero or near zero singular values s_i with terms from the difference operator \mathbf{D} such that $\mathbf{R}(\alpha)$ is decomposed by

$$\mathbf{R}(\alpha) = \sum_{i=1}^N s_i \mathbf{u}_i \mathbf{u}_i^T + \hat{\alpha} \sum_{i=1}^N g_i \mathbf{f}_i \mathbf{f}_i^T, \quad (2.57)$$

where $\hat{\alpha}$ is chosen as explained above, and $\mathbf{Q} = \mathbf{U} \mathbf{G} \mathbf{F}^T$ is the SVD of the derivative matrix in Equation (2.47) such that \mathbf{u}_i and \mathbf{f}_i are the i th column vectors of \mathbf{U} and \mathbf{F} respectively [61].

Vector Regularization

In *Vector Regularization* another new matrix is formed using a combination of the unitary matrices from the SVD of $\mathbf{W}^T \mathbf{W}$ and the SVD of the *Tikhonov Matrix* \mathbf{Q} ,

$$\mathbf{Z} = \mathbf{V}^T \mathbf{Q} \mathbf{U}. \quad (2.58)$$

The diagonal elements of \mathbf{Z} can be used to modify $\mathbf{R}(\alpha)$ as:

$$\mathbf{R}(\alpha) = \sum_{i=1}^N (s_i + a_i) \mathbf{u}_i \mathbf{u}_i^T. \quad (2.59)$$

This new form of $\mathbf{R}(\alpha)$ can be used as is where each value of s_i is used or an additional option is to only use those values of s_i that are zero or near-zero [16].

Truncated Singular Value Decomposition

Truncated Singular Value Decomposition (TSVD) Regularization is described in [58] and is similar to *Scalar Regularization* where only $g < N$ singular values from $\mathbf{\Lambda}$ are used in the reconstruction, however they are not incorporated through the choice of α but directly through the linear transformation matrix,

$$\begin{aligned} \mathbf{\Pi}_{TVSD} &= \sum_{i=1}^{g < N} \frac{1}{s_i} \mathbf{u}_i \mathbf{u}_i^T, \\ &= \mathbf{U}_g \mathbf{\Lambda}^{-1} \mathbf{U}_g^T, \end{aligned} \quad (2.60)$$

and the image estimate is

$$\hat{\mathbf{x}}_{TVSD} = \mathbf{\Pi}_{TVSD} \mathbf{y}. \quad (2.61)$$

The results in [58] found this form of regularization to result in images which were much noiser than those formed using *Tikhonov Regularization* and *Total Variation (TV) Regularization*.

Total Variation

TV Regularization is a non-linear form of regularization where the cost function is described by:

$$f_{TV}(\mathbf{x}) = \frac{1}{2} \|\mathbf{W}\mathbf{x} - \mathbf{y}\|^2 + \alpha TV(\mathbf{x}), \quad (2.62)$$

where

$$TV(\mathbf{x}) = \sum_i |\nabla \mathbf{x}|_i, \quad (2.63)$$

and is the i th element of the gradient of \mathbf{x} which is approximated by the difference matrix \mathbf{D} [58]. This form of regularization requires an approximation for the gradient of \mathbf{x} which is used in order for the numerical optimization algorithm to converge reliably [58], such that:

$$TV(\mathbf{x}) \simeq \sum_i \sqrt{\|\nabla \mathbf{x}\|_i^2 + \beta^2}, \quad (2.64)$$

where β is an extremely small constant that accounts for the discontinuity of $\sqrt{\|\nabla \mathbf{x}\|_i^2}$ at 0. *TV Regularization* attempts to reduce the total variation of the signal, removing unwanted noise while preserving important details; ultimately the estimated image will have sharp edges and high contrast without much noise [58]. Unlike the previous forms of regularization, this method is significantly more computationally complex because of the need for numerical optimization.

Subspace Decomposition. Another method for estimating the image uses SVD and is referred to in the literature as *Subspace Decomposition*. The work in [29] defined two forms of motion experienced in an RTI network: *intrinsic* and *extrinsic* motion. Zhao and Patwari [29] compared similar experiments that only differed by the amount of impact from external elements such as wind and branches of a nearby tree, yet resulted in much different estimates. They cited the differences as a result of the *intrinsic* motion caused by the wind and tree which caused additional variance in the measured RSS in such a way that resembled noise. They decomposed the received measurement vector into two distinct signal components, $\mathbf{y} = \hat{\mathbf{y}} + \tilde{\mathbf{y}}$, where $\hat{\mathbf{y}}$ represents the intrinsic component and $\tilde{\mathbf{y}}$ is the *extrinsic* component which is caused by the motion from an obstruction in the network;

the actual focus of RTI. Through their research, they found that any motion seen in an empty network could be attributed to *intrinsic* motion and therefore could be identified and analyzed using calibration data.

First, an estimate of the covariance of the calibration data \mathbf{C}_{y_c} is calculated which is represented by the sample variance as defined in Equation (2.19) [29]. Then they perform SVD, $\mathbf{C}_{y_c} = \mathbf{U}\mathbf{\Lambda}\mathbf{U}^T$ to determine the *Eigenvectors* \mathbf{u}_i and values λ_i of \mathbf{C}_{y_c} . Next using Principal Component Analysis (PCA), Zhao and Patwari [29] discover the first g *Eigenvectors* \mathbf{u}_i point in the direction of the maximum variance in the calibration measurement which represents the *intrinsic* motion. Thus, they separate the unitary matrix \mathbf{U} into two sets: $\hat{\mathbf{U}} = [u_1, u_2, \dots, u_g]$ and $\tilde{\mathbf{U}} = [u_{g+1}, u_{g+2}, \dots, u_M]$ where $\hat{\mathbf{U}}$ is the *intrinsic* subspace and $\tilde{\mathbf{U}}$ is the *extrinsic* subspace. Using these subspaces to form projection matrices, they are able to project future RSS measurement vectors \mathbf{y} onto the *extrinsic* subspace as a means to reduce the effects of *intrinsic* motion on future results. The *intrinsic* and *extrinsic* signal components and projection matrices are described by:

$$\hat{\mathbf{y}} = \mathbf{\Pi}_I \mathbf{y} = \hat{\mathbf{U}} \hat{\mathbf{U}}^T \mathbf{y}, \quad (2.65)$$

$$\tilde{\mathbf{y}} = \mathbf{\Pi}_E \mathbf{y} = (\mathbf{I} - \hat{\mathbf{U}} \hat{\mathbf{U}}^T) \mathbf{y}, \quad (2.66)$$

where $\mathbf{\Pi}_I$ is the projection matrix for the *intrinsic* subspace, and $\mathbf{\Pi}_E$ is the projection matrix for the *extrinsic* subspace [29]. To obtain the final image estimate, the projection of the measurement vector onto the *extrinsic* subspace is used in place of \mathbf{y} in Equation (2.49),

$$\hat{\mathbf{x}}_{SUB} = \mathbf{\Pi}_{TIK} \tilde{\mathbf{y}}, \quad (2.67)$$

where a new linear transformation matrix can be defined as:

$$\begin{aligned} \mathbf{\Pi}_{SUB} &= \mathbf{\Pi}_{TIK} \mathbf{\Pi}_E, \\ \mathbf{\Pi}_{SUB} &= (\mathbf{W}^T \mathbf{W} + \alpha \mathbf{Q}^T \mathbf{Q})^{-1} \mathbf{W}^T (\mathbf{I} - \hat{\mathbf{U}} \hat{\mathbf{U}}^T). \end{aligned} \quad (2.68)$$

This method of estimation was also used in [48].

Weighted Least Squares. Another RTI image estimation technique reported in the literature is a form of *Weighted Least Squares* which uses the inverse of the covariance matrices of both the noise \mathbf{C}_n and the change in RSS \mathbf{C}_x [29]. In this method, the use of \mathbf{C}_x is justified in the *Bayesian* sense as described in the section covering *Tikhonov Regularization* and as was defined in Equation (2.51). Also included is the *Ledoit-Wolf estimator* as a means to define \mathbf{C}_n ,

$$\mathbf{C}_n = \nu\mu\mathbf{I} + (1 - \nu)\mathbf{C}_n^*, \quad (2.69)$$

where \mathbf{C}_n^* is the sample covariance matrix as described in Equation (2.19), μ is a scaling parameter for the identity matrix \mathbf{I} , and ν is a shrinkage parameter that shrinks the sample covariance matrix towards the scaled Identity matrix [29]. Assuming there is no *extrinsic* motion during the calibration period, Zhao and Patwari [29] approximate $\mathbf{C}_n^* = \mathbf{C}_{y_c}$. The modified cost function for this estimator is:

$$f_{WLS}(\mathbf{x}) = \|\mathbf{W}\mathbf{x} - \mathbf{y}\|_{\mathbf{C}_n}^2 + \|\mathbf{x} - \mathbf{x}_a\|_{\mathbf{C}_x}^2, \quad (2.70)$$

while \mathbf{x}_a can be included in the tracking period, and is therefore assumed to be zero here. The final image estimate is described by:

$$\hat{\mathbf{x}}_{WLS} = \mathbf{\Pi}_{WLS}\mathbf{y}, \quad (2.71)$$

where

$$\mathbf{\Pi}_{WLS} = (\mathbf{W}^T \mathbf{C}_n^{-1} \mathbf{W} + \mathbf{C}_x^{-1})^{-1} \mathbf{W}^T \mathbf{C}_n^{-1}. \quad (2.72)$$

Least Absolute Shrinkage and Selection Operator. Another form of estimation seen in the literature is a variation of *l1-minimization* referred to as *Least Absolute Shrinkage and Selection Operator (LASSO)* [51]. The associated cost function is defined as:

$$f_{LASSO}(\mathbf{x}) = \frac{1}{2} \|\mathbf{W}\mathbf{x} - \mathbf{y}\|^2 + \lambda \|\mathbf{x}\|_{l1}, \quad (2.73)$$

where $\|\mathbf{x}\|_{l1}$ is the *l1-norm* of \mathbf{x} and λ is a scaling parameter that regulates the amount of sparsity versus signal intensity. This method was used in [11].

2.4.3.5 Cylindrical Human Model.

In order to assess the accuracy of RTI images, a truth image must be generated for comparison. A model for a human obstruction that considers position, size, shape, and density would be ideal, but is difficult. A simple model found in the literature is that of uniformly attenuating cylinder with radius R_H . This model modestly attempts to consider position, size, and shape. The model of a human located at position $c_H = (x_H, y_H, z_H)$ yields the truth image \mathbf{x}_c :

$$x_{c,p} = \begin{cases} 1 & \text{if } \|(x, y, z)_p - c_H\| < R_H \\ 0 & \text{otherwise} \end{cases}, \quad (2.74)$$

where $\mathbf{x}_{c,p}$ is the center location of voxel p [12]. Another model seen in the literature is that of a sphere [49].

2.4.3.6 Cramer-Rao Lower Bound.

The Cramer-Rao Lower Bound (CRLB), the well-known lower bound on the variance of an unbiased estimator, is used in RTI as a lower bound on the estimation error. The work of Wilson and Patwari in [12] derives a pixel-by-pixel bound on $\hat{\mathbf{x}}_{TIK}$ in terms of estimating the attenuation field. It is described by:

$$\begin{aligned} COV[\hat{\mathbf{x}}_{TIK}] &\geq J_{pp}^{-1}, \\ J_{pp}^{-1} &= \left(\gamma \mathbf{W}^T \mathbf{W} + \mathbf{C}_{\mathbf{x}}^{-1} \right)_{pp}^{-1}, \end{aligned} \quad (2.75)$$

where J_{pp}^{-1} represents the diagonal elements of the Fisher Information Matrix (FIM) \mathbf{J} , and as such are the lower bounds on the Normalized Mean Squared Error (NMSE)_R for pixel p .

In [49], Martin et al. derive a lower bound on the estimation of the obstruction's position, size, and attenuation based on a spherical obstruction model. And later on in [50], Martin et al. derive the CRLB in the form of compact scalar metrics for evaluating the weighting models in Equations (2.33), (2.34), (2.35), (2.37), (2.38) as a function of voxel size, test area size, number of sensors, amount of regularization, and various other model parameters.

2.5 Chapter Summary

This chapter explained the most basic forms of geolocation leading up to the exploration of DFL. Furthermore, the various signal propagation models, measurement modalities, and weighting models for RTI that exist in the literature were explained. Lastly, common estimation and regularization techniques for sparse signal reconstruction were presented. More specifically, the models used in this research were explained, and include the *Linear Signal Propagation Model* as a system and measurement model, the *Line Model* for the purpose of attenuation weighting, and *Regularized Least Squares* with *Tikhonov Regularization* for image estimation and reconstruction.

III. Methodology

THIS chapter describes the methodologies used in this research to establish and collect data from an RTI network comprised of a number RFICs. The following sections outline the hardware and tools used, the research assumptions, the steps taken to simulate truth data, the design and implementation of experiments, and how the data post-processing is accomplished.

Throughout the next two chapters, when an RTI network exists in 3-D the data will be discussed in terms of a volume or voxel of size $[\Delta_p \times \Delta_p \times \Delta_p]$, while for a 2-D RTI network the data will be discussed in terms of an area or pixel of size $[\Delta_p \times \Delta_p]$. Understanding the different terms in regard to dimensionality is most applicable for experiments focused on localizing and tracking the positions and movement of targets within the $x - y$ plane.

3.1 Equipment and Tools

The equipment used in this research includes the Memsic TelosB mote platform[62] and a laptop for data collection and processing. Many tools were used in this research and are described below. Data simulation and analysis were completed in MATLAB[®].

Memsic TelosB Mote Platform. The radios used in this research are made by Crossbow Technology Incorporated (Inc.) based out of San Jose, California. The chosen model is the TelosB mote TPR2420, an open-source platform developed for experimental use in the research community by University of California (UC) Berkeley as shown in Figures 3.1 and 3.2. The TPR2400 includes an Institute of Electrical and Electronics Engineers (IEEE) 802.15.4 compliant, 250 kilobits per second (kbps) high data rate radio with an integrated antenna, and a low-power 8 megahertz (MHz) Microcontroller Unit (MCU) with 10 kilobytes (kB) of Random Access Memory (RAM). This radio offers

programming and data collection via a Universal Serial Bus (USB) interface. It has a maximum range 100 meters outdoors or 30 meters indoors.

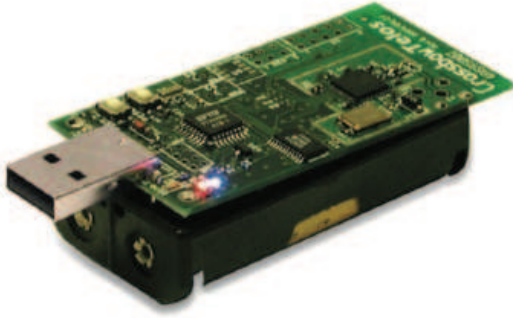


Figure 3.1: TelosB Mote.

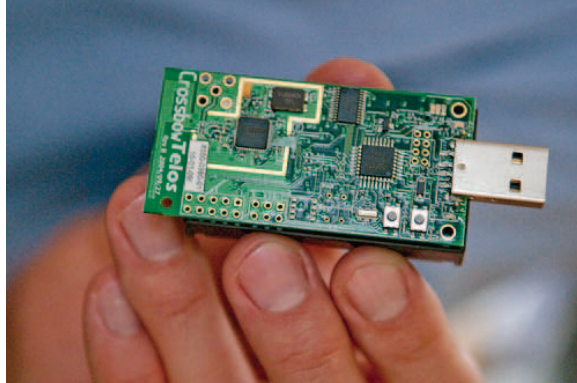


Figure 3.2: Size Demonstration.

The TPR2420 operates in the frequency range of 2.4000 gigahertz (GHz) to 2.4835 GHz. This band is one of several bands called the Industrial, Scientific and Medical (ISM) bands, as defined by the International Telecommunication Union (ITU). The radio draws up to 25 milliamps (mAs) of current, and uses up to 1 milliwatt (mW) of power for radio transmission. Each radio mote can be powered by two AA batteries or via the USB interface. The datasheet containing additional specifications for this platform is available at [62].

Cygwin. The motes were programmed using *Cygwin* on a *Microsoft Windows*[®] 7 64-bit laptop machine. *Cygwin* is a large collection of GNU and open-source tools which provide functionality similar to a Linux distribution on *Microsoft Windows*[®] [63].

TinyOS. The TelosB motes were equipped with the *Tiny Operating System (OS)* open-source, Berkely Software Distribution (BSD)-licensed OS written in NesC [64]. *TinyOS* includes the program file titled “BaseStation,” for programming the mote acting as the network *BaseStation*.

Spin. The deployed motes within the network were loaded with the program “Spin,” created by the Sensing and Processing Across Networks (SPAN) lab at the Department of Electrical and Computer Engineering at the University of Utah. *Spin* is an open-source *TinyOS* program written in NesC that collects RSS information from a WSN using a token passing protocol. With the token passing protocol, nodes transmit sequentially rather than at the same time; making the network more robust to lost packets. To download or read more about the *Spin* program refer to [65].

RTI LINK GUI. Data was collected using the *RTI LINK Graphical User Interface (GUI)* created by Mr. Alex Folkerts (Southwestern Ohio Council for Higher Education (SOCHE) Intern), Mr. Tyler Heintz (SOCHE Intern), and Dr. Richard K. Martin (Associate Professor of Electrical Engineering at the Air Force Institute of Technology (AFIT)). The *RTI LINK GUI* is a MATLAB[®] based application designed to collect and save RTI data while also allowing the user to view the data in near-real time while the experiment is conducted. The GUI parses the raw hexadecimal data written in two’s complement collected by the *BaseStation*, and converts it into a signed integer in the form of link RSS. The collection of unique link RSS measurements is the vector $\mathbf{y} = [y_1, y_2, \dots, y_M]^T$. The GUI implements the user-specified models and parameters, and estimates the change in RSS, \mathbf{x} , providing immediate feedback. The final data was saved in the form of raw link RSS measurements to provide further flexibility in comparing the impacts of regularization and pixel size.

3.2 Assumptions

The following are the assumptions that were made in this research:

1. $P_l \sim \mathcal{N}(\bar{P}(d_l), \sigma^2)$.
2. $\mathbf{n} \sim \mathcal{N}(\mathbf{0}, \sigma_n^2 \mathbf{I}_M)$
3. $\mathbf{y}|\mathbf{x} \sim \mathcal{N}(\mathbf{W}\mathbf{x}, \sigma_n^2 \mathbf{I}_M)$
4. $\mathbf{x} \sim \mathcal{N}(\mathbf{0}, \mathbf{C}_x)$ where \mathbf{C}_x is described by Equation (2.51)
5. Calibration data for the network is available.

6. Radios are oriented in a manner leading to the most effective and efficient use of antenna gain.
7. Obstructions in the network affect signal propagation strictly through RSS attenuation as a result of shadowing losses.
8. Shadowing losses caused by an obstruction maintain a constant spatial impact area regardless of the obstruction's location within the network.
9. Fade loss as a result of multipath is insignificant and not included in the chosen measurement and weighting models.
10. Measurement noise and static losses are insignificant and are averaged out over time.
11. Assets tracked during experiments monitoring resource usage are upright.
12. The number of targets is known.
13. The height of a target is known for 3-D position estimation. It is not assumed in attenuation image estimation and not used in motion tracking.
14. RSS attenuation is uniform over the area of a pixel (or volume of a voxel).
15. The use of filters (adaptive or otherwise) are not used in the control of noise related effects, motion tracking, or obstruction modeling.

3.3 System Models

This research applied shadowing-based RTI using the *Linear Signal Propagation* model described in Section 2.4.3.1. The system model is defined by Equation (2.14), and the set of system equations and chosen measurement model are described by Equation (2.15). Using a linear model simplified signal recovery and reduced computational complexity.

The *Line* model was chosen for the weight model and selection matrix described in Section 2.4.3.3 and defined by Equation (2.34) because it is computationally cheap, but more importantly, because the resulting attenuation estimate intuitively accounts for the path lengths of links passing through the obstruction.

Signal recovery was achieved with a *Tikhonov Regularized Least Squares* solution using a first order difference operator for the *Tikhonov matrix* as defined by Equation (2.49); however, it was modified for use in a 3-D WSN. The regularization parameter α was selected after completing analysis of several single and dual stationary target experiments as described in Section 3.7. The results of this analysis are presented in Chapter 4.

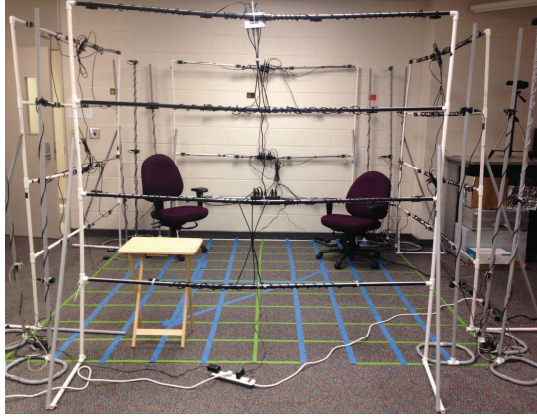
In summary:

- System Model: $\mathbf{y} = \mathbf{W}\mathbf{x} + \mathbf{n}$
- Measurement Model: $\mathbf{y} = [\Delta r_1, \Delta r_2, \dots, \Delta r_M]^T$
- Calibration: $\mathbf{y}_c = [\bar{r}_{c,1}, \bar{r}_{c,2}, \dots, \bar{r}_{c,M}]^T$
- Weight Model: $[\mathbf{W}]_{l,p}^{Line} = L_{l,p} \begin{cases} 1 & \text{if link } l \text{ traverses voxel } p \\ 0 & \text{otherwise} \end{cases}$
- Estimator: $\hat{\mathbf{x}}_{TIK} = \underset{x}{\operatorname{argmin}} \left(\|\mathbf{W}\mathbf{x} - \mathbf{y}\|^2 + \alpha \|\mathbf{Q}\mathbf{x}\|^2 \right)$
- Tikhonov Matrix: $\mathbf{Q} \triangleq \mathbf{D}_x^T \mathbf{D}_x + \mathbf{D}_y^T \mathbf{D}_y + \mathbf{D}_z^T \mathbf{D}_z$

3.4 Network Setup

The RTI network covered a [10 ft \times 10 ft] area surrounded by 80 wireless motes mounted on structures made of Polyvinyl Chloride (PVC). Pictures of the network structure are shown in Figure 3.3. The floor was marked with Painters Tape in a [1 ft \times 1 ft] grid. Grid intersections represent voxel center coordinates. An illustration of the grid is shown in Figure 3.4.

There were four rows of motes along the z-axis at the heights $z = [1.71, 3.42, 5.12, 6.83]$ ft. For each row of motes, the lateral separation between motes was 2 ft in both the x and y directions; however the first and third layer of motes were staggered in placement from the second and fourth rows. Various views of the mote topology can be seen in Figures 3.4 and 3.5.

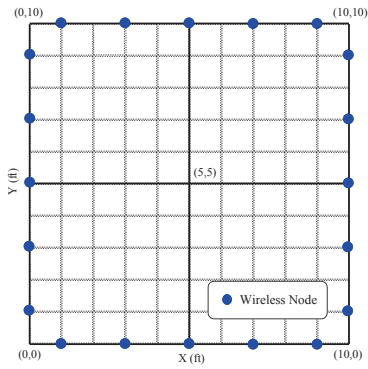


(a) Lateral View

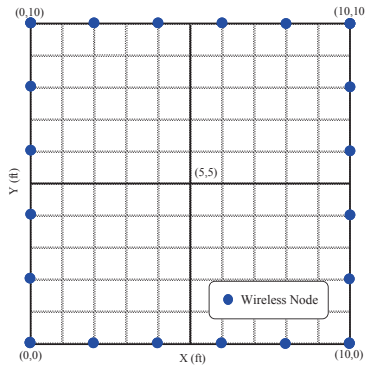


(b) Corner View from (10,10)

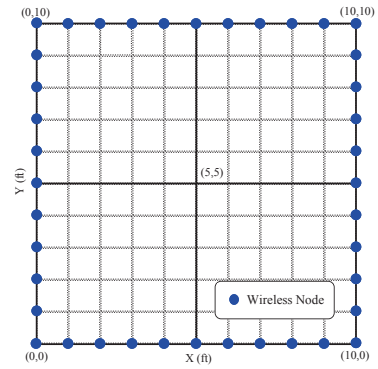
Figure 3.3: Experimental RTI network structure.



(a) First and Third Rows



(b) Second and Fourth Rows



(c) All Rows Included.

Figure 3.4: Aerial view of mote topology.

The chosen mote topology provided ample coverage of the area contained within the network. Preliminary visualization of network coverage was possible using MATLAB[®] scripts which plotted relative coverage patterns from various possible mote topologies. Additionally, the use of a 3-D network provided significantly higher link density versus what would be seen in a 2-D network. Link density leads to an increase in available RSS

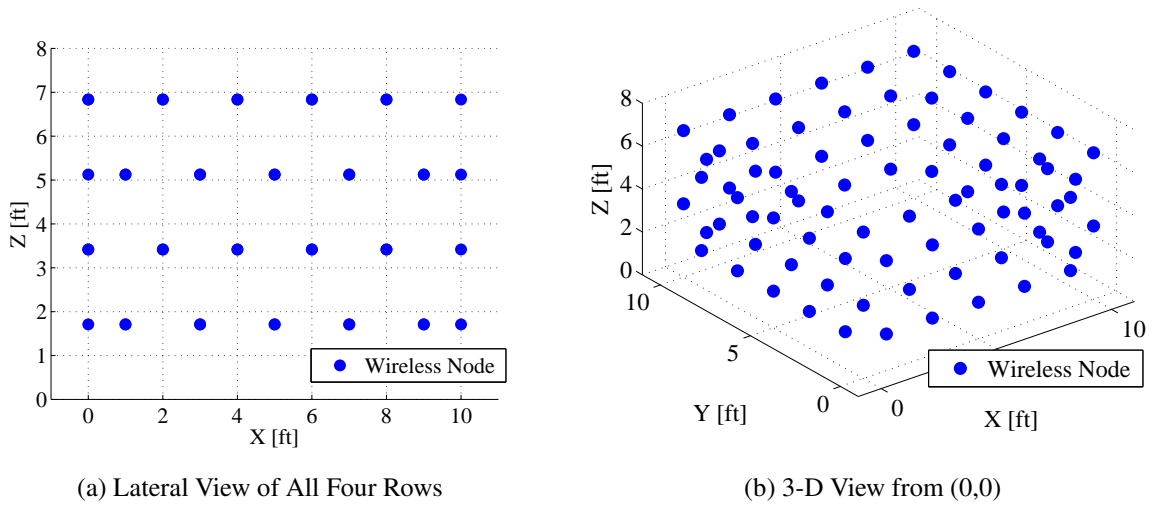


Figure 3.5: Lateral and three-dimensional views of mote topology.

information from the network. Multiple dimensions are exploited when RSS measurements are averaged along the z -dimension to locate an obstruction on the $x - y$ plane, ultimately compressing three-dimensions into two-dimensions. The 3-D network also provided an opportunity to explore 3-D images generated from RTI and how the network performed in various dimensions with a human obstruction present. Images illustrating the link density of the network are shown in Figures 3.6 and 3.7.

Another motivation behind the chosen mote topology was the respective voxel-by-voxel lower-bound of the variance of the linear estimator. As with an MLE, the CRLB is a means of representing the performance of the actual estimator since the CRLB is equal to the variance [50]. Applying the derivation of the CRLB as described in Section 2.4.3.6 and using the parameters in Table 3.1; the voxel-based bound can be visualized in a 3-D scatter-plot as seen in Figure 3.8a. To reduce the clutter in the figure, only values within the top 10% of the maximum value are kept as shown in Figure 3.8b. Using the derived form of the CRLB only considers the estimator's ability to estimate the change in RSS

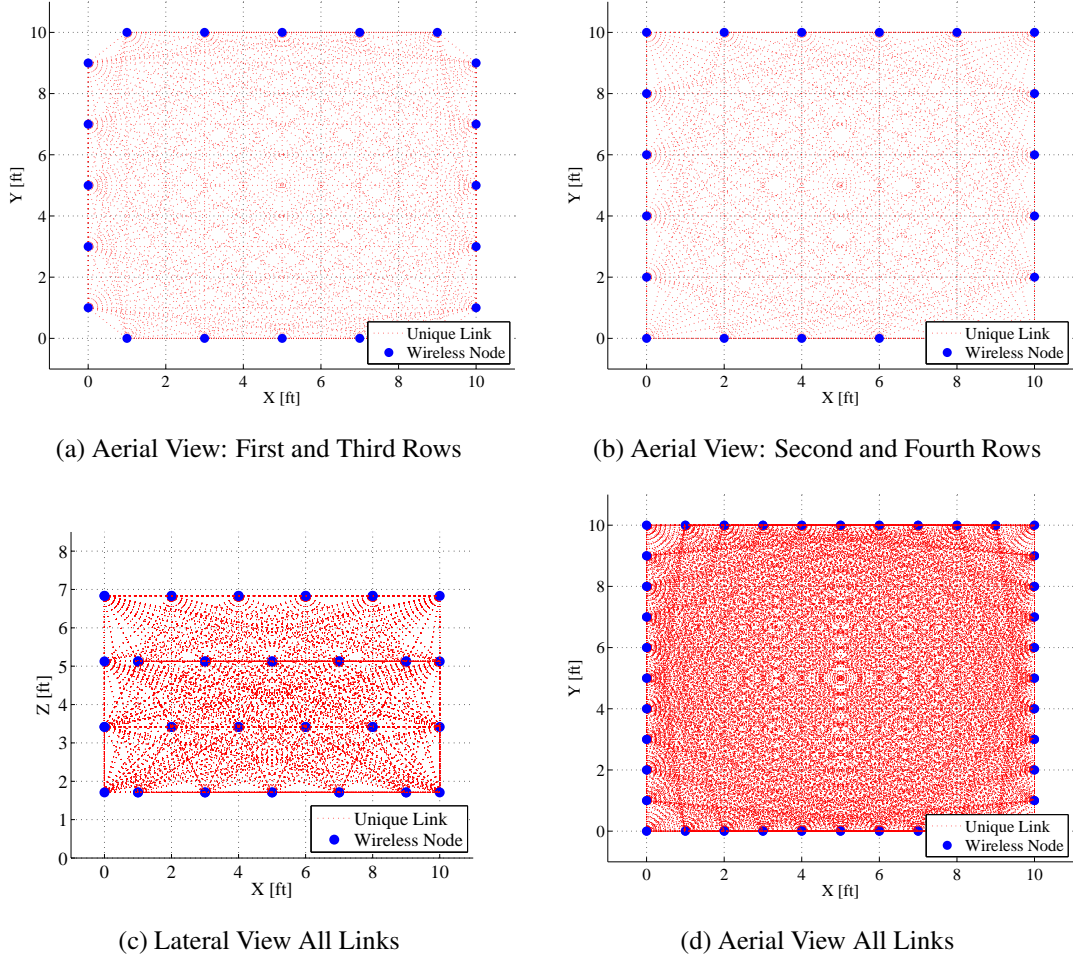


Figure 3.6: Three-dimensional views of link coverage.

where another form of CRLB could provide insight into the estimator's ability to estimate an object's position, size, and attenuation.

To further simplify the interpretation of the CRLB as it applies to a 3-D network, the mean, variance, and maximum value in the z -dimension are considered and shown in the surface plots shown in Figure 3.9, essentially compressing the information. The ability to understand the estimator's performance in the $x - y$ plane is more useful for this research

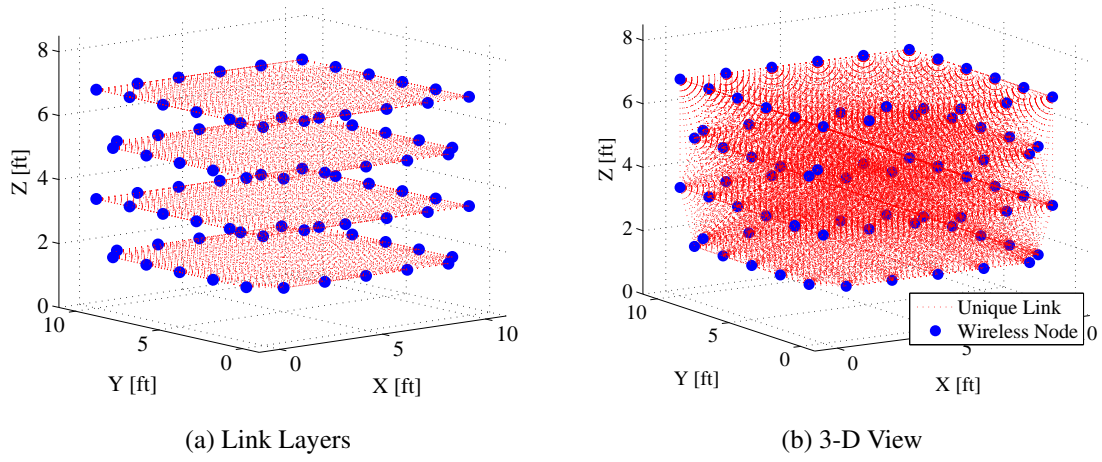


Figure 3.7: Two-dimensional views of link coverage.

Table 3.1: CRLB Construction Parameters.

Parameter	Value	Description
Δ_p	1.0	Voxel width (ft)
δ_c	4.27	Voxel correlation constant (ft)
σ_x^2	0.1	Voxel variance (dB^2)
γ	0.5483	Bound parameter
R_H	1.1	Human radius for cylindrical model (ft)

since the focus lies in the ability of the estimator to accurately locate and track a grounded obstruction within the network which occupies multiple levels in the z -dimension.

Figure 3.9a illustrates the average expected variance of the estimator's performance, while Figure 3.9b shows the amount of variation to be expected in the variance of the estimator (i.e., higher variance in the bound leads to areas that may be less predictable in estimating attenuation). Lastly, Figure 3.9c illustrates the maximum variance that is experienced along the z -axis throughout the network. The ability to analyze the CRLB and

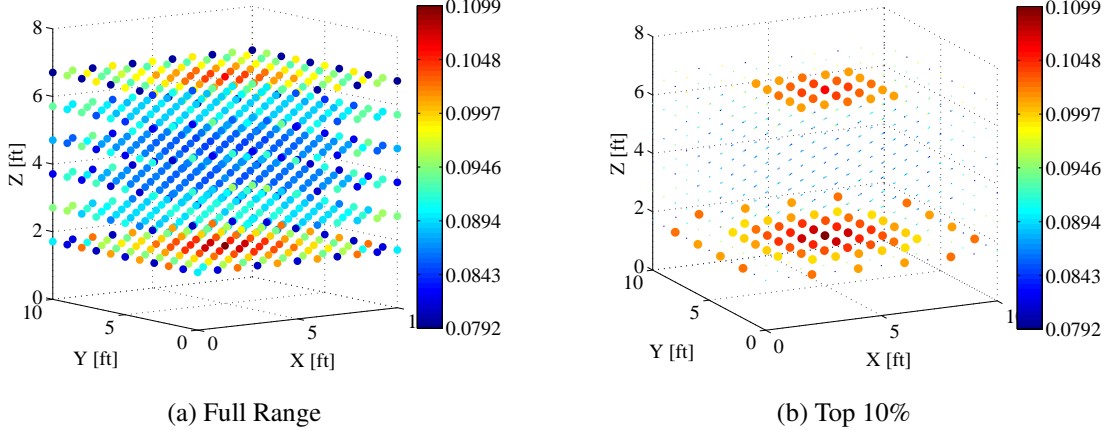


Figure 3.8: \sqrt{CRLB} volume $[\frac{dB}{f^2}]$.

link coverage for various topologies before hand eliminated the need for trial and error, and enabled a more educated approach in deciding sensor placement before constructing the network.

Radio Orientation. Referring to specifications for the Inverted-F Antenna (IFA) in the TelosB TPR2420 located at [66], orienting the motes horizontally in the network aligned with the most effective antenna gain pattern.

Human Subjects. Human subjects were used in this research. Required training has been completed by the principal investigators, and the AFIT RTI protocol approved by the Air Force Research Laboratory (AFRL) Institutional Review Board (IRB). Each subject was briefed, signed an Informed Consent Document (ICD), and voluntarily participated in experiments.

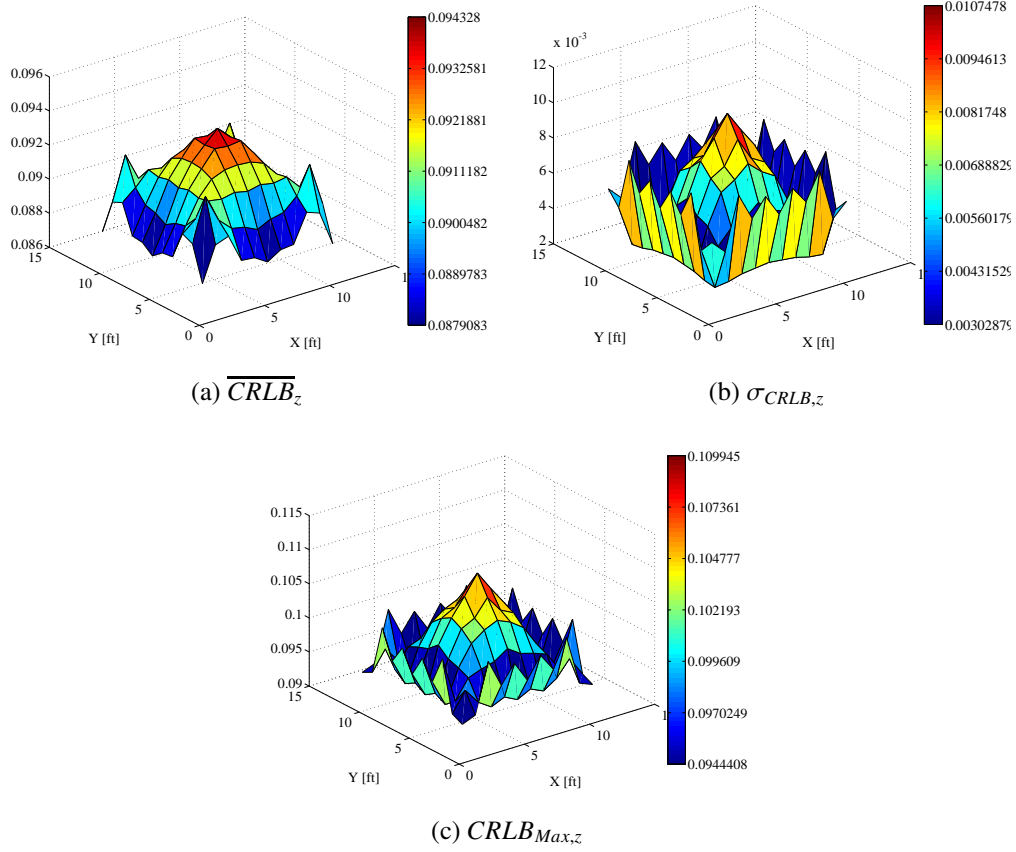


Figure 3.9: Analysis of the \sqrt{CRLB} along the vertical dimension $[\frac{dB}{fr^2}]$.

3.5 Choosing Model and Experiment Parameters

Model parameters α and Δ_p , were chosen after review of existing results from trade-off analysis conducted for similar networks in [12, 50], and a series of controlled preliminary experiments. Data from these experiments were analyzed using a range of values for α and Δ_p and the resulting Mean Squared Error (MSE) for each data set was compared.

3.6 Simulated Truth Data

The *Cylindrical Human model* described in Section 2.4.3.5 was used to generate the truth attenuation images for stationary targets such that c_H is set to be the known $(x, y, z)_{sT}$

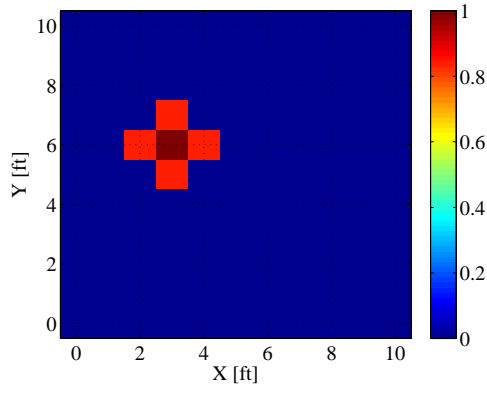
coordinates of the stationary targets to be localized,

$$[\mathbf{x}]_{CHM,p} = x_{CHM,p} = \begin{cases} 1 & \text{if } \|(x, y, z)_p - c_H\| < R_H \\ 0 & \text{otherwise} \end{cases}, \quad (3.1)$$

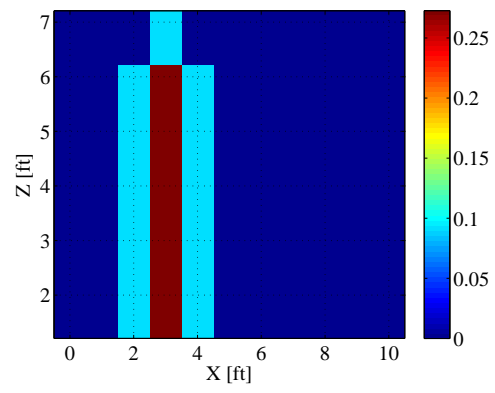
where the true attenuation image, $\mathbf{x}_{CHM,Targets}$ is a $[L_x, L_y, L_z]$ matrix consisting of ones in the voxels occupied by the cylindrical model centered on c_H with radius R_H and zeros elsewhere. The dimensions $[L_x, L_y, L_z]$ represent the number of voxels in the x , y , and z dimensions respectively. Since the size of the modeled cylinder depends upon R_H , the number of voxels set to one may include those bordering the voxel centered on c_H . The truth matrix, \mathbf{x}_{CHM} is compressed along the z -axis into a matrix of size $[L_x, L_y]$ to compare to the 2-D aerial view of the estimated attenuation image for stationary localization. Additionally, the truth matrix is compressed along the y -axis rendering a matrix of size $[L_z, L_x]$ to compare the 2-D lateral view of the estimated attenuation image for stationary localization. For each of 2-D matrix, the voxels are compressed to pixels. For a target's true 3-D position, the known $x - y$ position is replicated along the z -dimension relative to the target's height. The target's height is rounded toward infinity to account for the target's presence in a pixel or voxel regardless of the amount in conjunction with the assumption that attenuation caused by a target is uniform throughout the pixel or voxel. Therefore, the height illustrated in a true attenuation image and position will be in respect to pixel or voxel size. The target's true 2-D and 3-D position is discretized and centered in the respective pixel or voxel the target occupies.

Simulated truth data for motion tracking did not utilize the *Cylindrical Human model*. Instead a matrix \mathbf{x}_mT of the size $[L_x, L_y]$ was created simply by setting only those pixels to one, whose center coordinates were either the known positions $(x, y)_{sT,Targets}$, or were included in the known target path $(x, y)_{mT,path}$ and all others were set to zero. In exploring 3-D RTI networks, the target's height was considered when generating truth images, image estimates, and position estimates for stationary targets. The target's height was

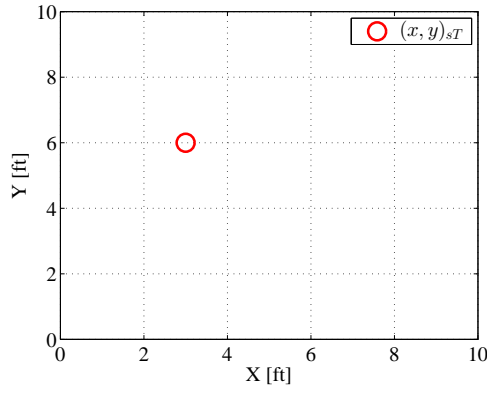
not considered in data analysis for motion tracking and spatial pattern monitoring truth data and experiments. Figures 3.10 and 3.12 show examples of the simulated truth images for a single stationary target and two stationary targets respectively where $\Delta_p = 1.0\text{ft}$. Figures 3.11 and 3.13 illustrates the same images but for a pixel size of $\Delta_p = 0.5\text{ft}$. Lastly, Figures 3.14 and 3.15 show examples of the simulated true paths for a single moving target for the controlled motion tracking experiments. Figures 3.15 and 3.16 show the simulated true paths and attenuation images used in the spatial pattern monitoring experiments which contained furniture obstructions.



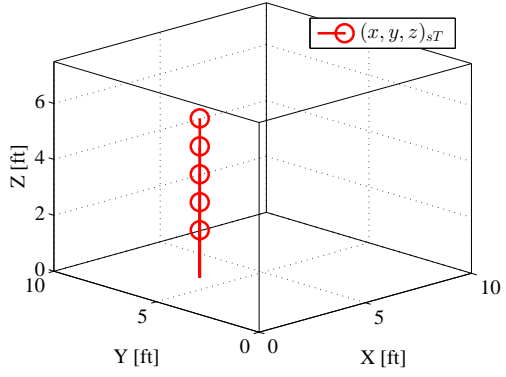
(a) Aerial View: $\mathbf{x}_{CHM,1}$



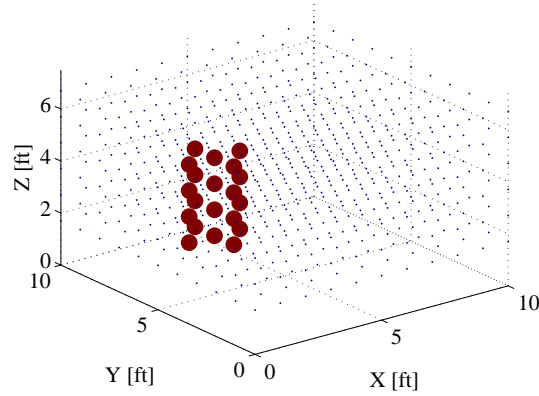
(b) Lateral View: $\mathbf{x}_{CHM,1}$



(c) 2-D Position: $(x, y)_{sT,1}$

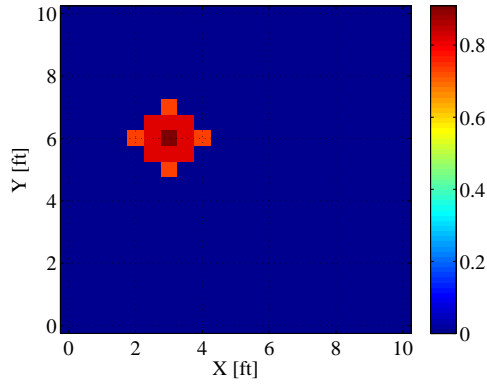


(d) 3-D Position: $(x, y, z)_{sT,1}$

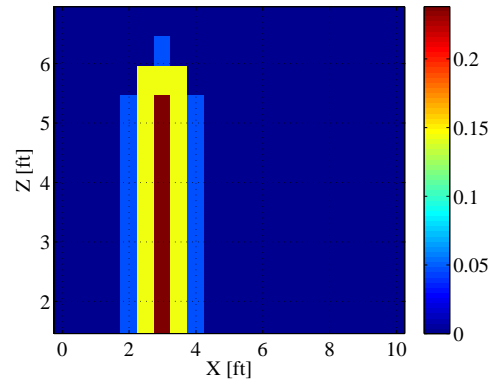


(e) 3-D View: $\mathbf{x}_{CHM,1}$

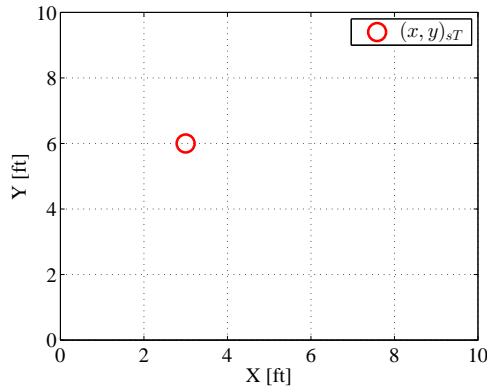
Figure 3.10: Truth Images: Single stationary target standing at $(x, y)_{sT,1} = (3, 6)$. Target height: 5'1". $\{\Delta_p = 1.0\text{ft}\}$



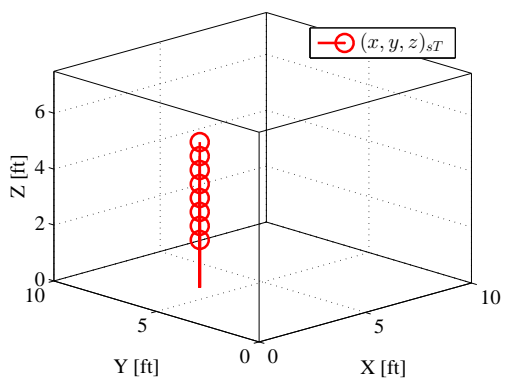
(a) Aerial View: $\mathbf{x}_{CHM,1}$



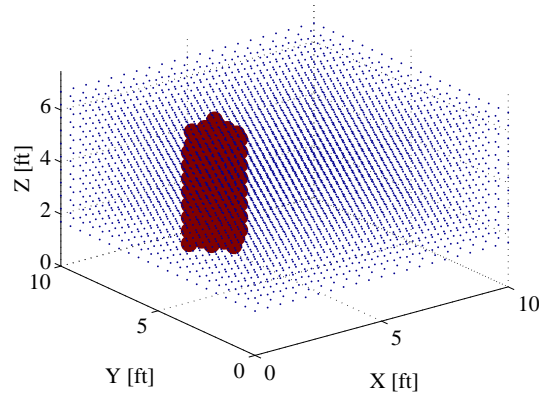
(b) Lateral View: $\mathbf{x}_{CHM,1}$



(c) 2-D Position: $(x, y)_{sT,1}$

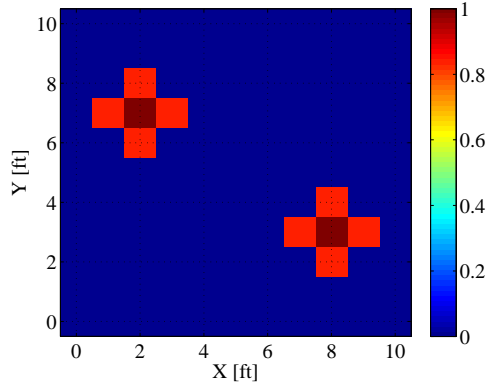


(d) 3-D Position: $(x, y, z)_{sT,1}$

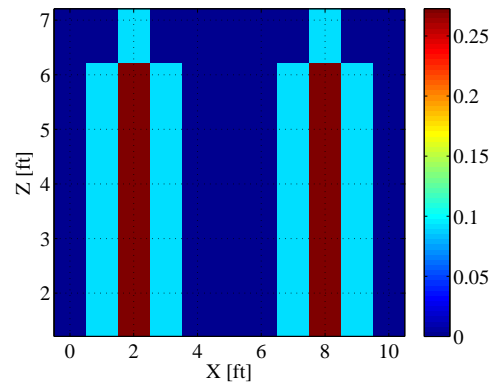


(e) 3D View: $\mathbf{x}_{CHM,1}$

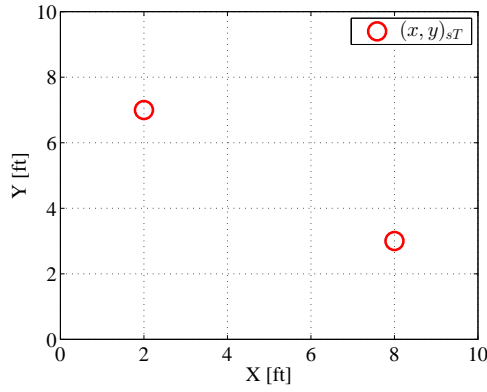
Figure 3.11: Truth Images: Single stationary target standing at $(x, y)_{sT,1} = (3, 6)$. Target height: 5'1". $\{\Delta_p = 0.5\text{ft}\}$



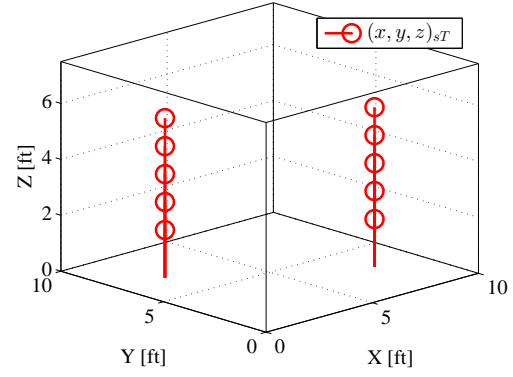
(a) Aerial View: $\mathbf{x}_{CHM,2}$



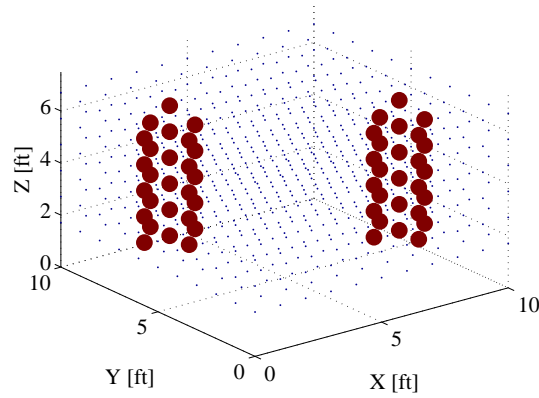
(b) Lateral View: $\mathbf{x}_{CHM,2}$



(c) 2-D Position: $(x, y)_{sT,2}$

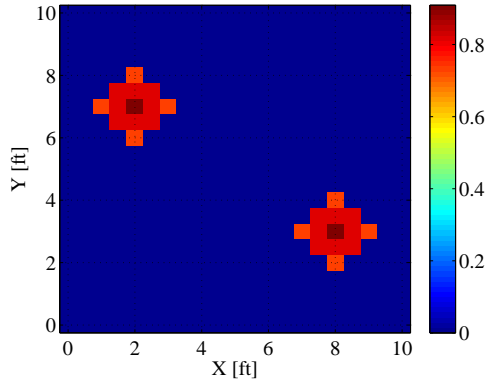


(d) 3-D Position: $(x, y, z)_{sT,2}$

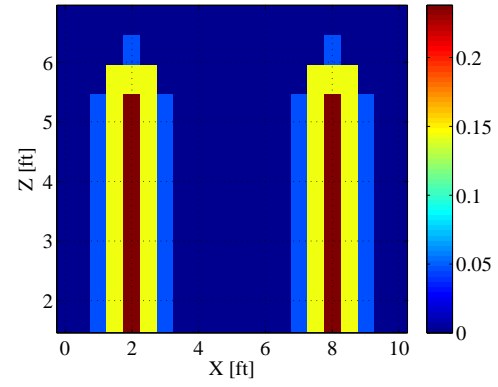


(e) $\mathbf{x}_{CHM,2}$

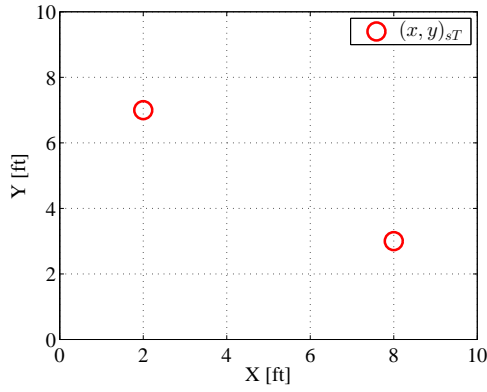
Figure 3.12: Truth Images: Two stationary targets standing at $(x, y)_{sT,1} = (2, 7)$ and $(x, y)_{sT,2} = (8, 3)$. Target heights: 5'8" and 5'5". $\{\Delta_p = 1.0\text{ft}\}$



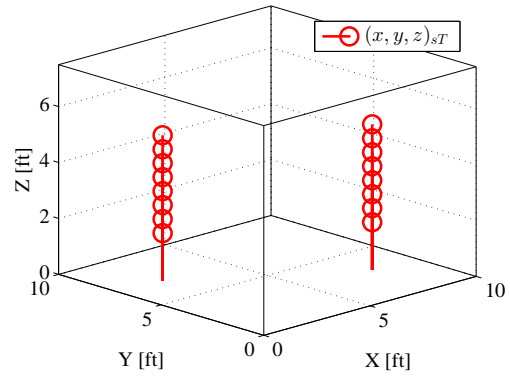
(a) Aerial View: $\mathbf{x}_{CHM,2}$



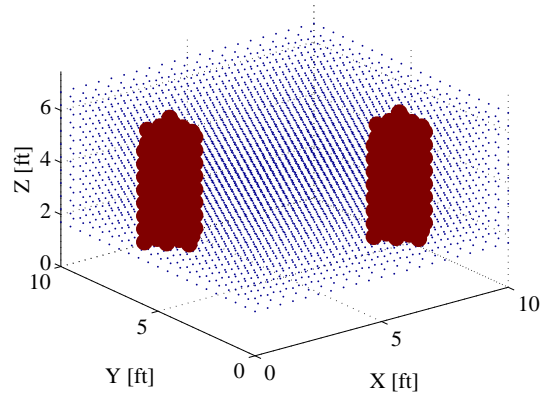
(b) Lateral View: $\mathbf{x}_{CHM,2}$



(c) 2-D Position: $(x, y)_{sT,2}$

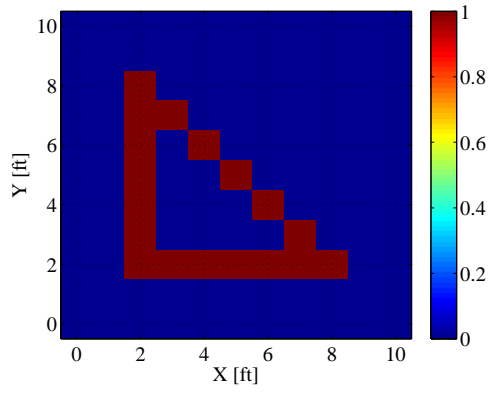


(d) 3-D Position: $(x, y, z)_{sT,2}$

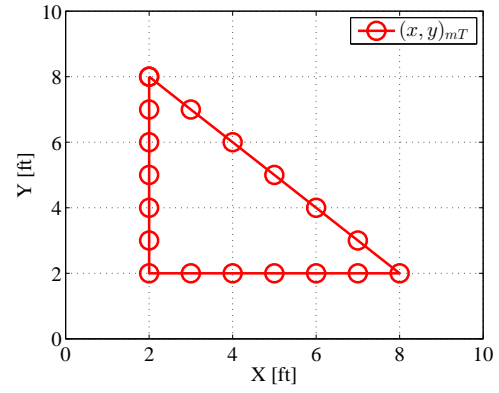


(e) 3-D View: $\mathbf{x}_{CHM,2}$

Figure 3.13: Truth Images: Two stationary targets standing at $(x, y)_{sT,1} = (2, 7)$ and $(x, y)_{sT,2} = (8, 3)$. Target heights: 5'8" and 5'5". $\{\Delta_p = 0.5\text{ft}\}$



(a) Aerial View: \mathbf{x}_{mT}



(b) 2-D Path: $(x, y)_{mT}$

Figure 3.14: Time Averaged 2-D Truth Images: Single target motion tracking over triangle path $(x, y)_{mT} = (2, 8) - (2, 2) - (8, 2)$ without obstructions. $\{\Delta_p = 1.0\text{ft}\}$

3.7 Experiment Design

This research utilized a series of experiments broken into several categories focused on stationary localization of a single target and multiple targets, motion tracking of a single target, and spatial pattern monitoring using a single target and multiple targets in both obstructed and non-obstructed environments. One experiment is defined as a single data collection period within one of the defined experiment categories. Within each experiment, model parameters were controlled and logged, and a set of truth data was created using the means described in Section 3.6 to match the hypothesized results for the purpose of error analysis. Network calibration was conducted for each experiment prior to starting, while the network was empty of any targets, and only permanent obstructions were in place if they were to be included in the subsequent experiment; link RSS measurements were taken for approximately 1 minute as time was tracked using the same watch.

Stationary Localization. Controlled experiments for stationary target localization were conducted as a means to verify network reliability and explore 3-D RTI. The focus was on verifying the network's ability to localize a target. A total of 70 experiments were conducted; the variations between the experiments included the number of targets; target height, size, and position; and the presence of permanent obstructions. A table of the experiment statistics can be seen in Table 3.2. The only other variation was in the last two experiments listed in the table; the first consisted of the targets sitting while the second had the targets standing.

For each experiment within the stationary localization category, targets remained stationary at predetermined coordinates for a total of 30 seconds, and the same set of targets was used each time. Examples of the truth images are shown in Figures 3.10, 3.11, 3.12, and 3.13.

Table 3.2: Stationary Localization Experiments.

Number of Experiments	Number of Targets	Target Height	Target Orientation	$(x, y)_{sT}$	Obstructions
8	1	5'1"	Standing	(3,6)	No
2	1	5'8"	Standing	(3,6)	No
2	1	6'1"	Standing	(3,6)	No
5	1	5'1"	Standing	(3,6)	Yes
10	1	5'1"	Standing	(7,5)	No
5	1	5'1"	Standing	(7,5)	Yes
5	1	5'1"	Standing	(7,6)	Yes
4	2	5'8" / 5'5"	Standing	(5,2) / (7,6)	No
1	2	5'8" / 5'5"	Standing	(5,2) / (7,6)	Yes
1	2	5'8" / 5'5"	Sitting	(2,4) / (8,3)	Yes

Motion Tracking. Following network verification, a series of experiments for motion tracking were conducted in a similar fashion to the stationary localization experiments. In order to be able to compare results between each experiment, a metronome was used to regulate the pace of moving targets within the network to ensure it was consistent between experiments. The paths for these experiments were selected for the purpose of ensuring the network was adequately covered and hot-spots, such as the network's center and borders, were included.

Within the category of tracking a single target moving through the network, there were a total of 20 experiments. There were three paths used, two of which were also utilized when collecting spatial pattern data. The initial set of experiments were conducted using various metronome tempos in beats per minute (BPM). to determine a moving pace that balanced realism and experimental control. The breakdown of these experiments is presented in Table 3.3.

Link RSS data was collected only for as long as it took the target to travel the predetermined path. The results of these experiments aided in verifying the network could

accurately track moving targets and thus determine the frequency of a target's presence at a particular location within the network. Example truth images are shown in Figure 3.14.

Table 3.3: Motion Tracking Experiments.

Number of Experiments	Number of Targets	Target Height	$(x, y)_{mT}$	Metronome Tempo (BPM)	Obstructions
1	1	5'1"	(2,8)-(2,2)-(8,2)	35	No
1	1	5'1"	(2,8)-(2,2)-(8,2)	34	No
1	1	5'1"	(2,8)-(2,2)-(8,2)	33	No
10	1	5'1"	(2,8)-(2,2)-(8,2)	32	No
4	1	5'1"	(3,4)-(7,8)	32	Yes
3	1	5'1"	(7,3)-(7,8)	32	Yes

Monitoring Spatial Patterns. Finally, the last set of experiments were designed based on the previous work from Section 3.7, with the ultimate focus of answering the question posed in Section 1.3: “Can an indoor RTI network be used to monitor resource usage within a room?” In the context of this research, spatial pattern monitoring aims to track the movements of assets in an office environment in order to determine high traffic areas. With this information, leadership may make informed decisions on office layout to increase productivity and efficiency. These concepts dictated the design of each experiment. It was important to maintain parameter control such that each experiment could build on top of the previous one. With that said, the stationary localization and motion tracking experiments were conducted to verify the effective use of RTI in each of the different aspects contributing to spatial pattern monitoring.

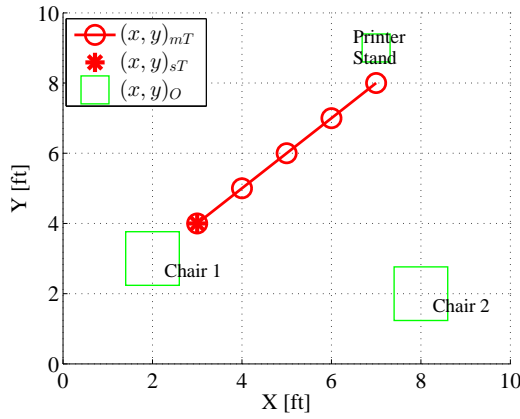
Six distinct experiments were conducted under the spatial pattern monitoring category. The first and second experiments consisted of a single asset in an obstructed network. The obstructed network consisted of a two padded office chairs and a small folding table. A primary position was defined as the location where the asset remained while not moving through the network. The purpose of the primary positions was to act as the assets' personal

work spaces where they are most frequently located throughout the workday. When the asset moved through the network, the same path, end point, and pace were used each time. The difference between the two experiments was the frequency of how often the asset walked the path. Varying trip frequency was necessary to demonstrate the ability to distinguish between varying high traffic areas. The third and fourth experiments were structured in the same manner; however, a different primary position was defined and a new path to the same end-point was used. The two primary positions and paths from these experiments were the same ones used in the next two experiments. The paths represent high traffic areas to a common focus point such as a printer.

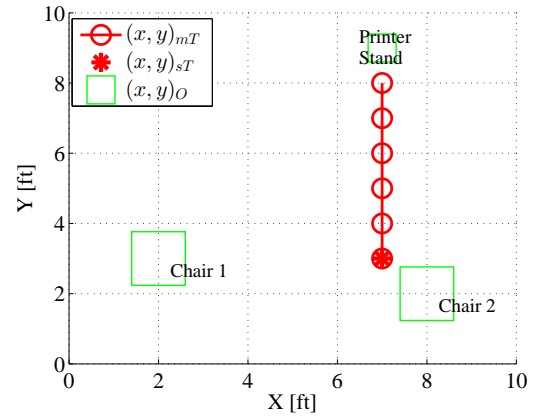
The last two experiments consisted of two assets; movement was coordinated in the same way the single asset experiments were and the same primary positions and paths were used. Between the two experiments, the only varying parameter was the trip frequency. In the first experiment, asset 1 made the trip down his/her respective path two times while asset 2 made the trip four times. This was reversed for the second experiment. In each of them, the same assets were used and assigned the same primary positions and paths respectively.

Table 3.4: Spatial Pattern Monitoring Experiments.

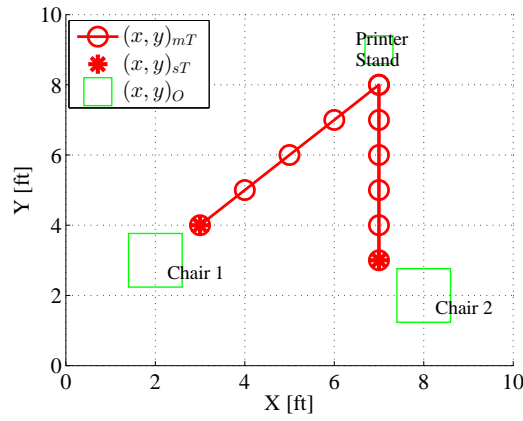
Number of Experiments	Number of Targets	Target Height	$(x, y)_{mT}$	λ_T	Metronome Tempo (BPM)	Obstructions
1	1	5'1"	(3,4)-(7,8)	2	32	Yes
1	1	5'1"	(3,4)-(7,8)	4	32	Yes
1	1	5'1"	(7,3)-(7,8)	4	32	Yes
1	1	5'1"	(7,3)-(7,8)	2	32	Yes
1	2	5'8"	(3,4)-(7,8)	2	32	Yes
		5'5"	(7,3)-(7,8)	4		
1	2	5'8"	(3,4)-(7,8)	4	32	Yes
		5'5"	(7,3)-(7,8)	2		



(a) $(x, y)_{mT,1} = (3, 4) - (7, 8)$



(b) $(x, y)_{mT,2} = (7, 3) - (7, 8)$



(c) $(x, y)_{mT,1,2}$

Figure 3.15: Truth Path: Motion tracking and spatial pattern monitoring with obstructions.

The motivation for using the same paths in each experiment was the ability to compare the results from different experiments. Additionally, if the experiment consisted of random movement or using different paths each time throughout the network it would not be possible to simulate the respective truth data based on hypothesized results. Controlling the paths taken and the trip frequency also made it possible to distinguish between false positives in terms of inaccurately identified occupied pixels. Each spatial pattern monitoring experiment lasted for 9 minutes. Illustrations of the true paths used in both the

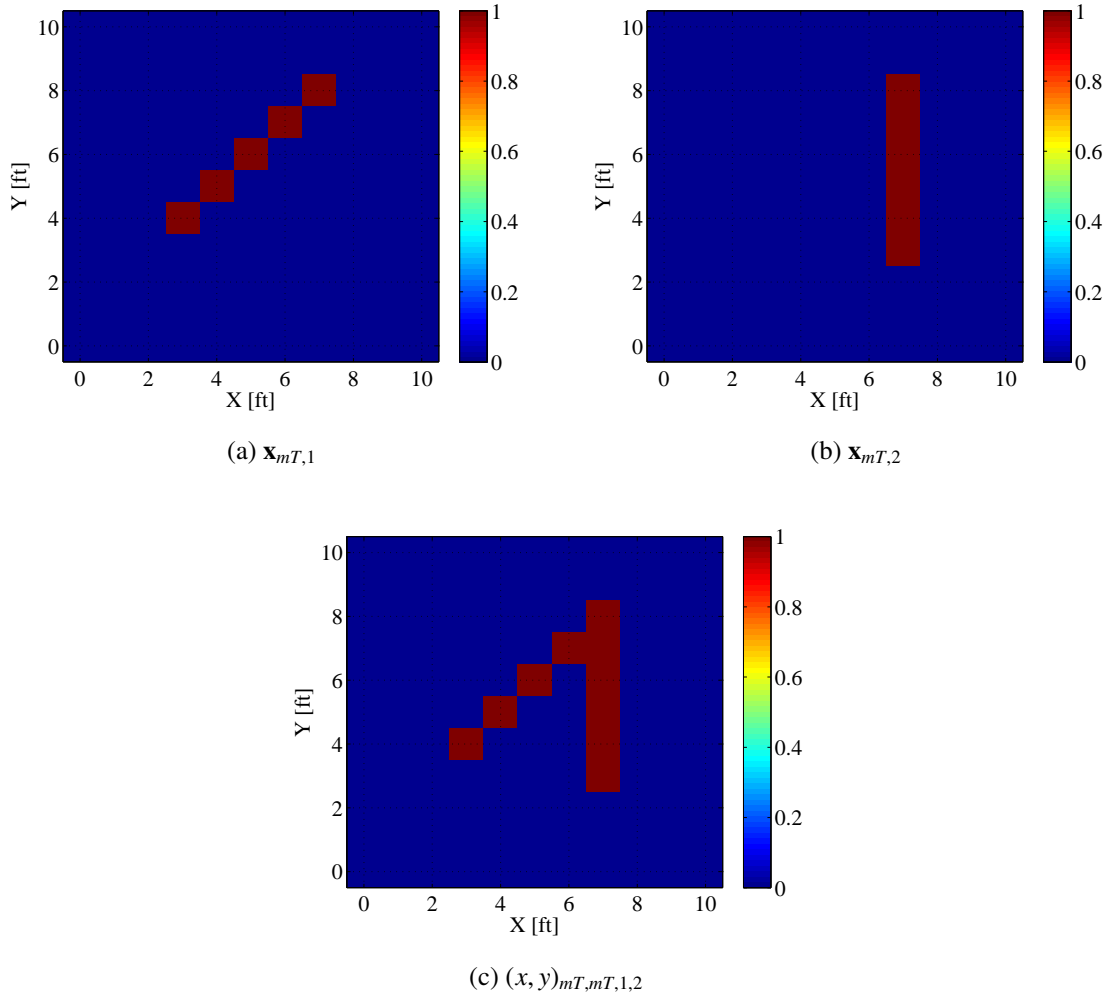


Figure 3.16: Time Averaged Aerial Truth Images: Motion tracking and spatial pattern monitoring with obstructions. $\{\Delta_p = 1.0\text{ft}\}$

motion tracking and spatial pattern monitoring experiments are shown in Figure 3.15. The time averaged aerial truth images that were used to compare with the pseudo attenuation image estimates generated from the same experiments are shown in Figure 3.16.

3.8 Data Analysis

All data analysis and processing was accomplished using MATLAB[®]. Most of the techniques used for data manipulation and processing were similar for each type of experiment; however, there were a few differences between the stationary localization experiments versus the motion tracking and spatial pattern monitoring experiments. For each experiment, the first and last three frames were removed from the data set to account for the period of time it took for assets to get positioned within the network. For each experiment, the collection of raw link RSS measurements was recorded using the *RTI LINK GUI*. Then the models listed in Section 3.3 were applied while varying α and Δ_p ; resulting in an attenuation volume estimate $\hat{\mathbf{x}}_{TIK}$ for each data set. Next, the processing techniques described below were utilized on the estimates relative to the experiment type.

Stationary Target Localization. In stationary target localization, the goal is to correctly identify the position a target is standing in. The first step is to compute the sample average of the data set across all frames. The result is a 3-D volume of estimated voxel attenuation of the size $[L_x, L_y, L_z]$. A 3-D position estimate is determined from the 3-D voxel attenuation matrix by locating a single maximum value in each $x - y$ plane. Next, the attenuation estimate is compressed in two different ways. First, by determining the mean along the vertical dimension z providing an aerial view of the estimated 2-D attenuation image, and the second by determining the mean along the lateral dimension y providing a lateral view of the estimated 2-D attenuation image. Compressing the data along the z -axis results in 2-D estimates and therefore voxels are reduced to pixels. Additionally, due to the sporadic nature of RTI, pixels can be incorrectly identified as occupied; false-positives happen infrequently and are negligible.

Compressing the data now results in a $[L_x, L_y]$ matrix of estimated pixel attenuation in the $x - y$ plane. A search for the maximum value results in a (x, y) position estimate. Attenuation is assumed to be uniform over the entire area of the pixel (or volume of the

voxel); therefore, the target's estimated position is generalized to be the center of the respective pixel or voxel, when the target's true position could be anywhere within the pixel or voxel. The same method is used for multiple targets by searching for the two maximum values. The same attenuation image estimates are generated which show the varying range of attenuation values. Using the attenuation imagery, targets may be located through visual inspection. However, for this research, the number of targets must be known to determine how many maxima should be expected. Adaptive filter and machine vision techniques are explored in the literature [17, 18, 44, 45, 56] to estimate the number of targets and then accurately track them, but they were not implemented because they were not the focus of this research.

Motion Tracking and Spatial Pattern Monitoring. Data analysis for motion tracking and spatial pattern monitoring are similar in the fact that the targets are moving and therefore the data is not time averaged before processing. Therefore, the same steps used in analyzing stationary target localization data are implemented, except a maximum value is located in each frame and stored in a new matrix of $[L_x, L_y, \# \text{ of frames}]$ size. The new matrix can be used to generate a single, aerial 2-D attenuation image estimate that shows the maximum attenuation values over time and all others are set to zero. Each maximum value represents a target's position at that point in time. The values are stored sequentially so the path may be estimated as well.

An additional step that was not taken in the analysis of stationary localization data was applying some form of logic to throw out unreliable estimates. In stationary localization, it wasn't necessary because a time average was taken and therefore if a frame of measurements was unreliable, the effects of an inaccurate estimate were minimized. For motion tracking, the maximum value of each frame of data was analyzed; the maximum represents a position estimate for that point in time, if the value was less than 50% of the maximum attenuation value of the entire data set (each frame included), it was thrown out.

The last step in analyzing motion tracking and spatial pattern monitoring data was the process of generating a histogram storing the frequency of occupied pixels over time. Ultimately, the histogram will not only show the estimated positions and paths but also the frequency with which the respective pixel was occupied. The final histogram considered only those estimates that were considered to be reliable passing the logic test described above.

Error Calculations. Two forms of error calculation were used in the data analysis of this research. The first is the error in the position estimate, ϵ_D , which is calculated using the *Euclidean Distance* between each true position and corresponding estimated position:

$$\epsilon_D = \frac{1}{N_z \times N_T} \sum_{i=1}^{N_T} \sum_{ii=1}^{N_z} \|(\hat{x}, \hat{y}, \hat{z})_{i,ii} - (x, y, z)_{sT,i,ii}\|, \quad (3.2)$$

where $(x, y, z)_{sT}$ is the target's true stationary position, $(\hat{x}, \hat{y}, \hat{z})$ is the estimated position, N_z is the number of estimates in the z -dimension based on target height, and N_T is the number of targets. This form of error was used in analyzing the results from stationary localization experiments. To determine the error in a 3-D position estimate, the true position and estimated position from each $x - y$ plane were compared. For a 2-D position estimate, only one truth-estimate comparison was needed per target. In each case, the position estimate error is an average per $x - y$ estimate.

The second form, $NMSE_R$, is the error in the estimated pseudo attenuation images from the motion tracking and spatial pattern monitoring experiments. The truth image \mathbf{x}_{mT} is generated from a matrix of ones and zeros, and therefore the estimated image must also be normalized between zero and one. The pseudo attenuation image estimate, $\hat{\mathbf{x}}_{mC}$, is a time averaged estimate capturing the entire estimated path such that the pixels that were estimated to be occupied at some point in time were set to one and all others were set to zero. The NMSE of the normalized image is defined as:

$$NMSE_R = \frac{\|\hat{\mathbf{x}}_T - \mathbf{x}_{mC}\|^2}{N_p}, \quad (3.3)$$

where N_p is the number of pixels in the image and $\hat{\mathbf{x}}_T$ is the true image consisting of ones in pixels the known path traverses and zeros elsewhere. Error estimation for spatial pattern monitoring was accomplished as a means to verify primary position and path localization.

3.9 Chapter Summary

This chapter described the equipment and tools used in this research and presented the methodologies used to establish an RTI network, simulate truth data, design experiments, and analyze the data from those experiments.

IV. Results and Discussion

THIS chapter presents results of various stationary localization, motion tracking, and spatial pattern monitoring experiments for one and two targets both in unobstructed and obstructed networks. The effects on stationary target localization accuracy and attenuation image estimate resolution as a result of parameters, α and Δ_p , are discussed.

The 2-D and 3-D position and attenuation image estimation results are presented for comparison from a select number of stationary localization and motion tracking experiments; the research observations and conclusions drawn apply to each of the experiments conducted in that category as described in Tables 3.2 and 3.3. Additional comparisons are made between experiments where the target's position is varied, furniture obstructions are introduced, and a second target is present. Lastly, the results from each spatial pattern monitoring experiment are discussed. Focus is placed on the impacts of the specific path used, how often the path is traveled, and the presence of more than one target.

4.1 Stationary Target Localization

Stationary localization experiments were categorized by the number of targets, the true position, and the presence of additional obstructions in the area. The results of varying Δ_p and α for each experiment were analyzed. The average localization error, $\bar{\epsilon}_D$, of 2-D and 3-D position estimates across the range of $\alpha = [1 : 150]$ for each experiment category are presented in Table 4.1.

In all but two cases, the 2-D position estimates were 100% accurate when $\Delta_p = 1.0$ ft regardless of the value of α . The average localization error when $\Delta_p = 0.5$ ft was insignificant for single target estimates and still modest, less than 2.0 ft, for experiments with two targets. 3-D position estimates generally suffered larger average localization error in each category across the range of α and for both values of Δ_p . Conversely, the average

localization error for 3-D position estimates was larger when $\Delta_p = 1.0$ ft. In both cases of Δ_p , 3-D position estimates experienced the largest values of ϵ_D across the board. As is shown in later figures in this section, high α values can have a negative impact when two targets are within close proximity of each other. The smoothing effects can overtake the estimate and result in “blending” the two high attenuation spatial impact areas together, making it difficult to differentiate between multiple targets. When additional obstructions are introduced into the area multipath may increase and link RSS may be absorbed by the new obstructions, increasing the challenge of locating multiple targets. For single target 3-D position estimation, the larger values of error are relative. This will be further illustrated in Figure 4.6 and discussed in that particular section.

Table 4.1: Average localization error, $\bar{\epsilon}_{D,\alpha}$ (ft) per experiment, across the range $\alpha = [1 : 150]$ for 2-D and 3-D position estimates of stationary targets.

Experiment Details			2-D		3-D	
<i>Number of Targets</i>	$(x, y)_{sT}$	<i>Obstructions</i>	$\Delta_p = 0.5$ ft	$\Delta_p = 1.0$ ft	$\Delta_p = 0.5$ ft	$\Delta_p = 1.0$ ft
1	(3,6)	No	1.20	0.32	1.17	1.31
1	(3,6)	Yes	0.28	0.00	0.69	1.22
1	(7,5)	No	0.34	0.00	1.20	1.47
1	(7,5)	Yes	0.06	0.00	0.59	1.15
1	(7,6)	Yes	0.18	0.00	0.95	1.27
2	(5,2) (7,6)	No	1.87	0.00	3.29	3.34
2	(5,2) (7,6)	Yes	1.96	0.55	2.82	3.35

Furthermore, the average localization error between similar experiments, where the only difference was the presence of additional obstructions tended to either be lower or unaffected when obstructions, were present. The presence of additional obstructions had little impact, if any at all, on stationary localization. This data provided insight into the performance of RTI in a naturally obstructed environment.

The addition of a second target resulted in larger average localization error for 2-D position estimates when $\Delta_p = 0.5$ ft and 3-D position estimates for both voxel sizes as compared to single target estimates. The addition of a second target generally resulted in noisier measurements making localization more challenging. Additional results from two-target localization experiments are discussed later on.

In this research, target tracking depended on the 2-D position estimate; therefore, Δ_p will remain at 1.0 ft for motion tracking and spatial pattern monitoring experiments since it yielded the most favorable results.

The parameter α determines how much influence the regularization term has on the estimate dictating the amount of original measurement information present in the final estimate. The variance of the average localization error, $\sigma_{\bar{\epsilon}_D}^2$, as a function of α and Δ_p for each experiment category is presented in Table 4.2. In each experiment category, there was little variance in the average localization error over the range of α for each experiment category. Values of $5 \geq \alpha \geq 150$ yielded the same results for 2-D position estimates of stationary targets. That same range of α resulted in only slight variations for 3-D position estimates of stationary targets. Overall, there was less variance in the average localization error as a result of α for 3-D position estimates versus 2-D position estimates. Small variances illustrate the consistency of both 2-D and 3-D stationary target localization regardless of α .

Table 4.2: Variance of average localization error, $\sigma_{\epsilon_p}^2$ (ft²) for 2-D and 3-D position estimates of stationary targets across the range $\alpha = [1 : 150]$.

Experiment Details			2-D		3-D	
<i>Number of Targets</i>	$(x, y)_{sT}$	<i>Obstructions</i>	$\Delta_p = 0.5$ ft	$\Delta_p = 1.0$ ft	$\Delta_p = 0.5$ ft	$\Delta_p = 1.0$ ft
1	(3,6)	No	0.04	0.03	0.03	0.08
1	(3,6)	Yes	0.06	0.00	0.02	0.02
1	(7,5)	No	0.03	0.00	0.04	0.03
1	(7,5)	Yes	0.06	0.00	0.02	0.04
1	(7,6)	Yes	0.06	0.00	0.01	0.01
2	(5,2) (7,6)	No	0.01	0.00	0.01	0.05
2	(5,2) (7,6)	Yes	0.10	0.70	0.03	0.12

The choice for α had visually apparent impacts on estimated attenuation images versus position estimates. For smaller values of α the impact was more evident, but as α was increased, the impact on a set of results between subsequent values of α grew to be less noticeable to the human eye. This is not true for extremely large values of α shown in Figures 4.14 and 4.16. As α is increased, the image visually appears to tighten around the obstruction as the high attenuation intensities caused by the obstruction stand out more and the intensity of noisy areas within the image is reduced. The overall intensity of the image is reduced across each pixel. As α is increased, the attenuation image will become smoother and the higher attenuation intensities caused by the obstruction will begin to blur over the entire image.

Figures 4.1 and 4.2 present the 2-D aerial attenuation images $\hat{\mathbf{x}}_{(3,6)}$ (dB/ft) of a target that is 5'8" tall standing at position $(x, y)_{sT} = (3, 6)$ ft as marked with the asterisk. The figures provide comparisons for each value of Δ_p as the value of α is increased from 1.0 to 125.0. Note how noisy areas are reduced and the image appears smoother, and stronger attenuation intensities appear concentrated around the target for both pixel sizes. Ultimately, the grouping of higher intensities where the target is standing disperses or

spreads over a greater area revealing a smoother image, especially when $\Delta_p = 0.5$ ft. This smoothing effect is the intended result Tikhonov Regularization, to help fill-in and smooth sparse and highly varied data. Values of α larger than those investigated in this research would be expected to have even greater smoothing effects until the spatial impact area of the target is blurred across the entire image.

Image estimates generated with $\Delta_p = 0.5$ ft versus $\Delta_p = 1.0$ ft appear to provide additional image resolution and thus are more aesthetically pleasing. However, image resolution does not necessarily correspond with localization accuracy as the position estimate is based on the maximum registered attenuation value. One such example is provided in Figure 4.3. The localization results for this experiment yielded in an inaccurate 2-D position estimate when $\Delta_p = 0.5$ ft, but an accurate estimate for the larger pixel size regardless of the value of α . The physical size of a pixel as it relates to the average size of a human target is an important relationship, the larger pixel size provides more tolerance in physical position estimation. If Δ_p were set to be much larger than the expected target size the estimates may no longer be useful because the possible occupied area identified in the estimate would be too large.

Choosing an appropriate pixel size should not only depend on the fidelity needed, but on the achievable node density and available link coverage. The number of unique two-way links should be equal to or greater than the number of pixels or voxels (i.e., $M \geq N$). When the number of pixels or voxel is greater than the number of links in the network, the same amount of RSS information from M links is expected to be discretized over a finer area than was actually measured.

The impacts of α and Δ_p are consistent in 3-D position estimation, and 2-D lateral and 3-D attenuation image estimation. The corresponding 2-D lateral attenuation images from the same experiment presented in Figures 4.1 and 4.2 are shown in Figures 4.4 and 4.5. There is a decrease in the registered attenuation intensity of the target as α is increased.

The negative impact in position estimation between two images with the same value of α as Δ_p is varied is less apparent in lateral images. However, from these images we transition to 3-D position and attenuation image estimation, and the possibility of extracting target features such as height, size, and density.

Figure 4.6 shows the 3-D position estimates for a stationary target that is 5'1" tall standing at $(x, y)_{sT} = (3, 6)$ ft. 2-D localization error ϵ_D appears to stabilize for $\Delta_p = 1.0$ ft at lower values of α , while for $\Delta_p = 0.5$ increased regularization is needed. In 3-D position estimation ϵ_D doesn't stabilize until regularization is increased to approximately $\alpha = 75$ for both voxel sizes. Figure 4.6 further illustrates that image resolution does not necessarily coincide with localization accuracy. Even though ϵ_D is larger for $\Delta_p = 1.0$ ft than $\Delta_p = 0.5$ ft, a larger voxel size yielded four of the five accurately estimated occupied voxels while for each value of α presented, none of the occupied voxels were correctly estimated when $\Delta_p = 0.5$ ft. For the smaller voxel size some experimental results did yield accurately estimated voxels; however, the majority of results were in favor of a larger voxel size for both 2-D and 3-D position estimates. Examples are shown in Figure 4.12.

Figures 4.7 and 4.8 are 3-D attenuation images for a stationary target that is 5'1" tall standing at $(x, y)_{sT} = (3, 6)$. Voxels with a registered attenuation value greater than 50% of $\hat{\mathbf{x}}_{p,MAX}$ are enlarged so they are more visible. The grouping of higher attenuation values cluster near the target's true position. Higher values of α smooth the estimate, and the smaller voxel size provides a higher resolution image. This is more aesthetically appealing, and results in a denser estimate of the target's volume within the space.

Three targets with different heights were used to determine if a 3-D RTI network could be used to extract physical features of a target such as height, size, and density. Multiple data sets were recorded for each target; the target's position remained constant at $(x, y)_{sT} = (3, 6)$ ft. Figures 4.9, 4.10, and 4.11 provide comparisons of 2-D and 3-D attenuation images from multiple experiments where target position, α , and Δ_p remained

constant but the target's height was different in each set. Examining the 2-D lateral attenuation images, the target's height is somewhat discernible, but it varies between experiments. In every case, the strongest attenuation values were registered in the lowest layer of voxels. Figure 4.11 provides the aerial views from the same set of experiments. In the 2-D attenuation images, there appears to be a relationship in the scale and shape of the attenuation caused by the target and the target's features, such as height in the aerial view, and width or density in the lateral view. A consistent relationship between target features and the resulting 3-D attenuation image for each experiment is not evident.

As stated earlier, a higher resolution would be more useful for higher fidelity in feature extraction. The smoothing effects of higher α values may also prove more beneficial or even necessary for feature extraction in addition to using smaller pixel sizes. Examples of the effects of significantly increasing α for the same experiments used previously are provided in Figures 4.13, 4.14, 4.15, and 4.16. The intense smoothing effects of $\alpha = [500.0, 1000.0]$ on the 3-D attenuation image requires that only the voxels with registered attenuation values within 30% of $\hat{\mathbf{x}}_{p,MAX}$ be enlarged.

Figure 4.17 includes aerial and lateral 2-D attenuation images for a localization experiment of two, stationary targets while the value of α is varied. When a second target is present a number of links will be attenuated before intersecting the second target, which will be more detrimental in networks with limited link coverage. Additionally, the introduction of a second target in the network results in more multipath and noise. In these images, mid-range values of α are effective in reducing the noise so it is easier to accurately locate both targets without blurring the two spatial impact areas together.

Through visual inspection, the value of $\alpha = 75.0$ appeared to result in attenuation images where targets were clearly identifiable between each experiment category. It was also one of the first values of α where the average localization error stabilized between 2-D

and 3-D estimates. The regularization parameter $\alpha = 75.0$ was selected for presenting the results of the motion tracking and spatial pattern monitoring experiments.

Estimation accuracy is also dependent on the target's physical location within the network. Ultimately it is dependent on the link coverage and the multipath due to the area's topography specific to the respective target's location. Figure 4.18 provides a comparison of the estimates from two experiments where a stationary target stood at two different locations within the network. The average localization error when the target stood at $(x, y)_{sT} = (7, 5)$ ft was lower for 2-D and 3-D position estimates when compared to experiments where the target stood at $(x, y)_{sT} = (3, 6)$ ft. Over the set of experiments for each position, the 2-D aerial attenuation images for $\hat{\mathbf{x}}_{(7,5)}$ (dB/ft) appeared to be less noisy than those for $\hat{\mathbf{x}}_{(3,6)}$ (dB/ft); the opposite was true for the lateral view of the attenuation images.

In Figures 4.19 and 4.20, the same two points used in the previous set of experiments are re-examined when additional obstructions are introduced into the area. Adding furniture to the environment had little affect on the 2-D and 3-D position estimates. It does appear that additional noise was visible in the attenuation images, specifically in the lateral views. It also seems that impact of additional obstructions was greater in the estimated attenuation images when the target stood at $(x, y)_{sT} = (7, 5)$ as opposed to $(x, y)_{sT} = (3, 6)$ ft.

Figure 4.21 illustrates the impact of additional obstructions in an experiment with two targets. The lateral attenuation images appear to be most affected by the multipath introduced as a result of the new obstructions. The second target is not discernible when there is furniture in the way; however, the impact isn't noticeable in the aerial estimates.

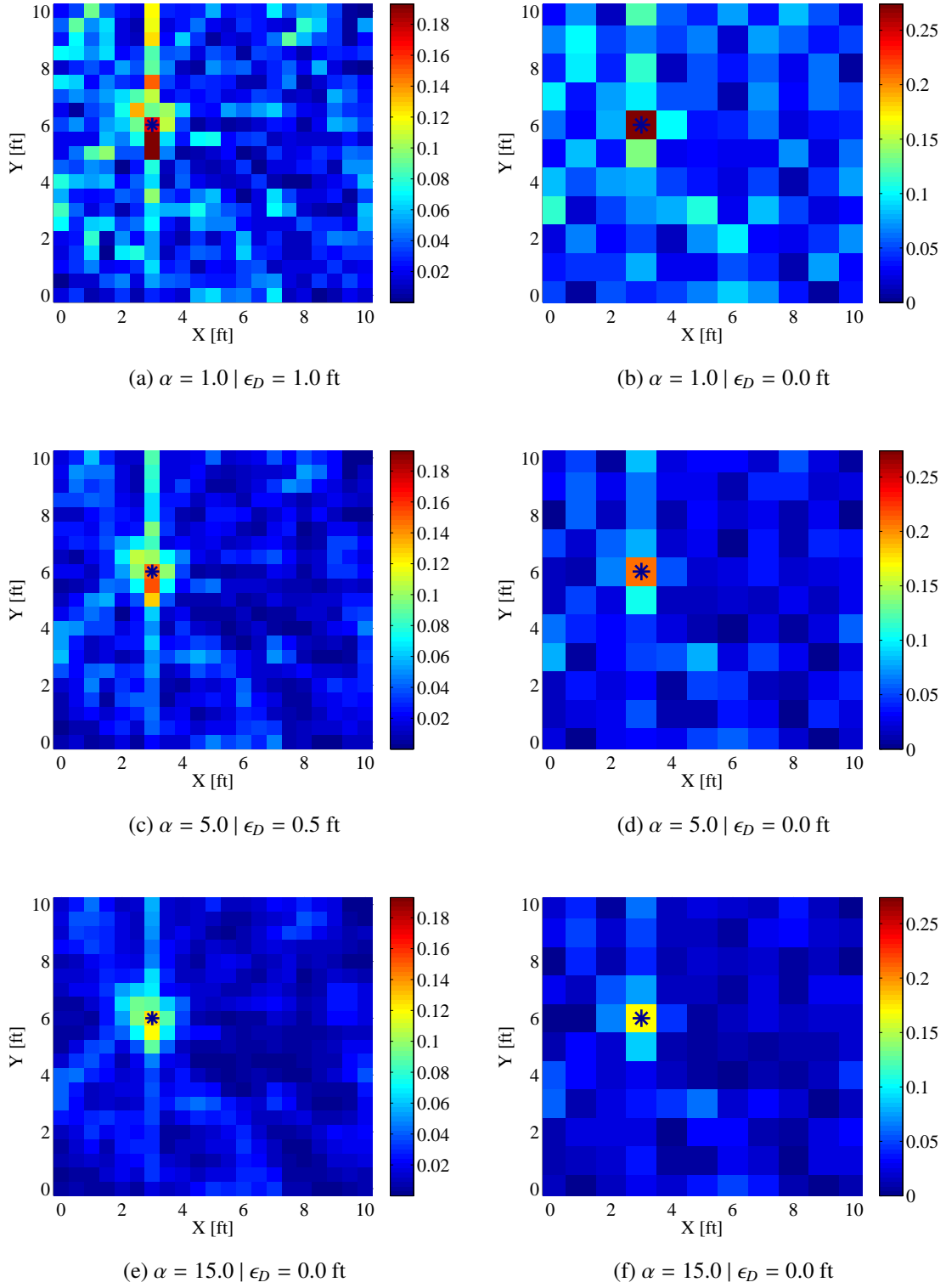
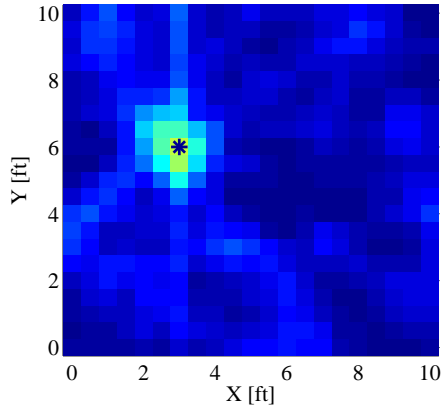
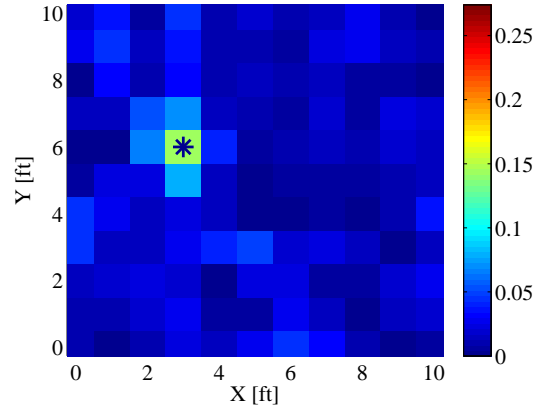


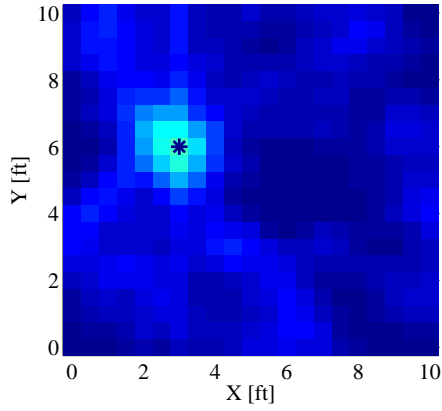
Figure 4.1: Relationship between pixel size and 2-D position and aerial attenuation images, $\hat{\mathbf{x}}_{(3,6)}$ (dB/ft). Stationary 5'8" tall target standing at $(x, y)_{sT} = (3, 6)$ ft. In the first column $\Delta_p = 0.5$ ft and in the second column $\Delta_p = 1.0$ ft. $\{\alpha = [1.0, 5.0, 15.0]\}$



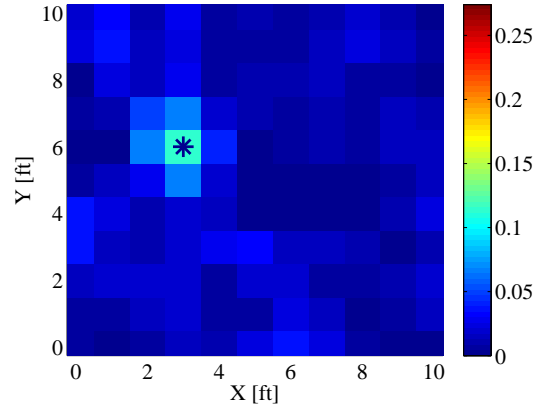
(a) $\alpha = 30.0 \mid \epsilon_D = 0.0 \text{ ft}$



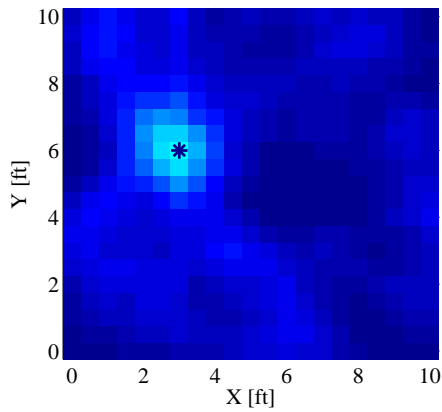
(b) $\alpha = 30.0 \mid \epsilon_D = 0.0 \text{ ft}$



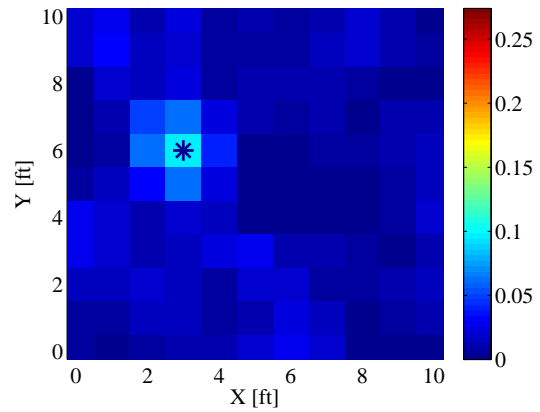
(c) $\alpha = 75.0 \mid \epsilon_D = 0.0 \text{ ft}$



(d) $\alpha = 75.0 \mid \epsilon_D = 0.0 \text{ ft}$

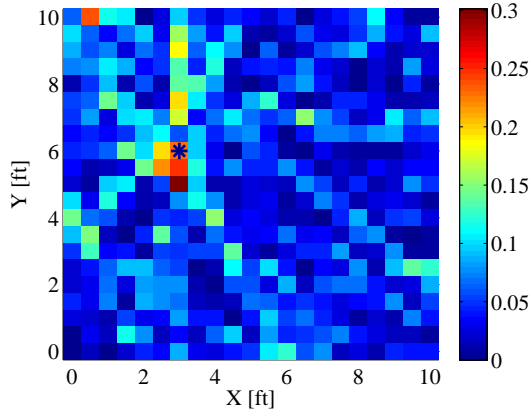


(e) $\alpha = 125.0 \mid \epsilon_D = 0.0 \text{ ft}$

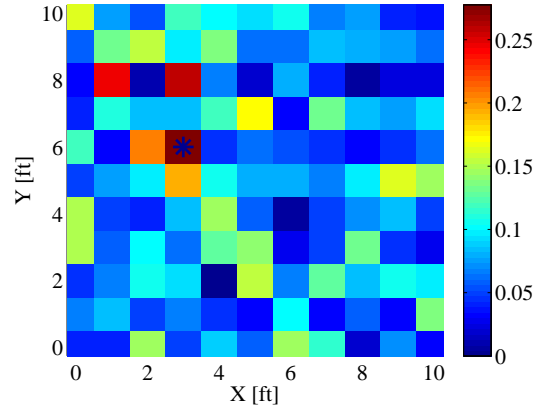


(f) $\alpha = 125.0 \mid \epsilon_D = 0.0 \text{ ft}$

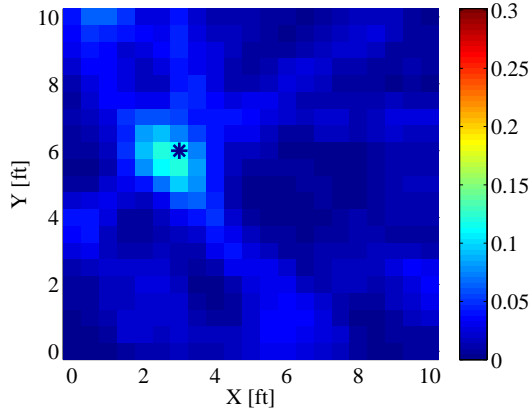
Figure 4.2: Relationship between pixel size and 2-D position and aerial attenuation images, $\hat{\mathbf{x}}_{(3,6)}$ (dB/ft). Stationary 5'8" tall target standing at $(x, y)_{sT} = (3, 6)$ ft. In the first column $\Delta_p = 0.5\text{ft}$ and in the second column $\Delta_p = 1.0\text{ft}$. $\{\alpha = [30.0, 75, 125.0]\}$



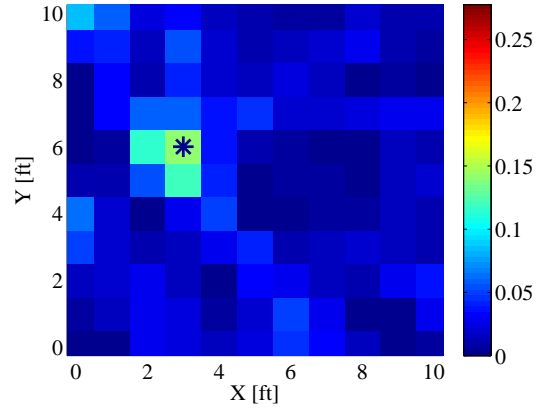
(a) $\alpha = 1.0 \mid \epsilon_D = 1.0 \text{ ft}$



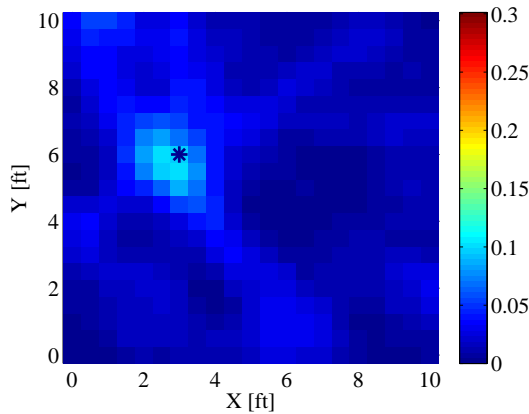
(b) $\alpha = 1.0 \mid \epsilon_D = 0.0 \text{ ft}$



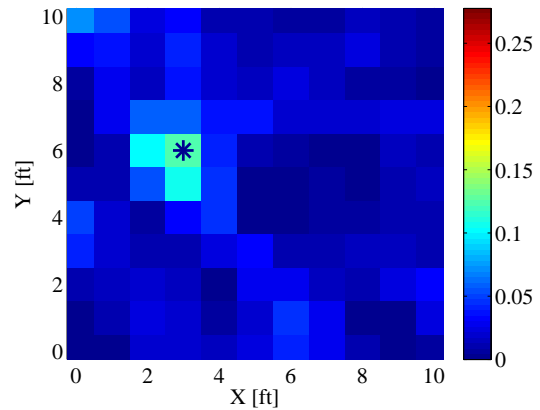
(c) $\alpha = 75.0 \mid \epsilon_D = 0.5 \text{ ft}$



(d) $\alpha = 75.0 \mid \epsilon_D = 0.0 \text{ ft}$



(e) $\alpha = 125.0 \mid \epsilon_D = 0.5 \text{ ft}$



(f) $\alpha = 125.0 \mid \epsilon_D = 0.0 \text{ ft}$

Figure 4.3: Relationship between pixel size and 2-D position and aerial attenuation images, $\hat{\mathbf{x}}_{(3,6)}$ (dB/ft). Stationary 6'1" tall target standing at $(x, y)_{sT} = (3, 6)$ ft. In the first column $\Delta_p = 0.5\text{ft}$ and in the second column $\Delta_p = 1.0\text{ft}$. $\{\alpha = [1.0, 75.0, 125.0]\}$

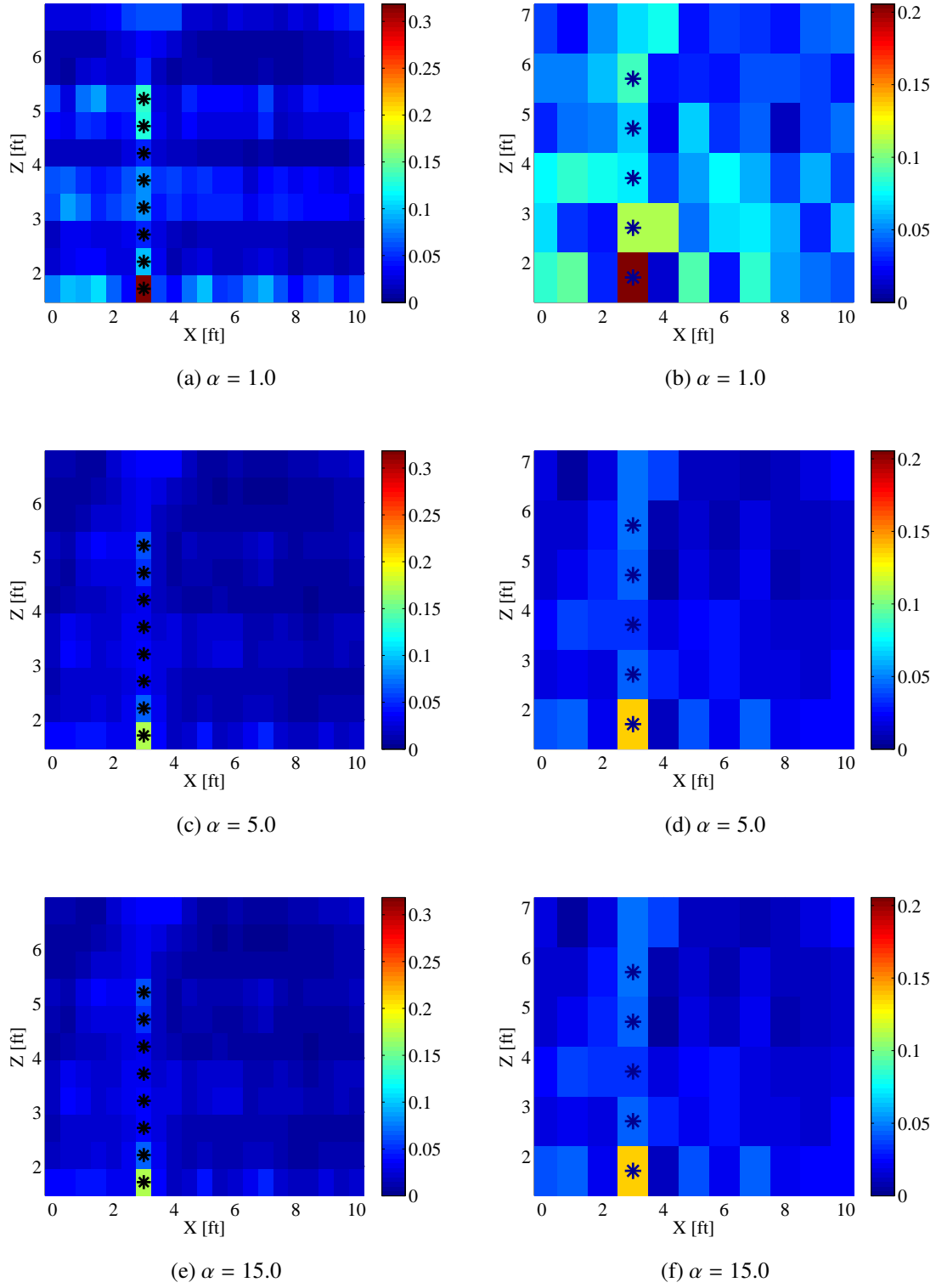


Figure 4.4: Relationship between pixel size and 2-D lateral attenuation images, $\hat{\mathbf{x}}_{(3,6)}$ (dB/ft). Stationary 5'8" tall target standing at $(x, y)_{sT} = (3, 6)$ ft. In the first column $\Delta_p = 0.5\text{ft}$ and in the second column $\Delta_p = 1.0\text{ft}$. $\{\alpha = [1.0, 5.0, 15.0]\}$

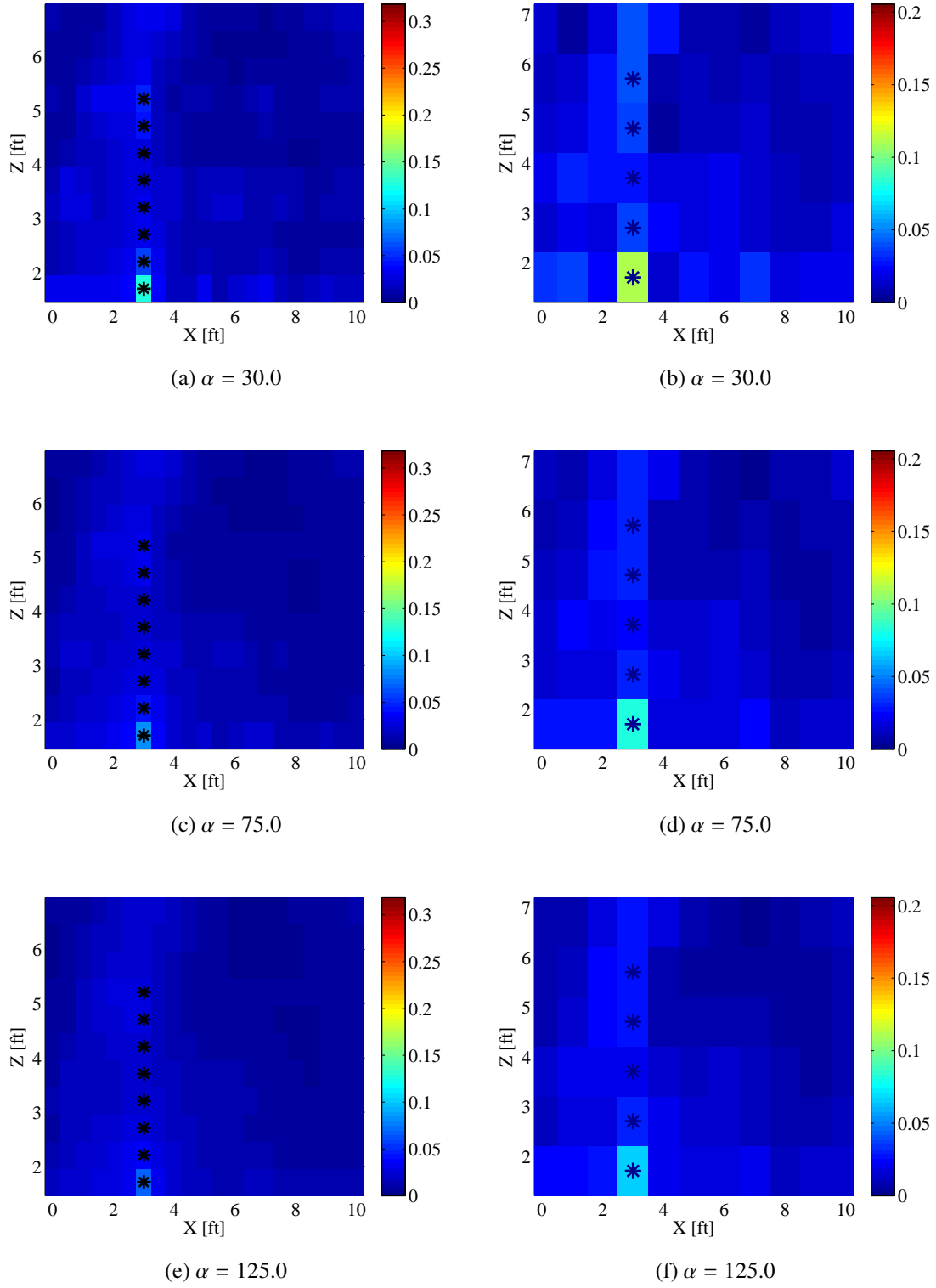
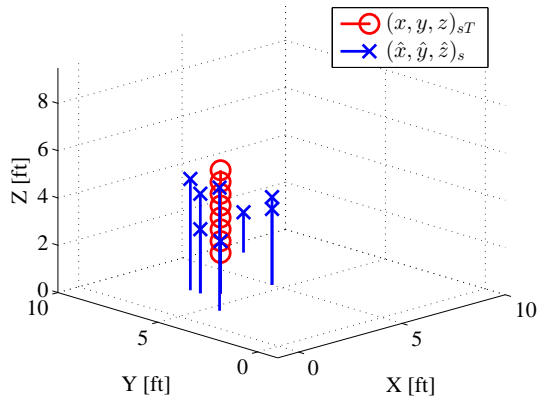
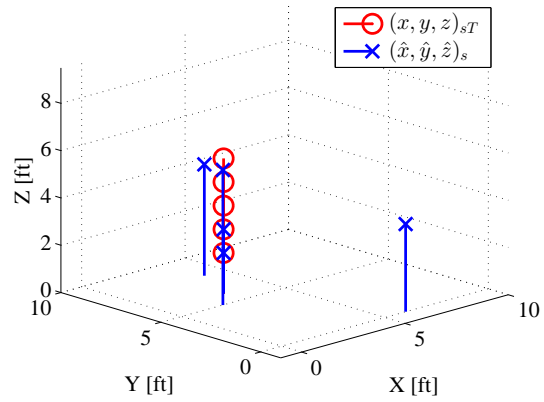


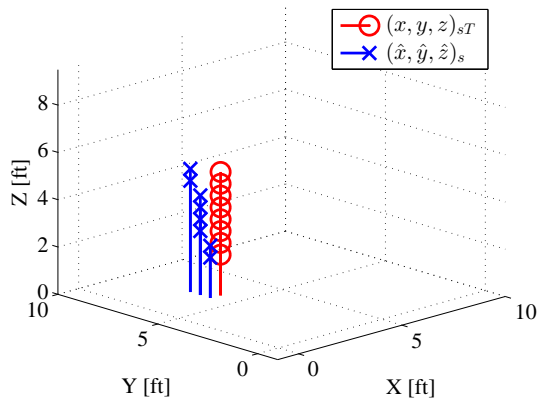
Figure 4.5: Relationship between pixel size and 2-D lateral attenuation images, $\hat{\mathbf{x}}_{(3,6)}$ (dB/ft). Stationary 5'8" tall target standing at $(x,y)_{sT} = (3,6)$ ft. In the first column $\Delta_p = 0.5$ ft and in the second column $\Delta_p = 1.0$ ft. $\{\alpha = [30.0, 75, 125.0]\}$



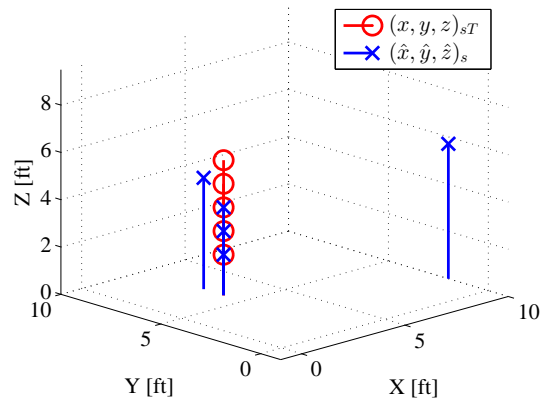
(a) $\alpha = 1.0 \mid \epsilon_D = 1.72 \text{ ft}$



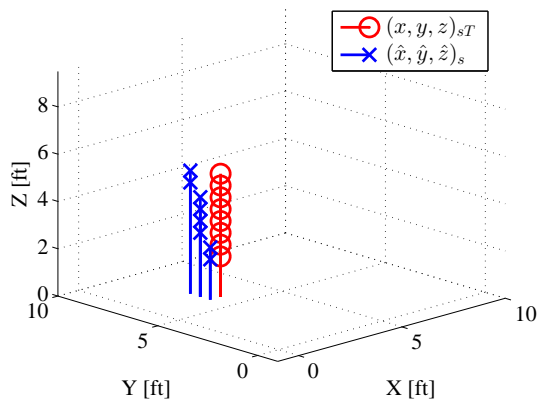
(b) $\alpha = 1.0 \mid \epsilon_D = 2.07 \text{ ft}$



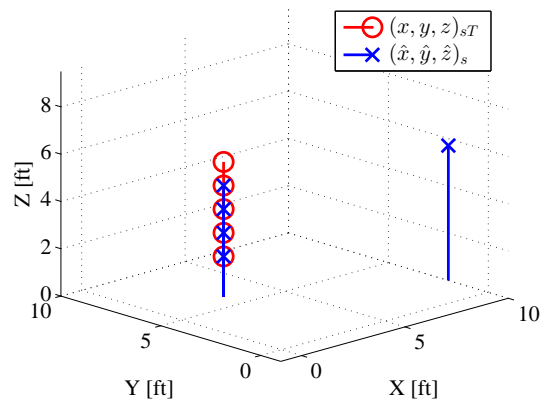
(c) $\alpha = 50.0 \mid \epsilon_D = 0.76 \text{ ft}$



(d) $\alpha = 50.0 \mid \epsilon_D = 1.81 \text{ ft}$

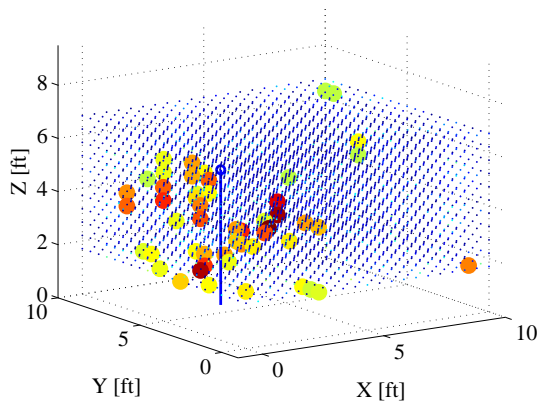


(e) $\alpha = 75.0 \mid \epsilon_D = 0.76 \text{ ft}$

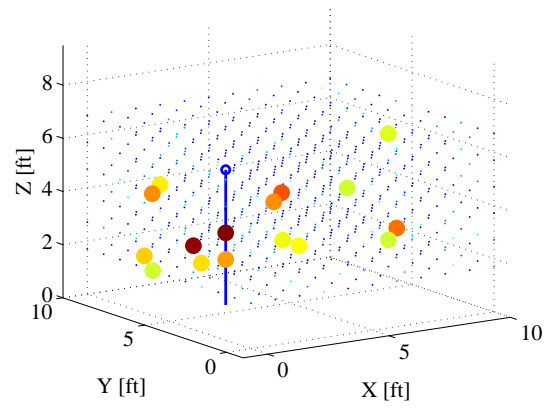


(f) $\alpha = 75.0 \mid \epsilon_D = 1.61 \text{ ft}$

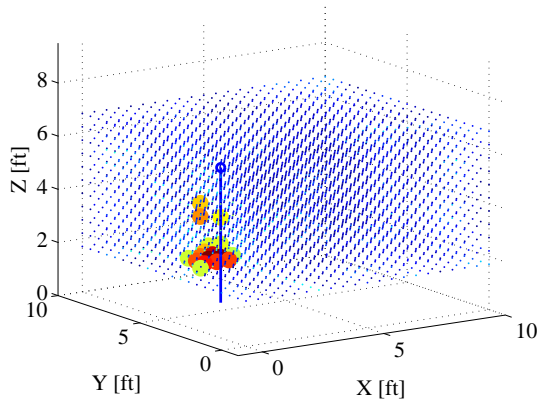
Figure 4.6: Relationship between pixel size and 3-D position estimates, $(\hat{x}, \hat{y}, \hat{z})$ ft. Stationary 5'1" tall target standing at $(x, y)_{sT} = (3, 6)$ ft. In the first column $\Delta_p = 0.5\text{ft}$ and in the second column $\Delta_p = 1.0\text{ft}$. $\{\alpha = [1.0, 50.0, 75.0]\}$



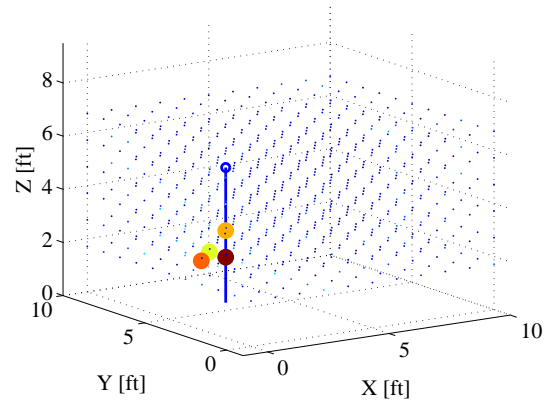
(a) $\alpha = 1.0 \mid \Delta_p = 0.5 \text{ ft}$



(b) $\alpha = 1.0 \mid \Delta_p = 1.0 \text{ ft}$

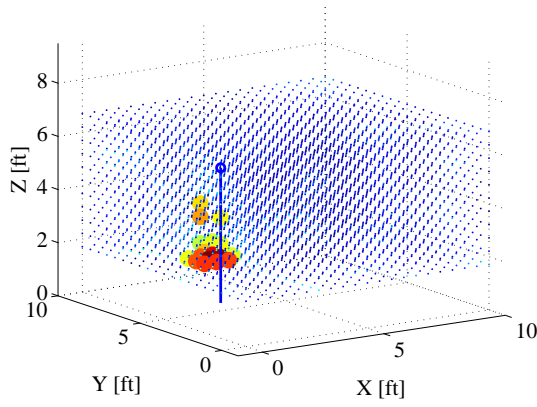


(c) $\alpha = 50.0 \mid \Delta_p = 0.5 \text{ ft}$

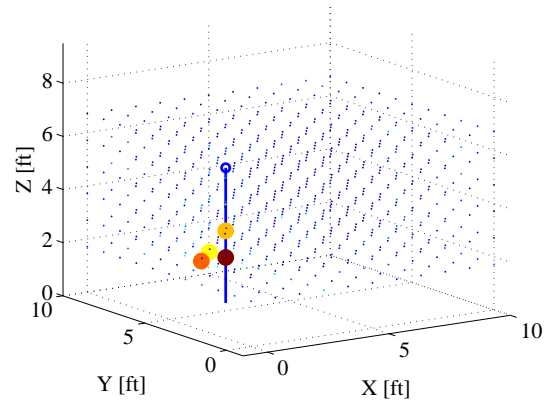


(d) $\alpha = 50.0 \mid \Delta_p = 1.0 \text{ ft}$

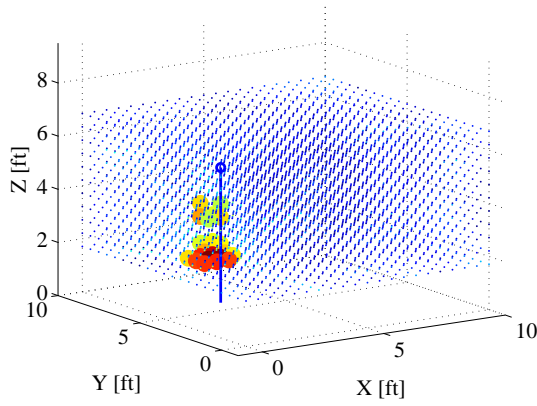
Figure 4.7: Relationship between pixel size and 3-D attenuation images, $\hat{\mathbf{x}}_{(3,6)}$ (dB/ft). Stationary 5'1" tall target standing at $(x, y)_{sT} = (3, 6)$ ft. In the first column $\Delta_p = 0.5$ ft and in the second column $\Delta_p = 1.0$ ft. $\{\alpha = [1.0, 50.0]\}$



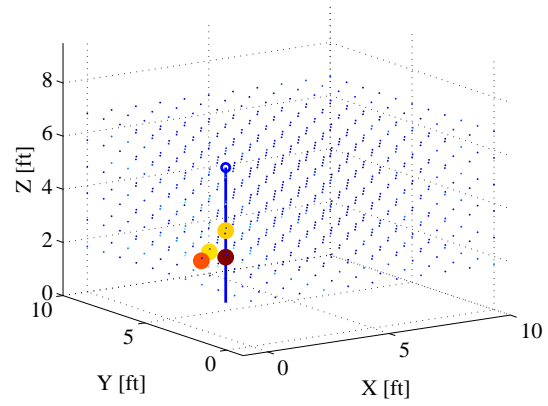
(a) $\alpha = 75.0 \mid \Delta_p = 0.5 \text{ ft}$



(b) $\alpha = 75.0 \mid \Delta_p = 1.0 \text{ ft}$

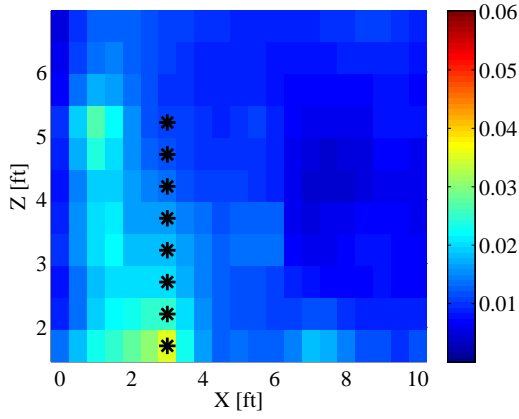


(c) $\alpha = 125.0 \mid \Delta_p = 0.5 \text{ ft}$

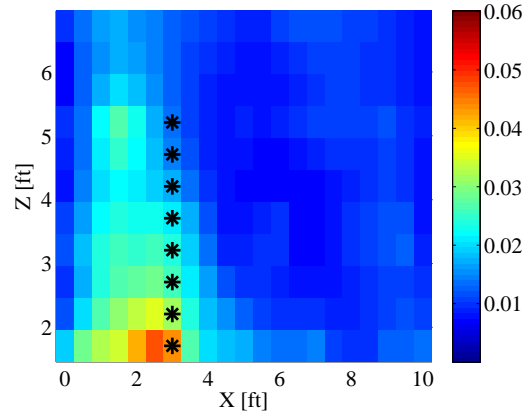


(d) $\alpha = 125.0 \mid \Delta_p = 1.0 \text{ ft}$

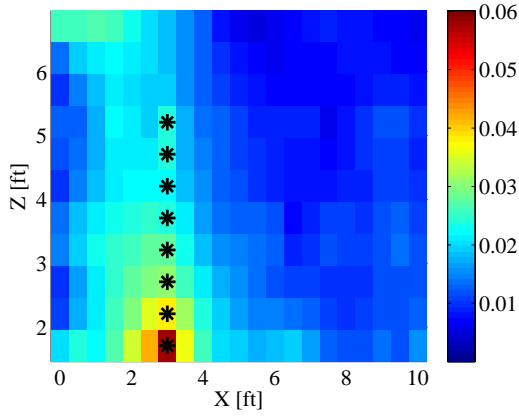
Figure 4.8: Relationship between pixel size and 3-D attenuation images, $\hat{\mathbf{x}}_{(3,6)}$ (dB/ft). Stationary 5'1" tall target standing at $(x, y)_{sT} = (3, 6)$ ft. In the first column $\Delta_p = 0.5$ ft and in the second column $\Delta_p = 1.0$ ft. $\{\alpha = [75, 125.0]\}$



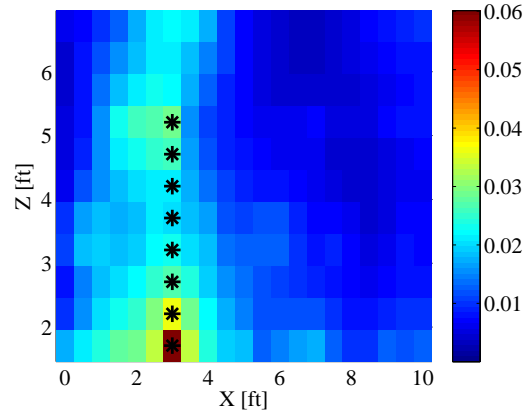
(a) Exp. 1 - Height: 5'1" | Weight: 130 lbs



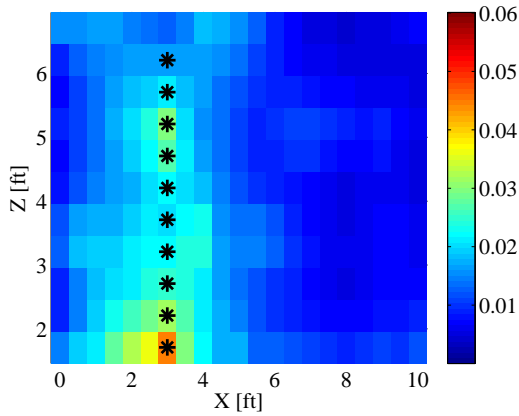
(b) Exp. 2 - Height: 5'1" | Weight: 130 lbs



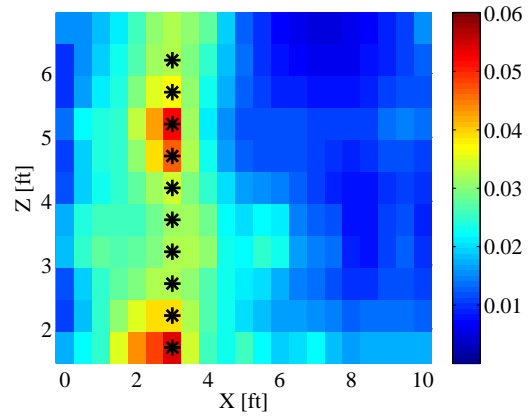
(c) Exp. 1 - Height: 5'8" | Weight: 190 lbs



(d) Exp. 2 - Height: 5'8" | Weight: 190 lbs

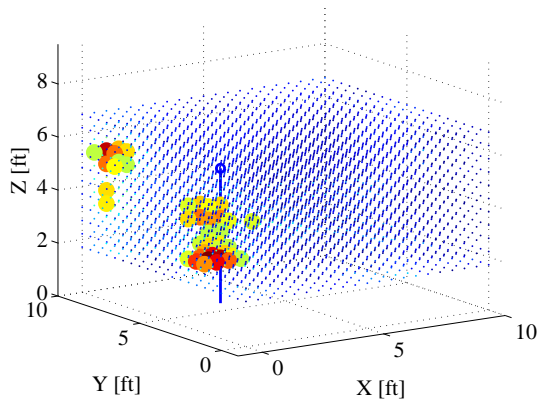


(e) Exp. 1 - Height: 6'1" | Weight: 185 lbs

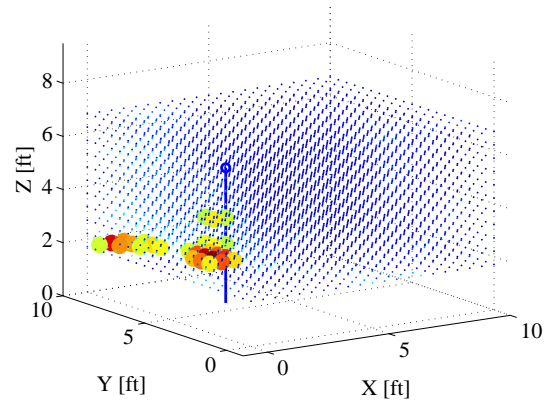


(f) Exp. 2 - Height: 6'1" | Weight: 185 lbs

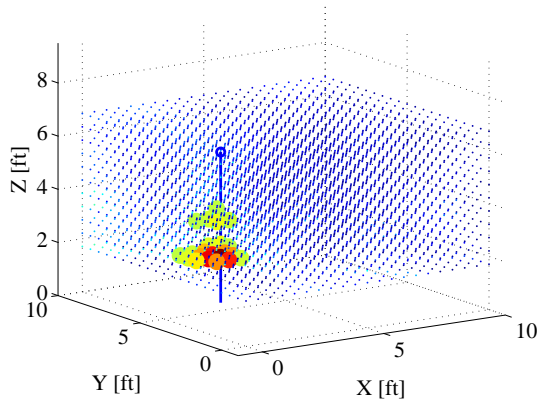
Figure 4.9: Comparison of 2-D lateral attenuation images, $\hat{\mathbf{x}}_{(3,6)}$ (dB/ft) of targets with different heights. Stationary target standing at $(x, y)_{sT} = (3, 6)$ ft. $\{\Delta_p = 0.5 \text{ ft} \mid \alpha = 150\}$



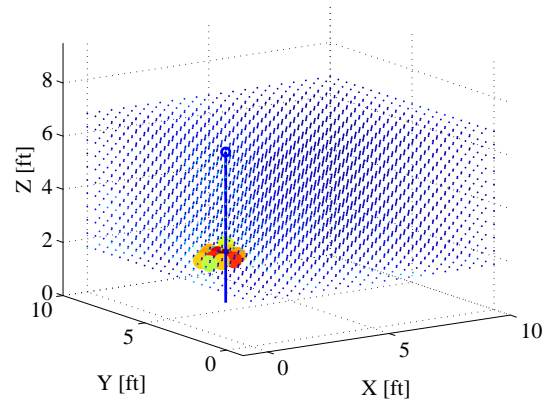
(a) Exp. 1 Target Height: 5'1"



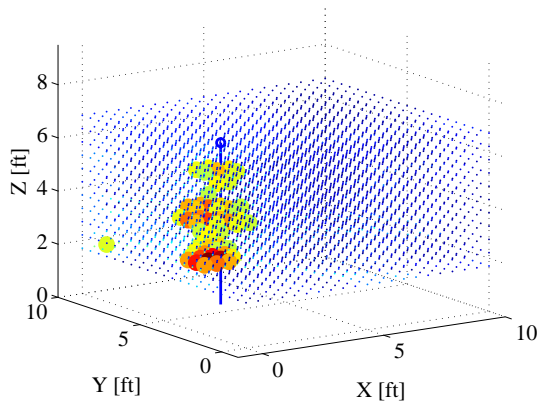
(b) Exp. 2 Target Height: 5'1"



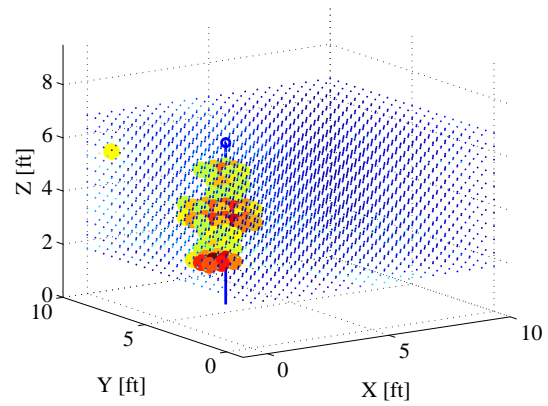
(c) Exp. 1 Target Height: 5'8"



(d) Exp. 2 Target Height: 5'8"

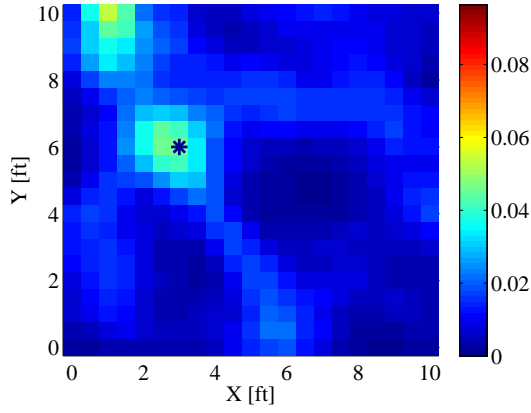


(e) Exp. 1 Target Height: 6'1"

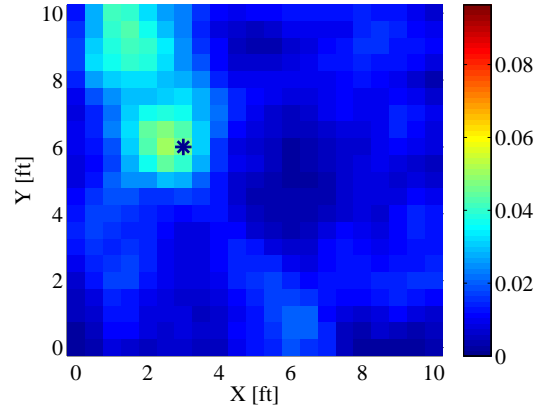


(f) Exp. 2 Target Height: 6'1"

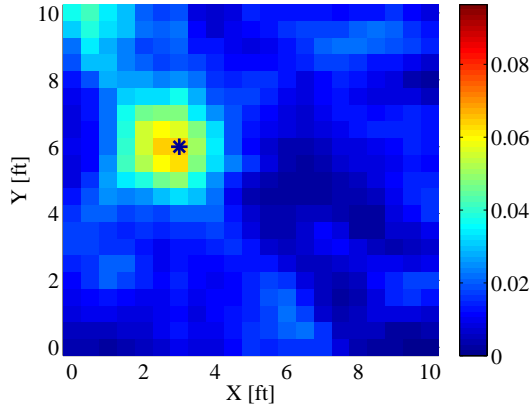
Figure 4.10: Comparison of 3-D attenuation images, $\hat{\mathbf{x}}_{(3,6)}$ (dB/ft) of targets with different heights. Stationary target standing at $(x, y)_{sT} = (3, 6)$ ft. $\{\alpha = 150 \mid \Delta_p = 0.5 \text{ ft}\}$



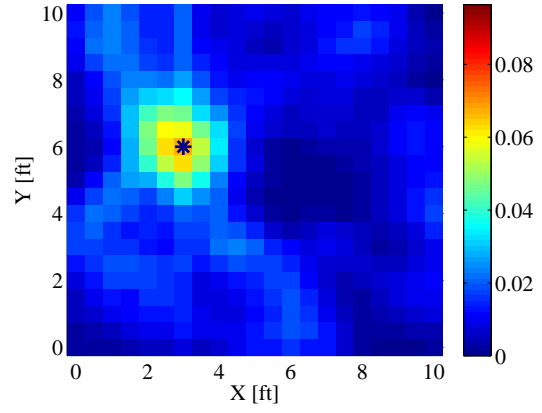
(a) Exp. 1 - Height: 5'1"



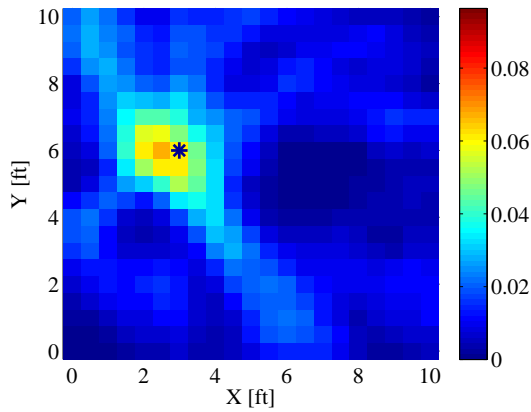
(b) Exp. 2 - Height: 5'1"



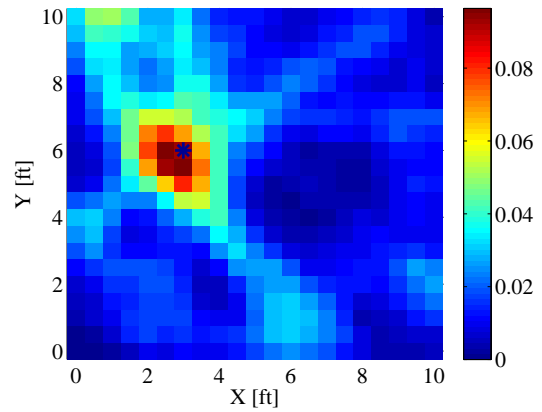
(c) Exp. 1 - Height: 5'8"



(d) Exp. 2 - Height: 5'8"

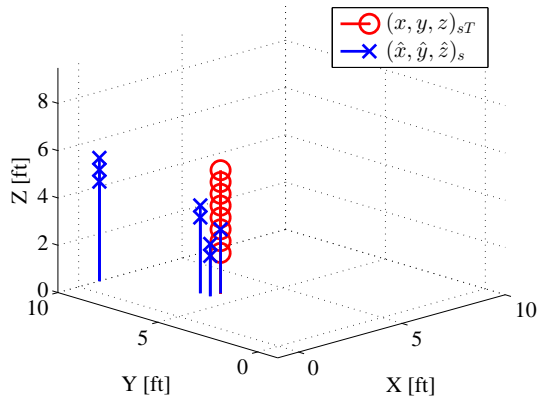


(e) Exp. 1 - Height: 6'1"

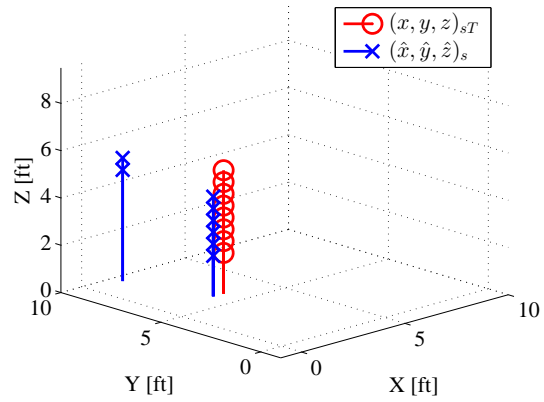


(f) Exp. 2 - Height: 6'1"

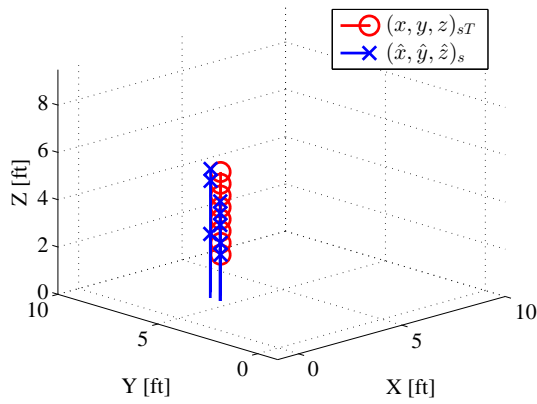
Figure 4.11: Comparison of 2-D aerial attenuation images, $\hat{\mathbf{x}}_{(3,6)}$ (dB/ft) of targets with different heights. Stationary target standing at $(x, y)_{sT} = (3, 6)$ ft. $\{\alpha = 150 \mid \Delta_p = 0.5 \text{ ft}\}$



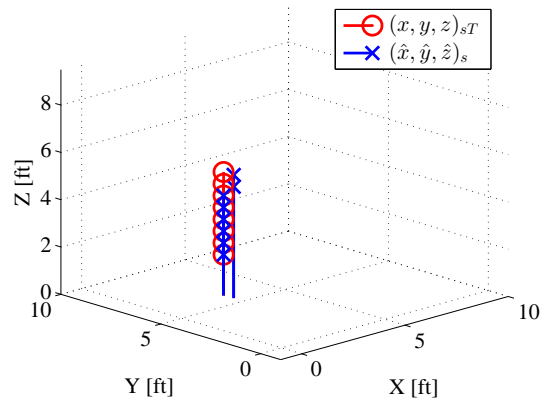
(a) Exp. 1 - Height: 5'1" | $\epsilon_D = 1.98$ ft



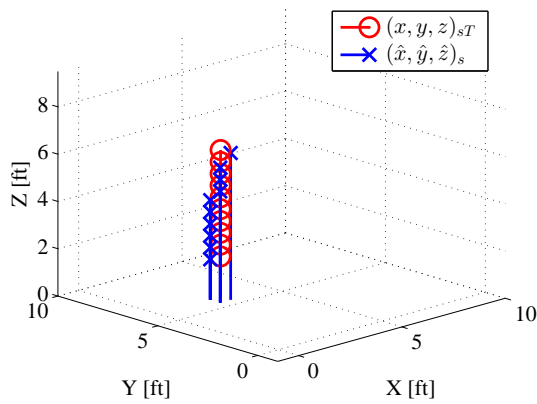
(b) Exp. 2 - Height: 5'1" | $\epsilon_D = 1.33$ ft



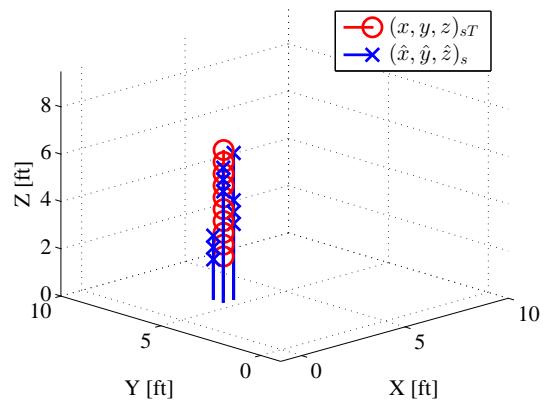
(c) Exp. 1 - Height: 5'8" | $\epsilon_D = 0.45$ ft



(d) Exp. 2 - Height: 5'8" | $\epsilon_D = 0.04$ ft

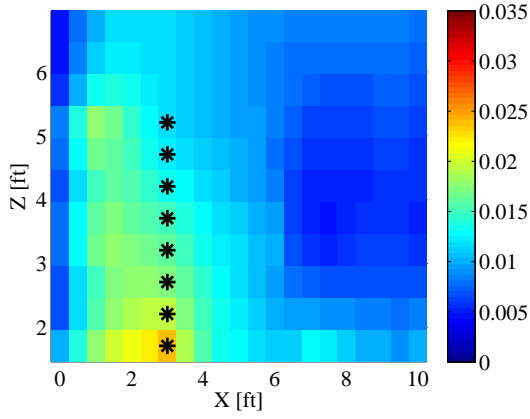


(e) Exp. 1 - Height: 6'1" | $\epsilon_D = 0.56$ ft

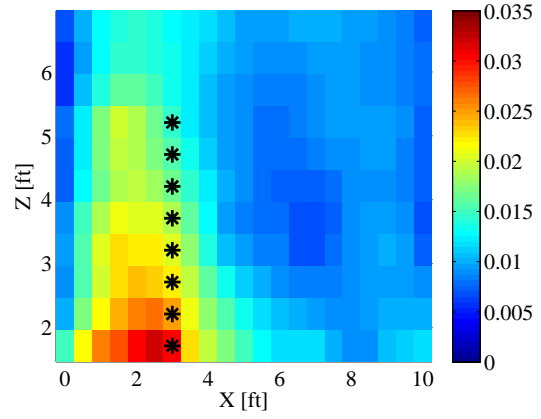


(f) Exp. 2 - Height: 6'1" | $\epsilon_D = 0.56$ ft

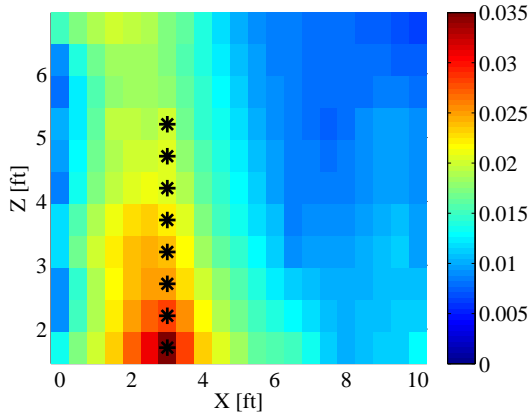
Figure 4.12: Comparison of 3-D position estimates, $(\hat{x}, \hat{y}, \hat{z})_{sT}$ (dB/ft) of targets with different heights. Stationary target standing at $(x, y)_{sT} = (3, 6)$ ft. $\{\alpha = 150 \mid \Delta_p = 0.5 \text{ ft}\}$



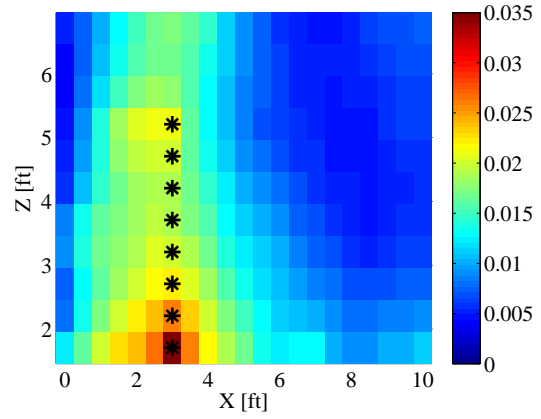
(a) Exp. 1 - Height: 5'1" | Weight: 130 lbs



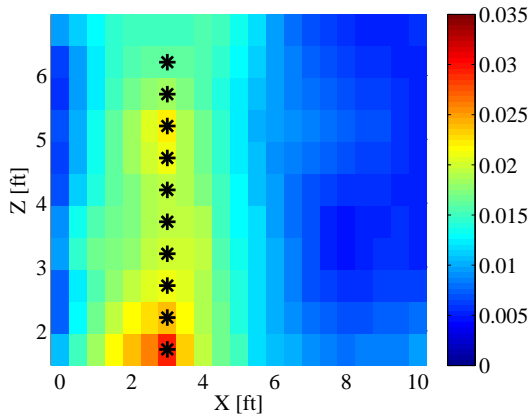
(b) Exp. 2 - Height: 5'1" | Weight: 130 lbs



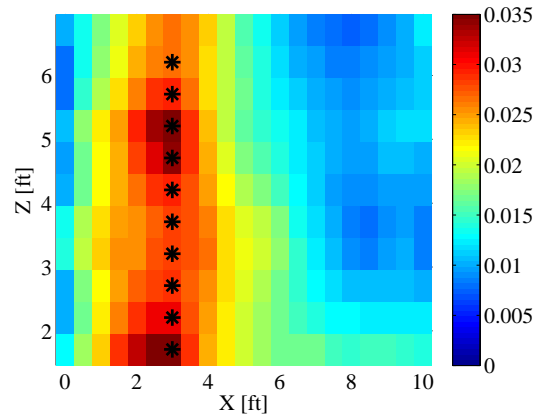
(c) Exp. 1 - Height: 5'8" | Weight: 190 lbs



(d) Exp. 2 - Height: 5'8" | Weight: 190 lbs

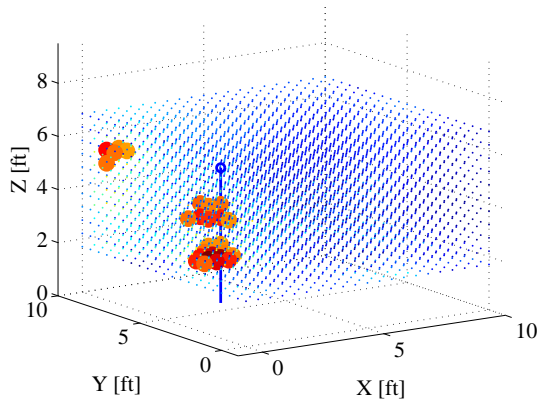


(e) Exp. 1 - Height: 6'1" | Weight: 185 lbs

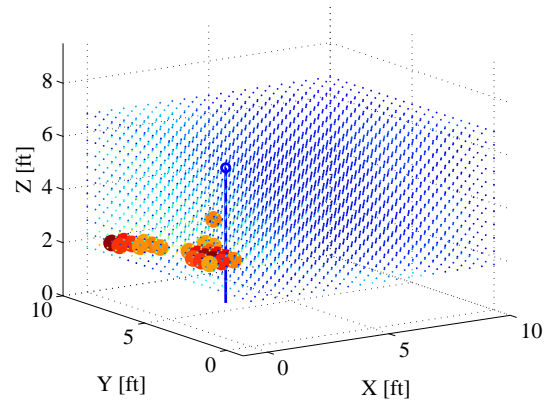


(f) Exp. 2 - Height: 6'1" | Weight: 185 lbs

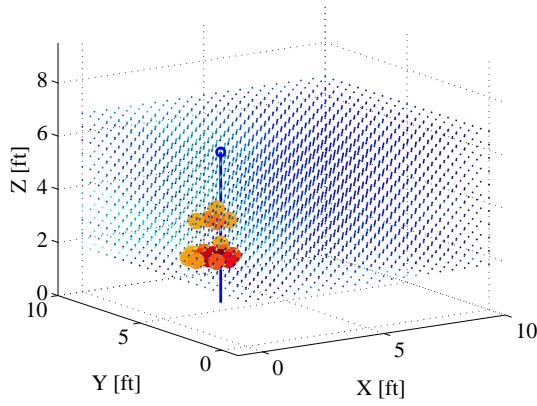
Figure 4.13: Comparison of 2-D lateral attenuation images, $\hat{\mathbf{x}}_{(3,6)}$ (dB/ft) of targets with different heights. Stationary target standing at $(x, y)_{sT} = (3, 6)$ ft. $\{\Delta_p = 0.5 \text{ ft} \mid \alpha = 500.0\}$



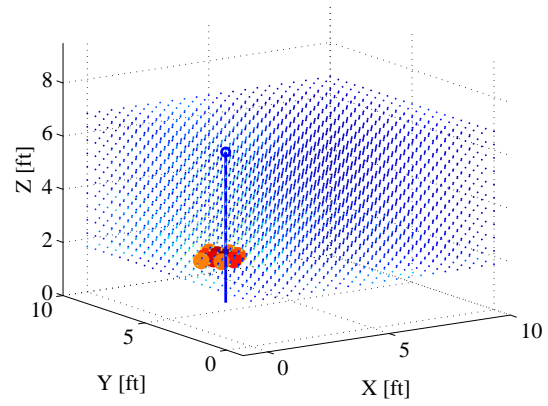
(a) Exp. 1 Target Height: 5'1"



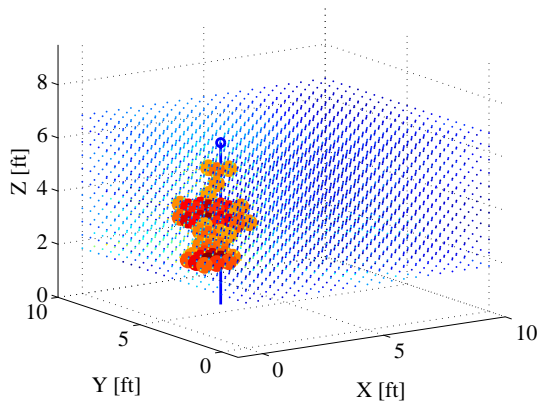
(b) Exp. 2 Target Height: 5'1"



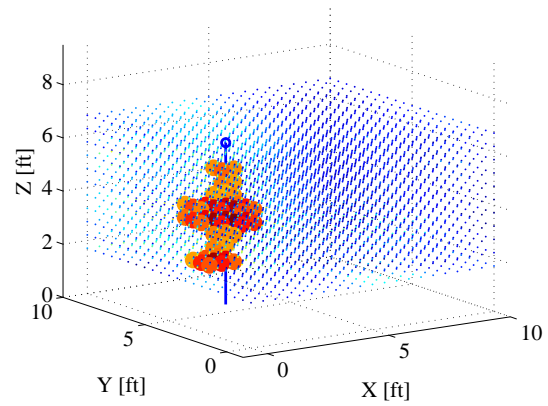
(c) Exp. 1 Target Height: 5'8"



(d) Exp. 2 Target Height: 5'8"

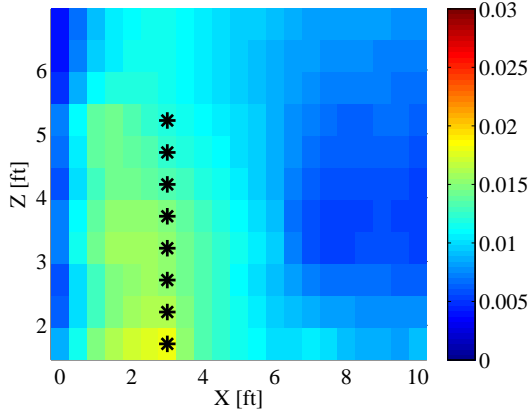


(e) Exp. 1 Target Height: 6'1"

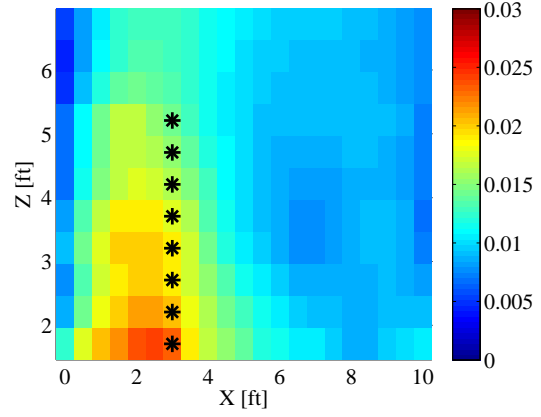


(f) Exp. 2 Target Height: 6'1"

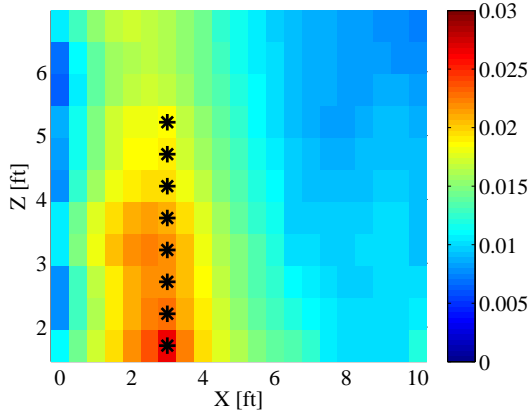
Figure 4.14: Comparison of 3-D attenuation images, $\hat{\mathbf{x}}_{(3,6)}$ (dB/ft) of targets with different heights. Stationary target standing at $(x, y)_{sT} = (3, 6)$ ft. $\{\Delta_p = 0.5 \text{ ft} \mid \alpha = 500.0\}$



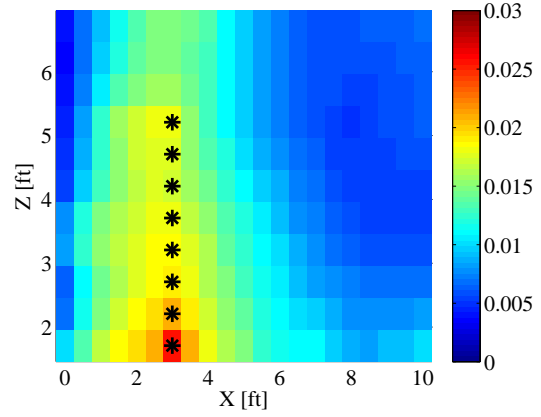
(a) Exp. 1 - Height: 5'1" | Weight: 130 lbs



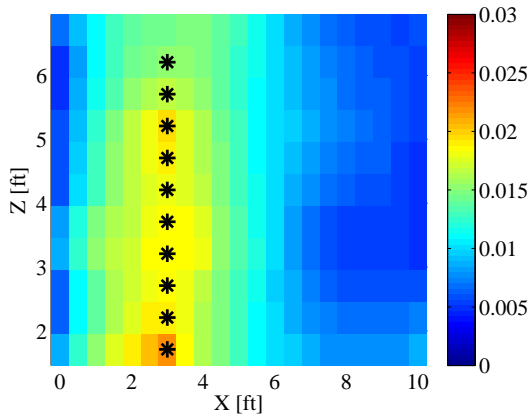
(b) Exp. 2 - Height: 5'1" | Weight: 130 lbs



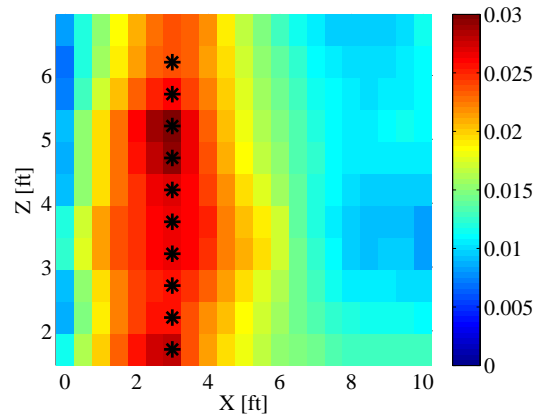
(c) Exp. 1 - Height: 5'8" | Weight: 190 lbs



(d) Exp. 2 - Height: 5'8" | Weight: 190 lbs

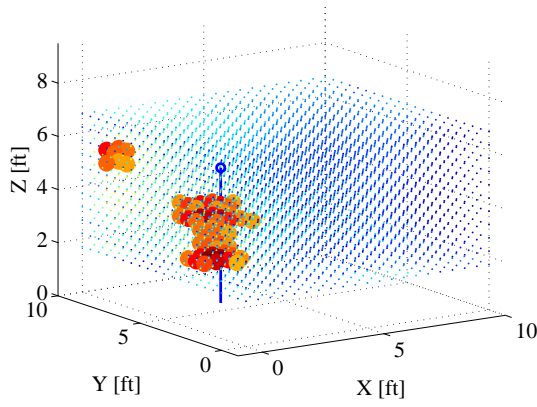


(e) Exp. 1 - Height: 6'1" | Weight: 185 lbs

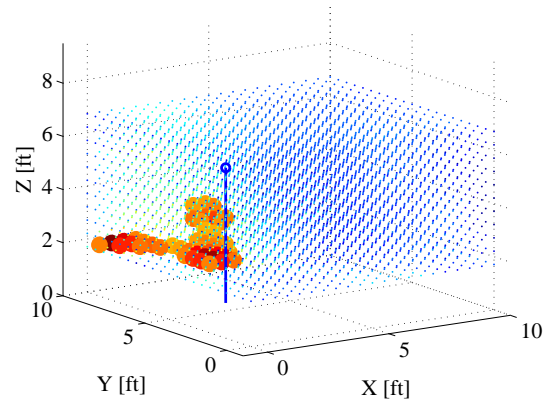


(f) Exp. 2 - Height: 6'1" | Weight: 185 lbs

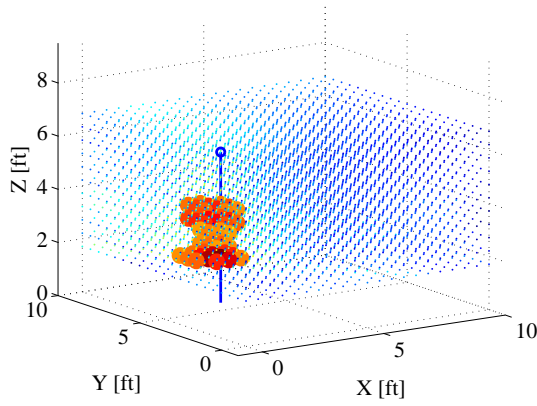
Figure 4.15: Comparison of 2-D lateral attenuation images, $\hat{\mathbf{x}}_{(3,6)}$ (dB/ft) of targets with different heights. Stationary target standing at $(x, y)_{sT} = (3, 6)$ ft. $\{\Delta_p = 0.5$ ft $|$ $\alpha = 1000.0$



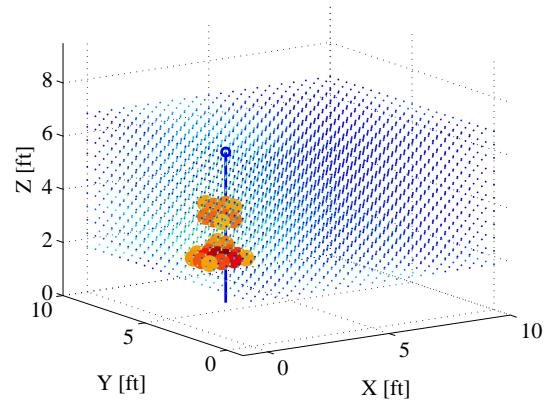
(a) Exp. 1 Target Height: 5'1"



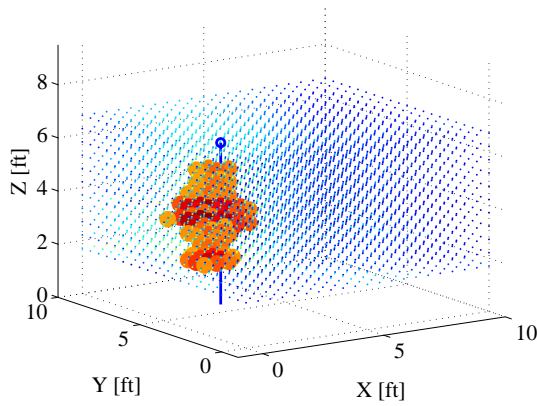
(b) Exp. 2 Target Height: 5'1"



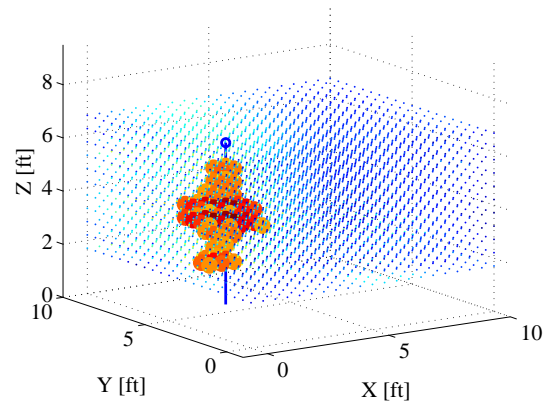
(c) Exp. 1 Target Height: 5'8"



(d) Exp. 2 Target Height: 5'8"

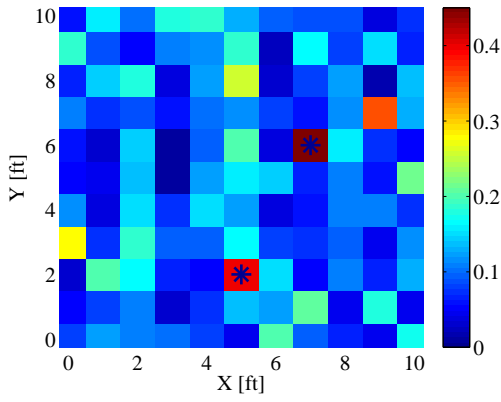


(e) Exp. 1 Target Height: 6'1"

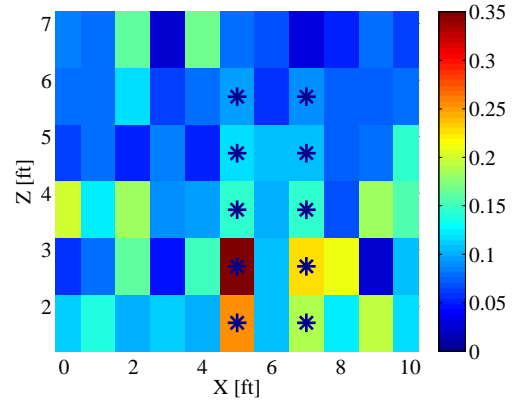


(f) Exp. 2 Target Height: 6'1"

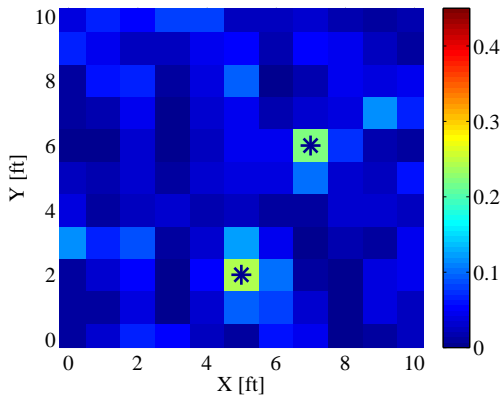
Figure 4.16: Comparison of 3-D attenuation images, $\hat{\mathbf{x}}_{(3,6)}$ (dB/ft) of targets with different heights. Stationary target standing at $(x, y)_{sT} = (3, 6)$ ft. $\{\Delta_p = 0.5 \text{ ft} \mid \alpha = 1000.0\}$



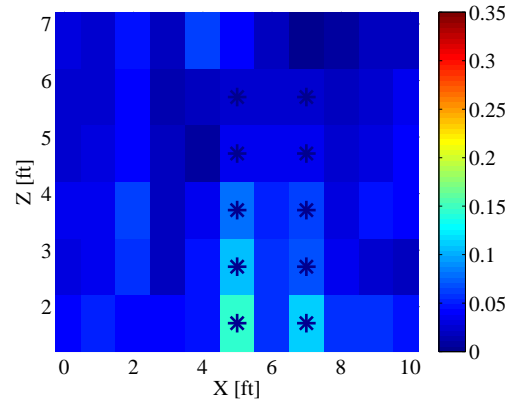
(a) Aerial View | $\alpha = 1.0$



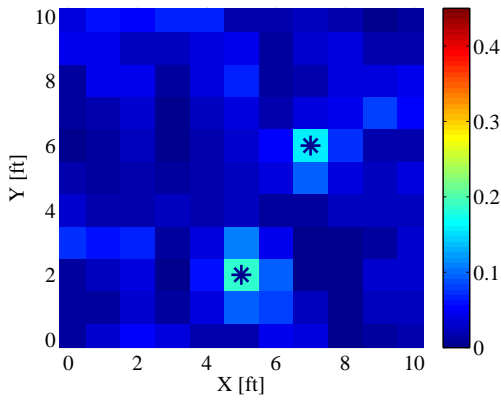
(b) Lateral View | $\alpha = 1.0$



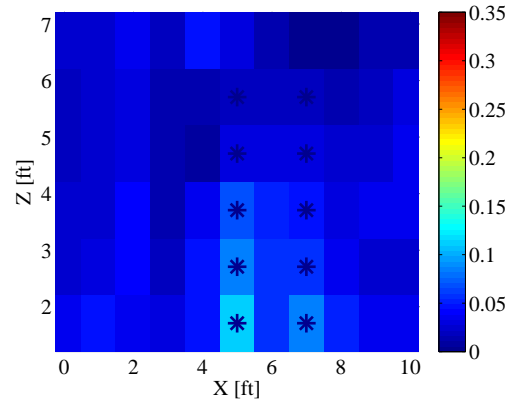
(c) Aerial View | $\alpha = 30.0$



(d) Lateral View | $\alpha = 30.0$

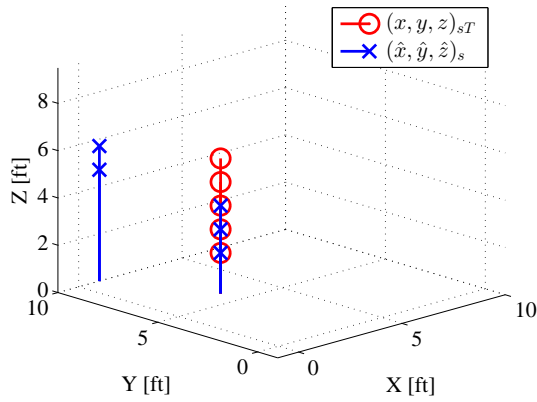


(e) Aerial View | $\alpha = 75.0$

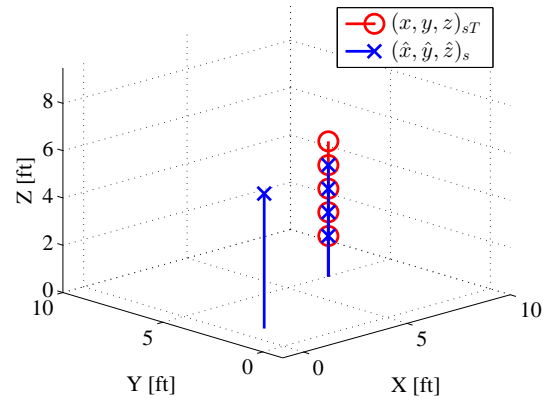


(f) Lateral View | $\alpha = 75.0$

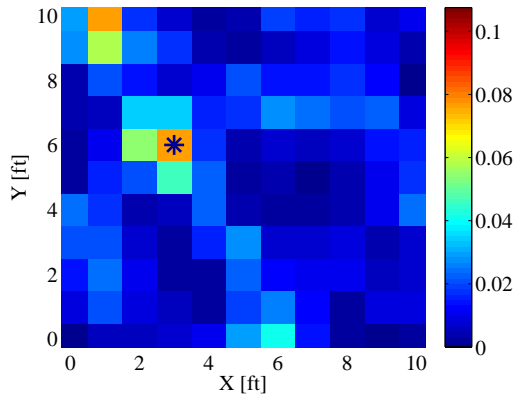
Figure 4.17: Relationship between α and 2-D attenuation images $\hat{\mathbf{x}}_{(5,2),(7,6)}$ (dB/ft) of two stationary targets standing at $(x, y)_{sT,1} = (5, 2)$ and $(x, y)_{sT,2} = (7, 6)$ ft where $\Delta_p = 1.0$ ft. Targets are 5'8'' and 5'4'' respectively.



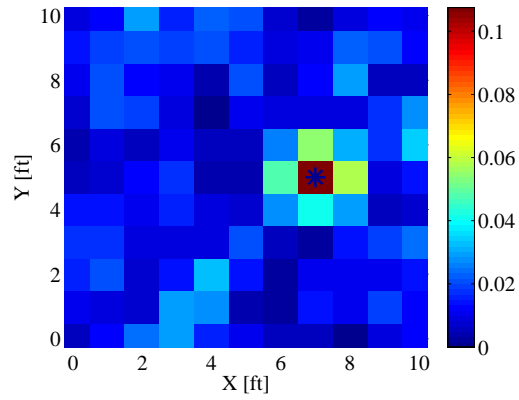
(a) $(\hat{x}, \hat{y}, \hat{z})_{(3,6,z)} \mid \epsilon_D = 1.79 \text{ ft}$



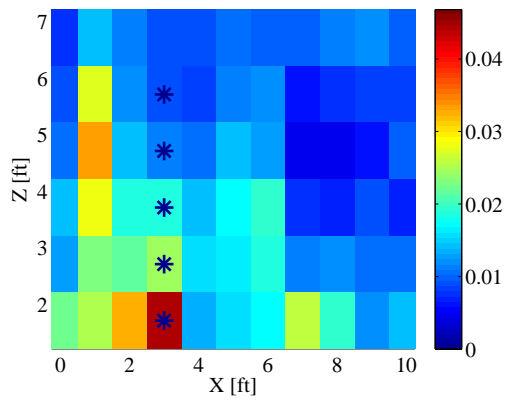
(b) $(\hat{x}, \hat{y}, \hat{z})_{(7,5,z)} \mid \epsilon_D = 1.34 \text{ ft}$



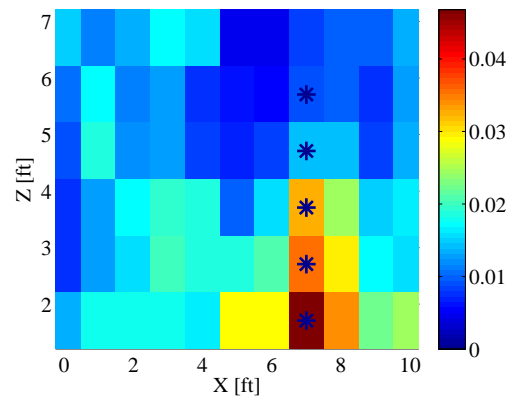
(c) Aerial View: $\hat{\mathbf{x}}_{(3,6)}$



(d) Aerial View: $\hat{\mathbf{x}}_{(7,5)}$

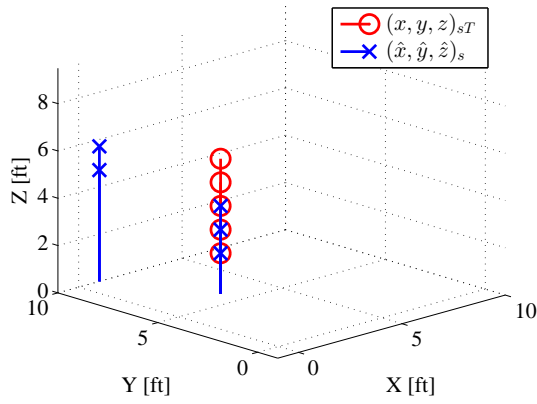


(e) Lateral View: $\hat{\mathbf{x}}_{(3,6)}$

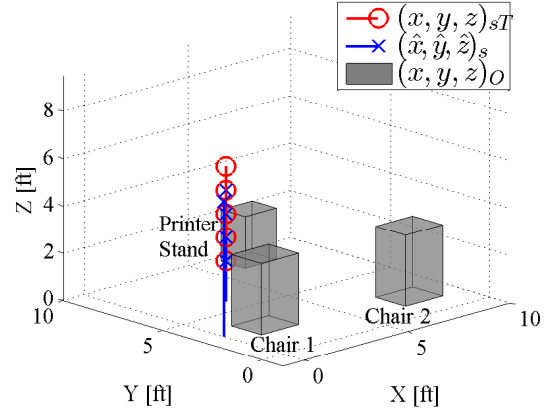


(f) Lateral View: $\hat{\mathbf{x}}_{(7,5)}$

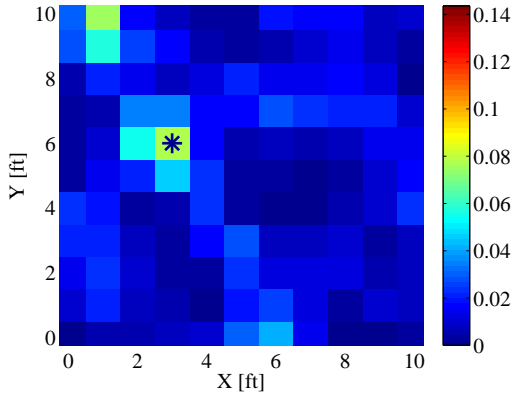
Figure 4.18: Comparison of 3-D position and 2-D attenuation images $\hat{\mathbf{x}}_{sT}$ (dB/ft) based on the position of a single stationary target who is 5'1". [$\alpha = 75.0 \mid \Delta_p = 1.0 \text{ ft}$].



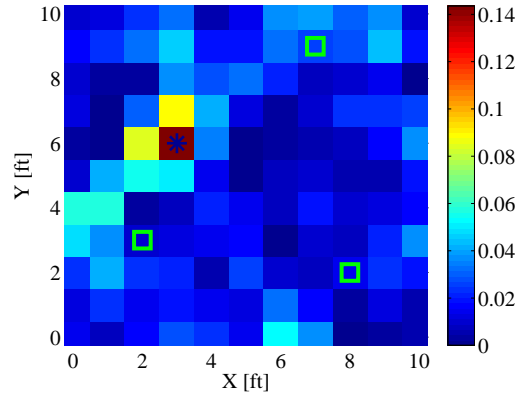
(a) $\epsilon_D = 1.79$ ft



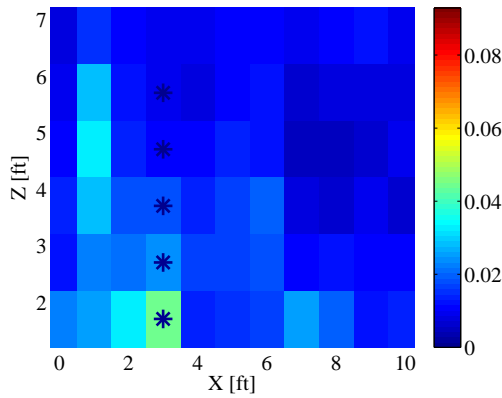
(b) $\epsilon_D = 0.85$ ft



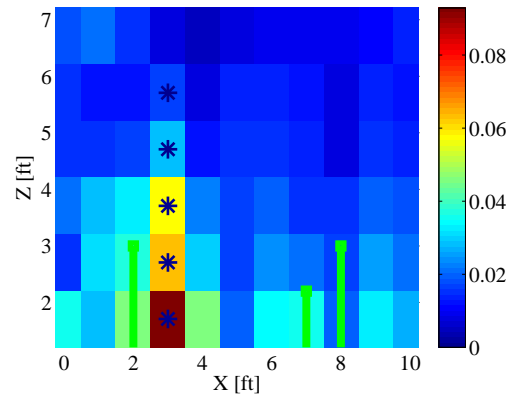
(c) Aerial View: $\hat{\mathbf{x}}_{(3,6)}$



(d) Aerial View: $\hat{\mathbf{x}}_{(3,6),O}$

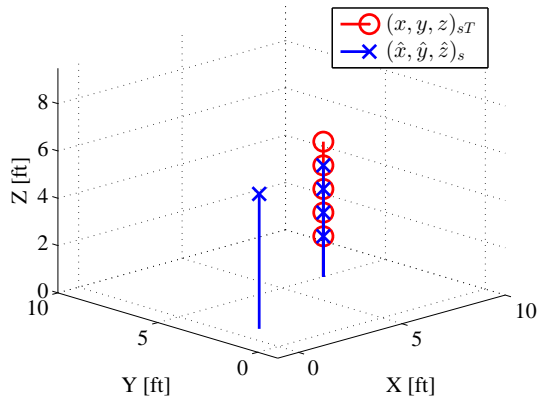


(e) Lateral View: $\hat{\mathbf{x}}_{(3,6)}$

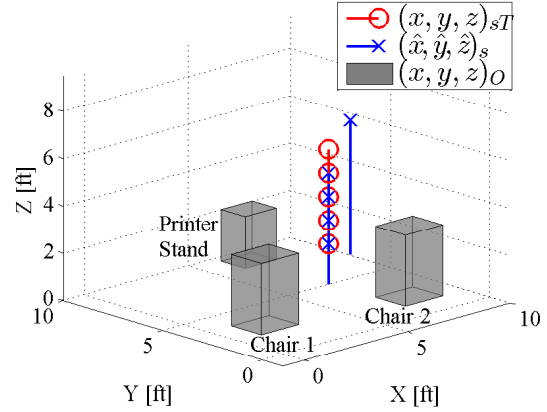


(f) Lateral View: $\hat{\mathbf{x}}_{(3,6),O}$

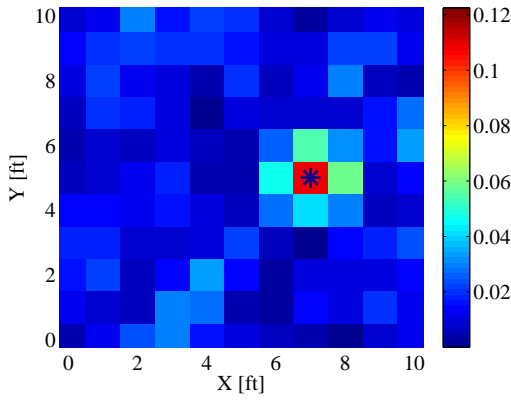
Figure 4.19: Comparison of 3-D position and 2-D attenuation images $\hat{\mathbf{x}}_{(3,6)}$ (dB/ft) for a stationary 5'1" target standing at $(x, y)_{sT} = (3, 6)$ ft with and without furniture within the area. The first column has the results from the unobstructed network and the second column has the results from the obstructed network [$\alpha = 75.0$ | $\Delta_p = 1.0$ ft].



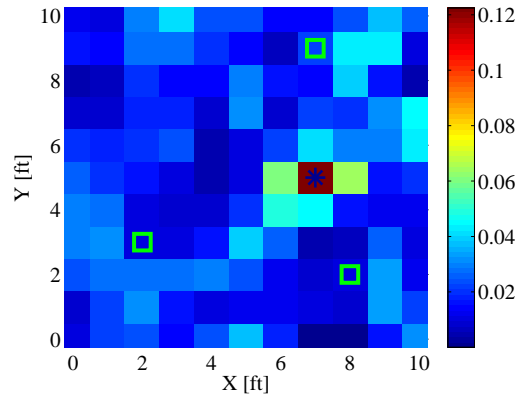
(a) $\epsilon_D = 1.34$ ft



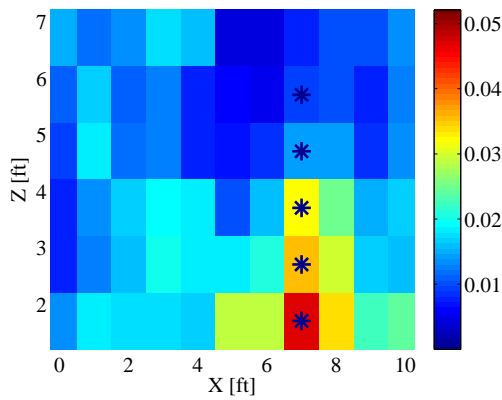
(b) $\epsilon_D = 0.72$ ft



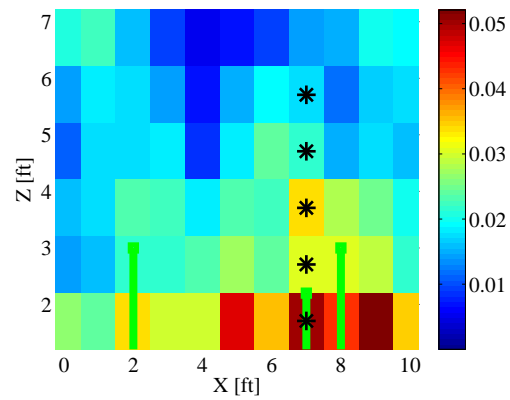
(c) Aerial View: $\hat{\mathbf{x}}_{(7,5)}$



(d) Aerial View: $\hat{\mathbf{x}}_{(7,5),O}$

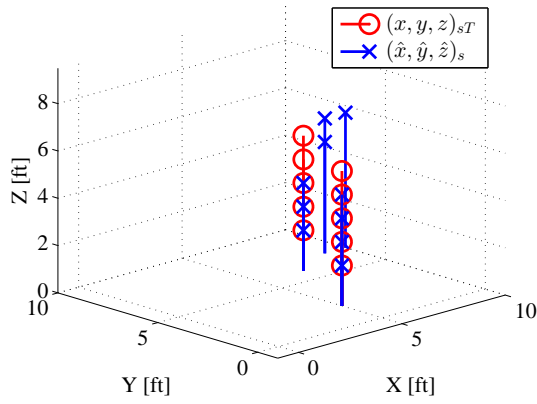


(e) Lateral View: $\hat{\mathbf{x}}_{(7,5)}$

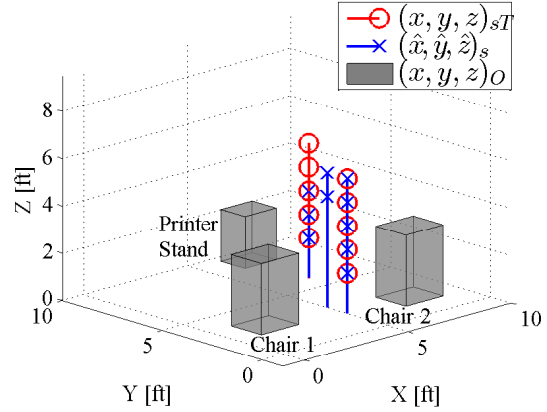


(f) Lateral View: $\hat{\mathbf{x}}_{(7,5),O}$

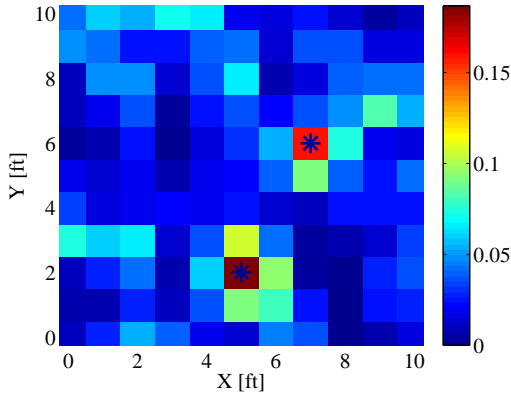
Figure 4.20: Comparison of 3-D position and 2-D attenuation images $\hat{\mathbf{x}}_{(7,5)}$ (dB/ft) for a stationary 5'1" target standing at $(x, y)_{sT} = (7, 5)$ ft with and without furniture within the area. The first column has the results from the unobstructed network and the second column has the results from the obstructed network [$\alpha = 75.0$ | $\Delta_p = 1.0$ ft].



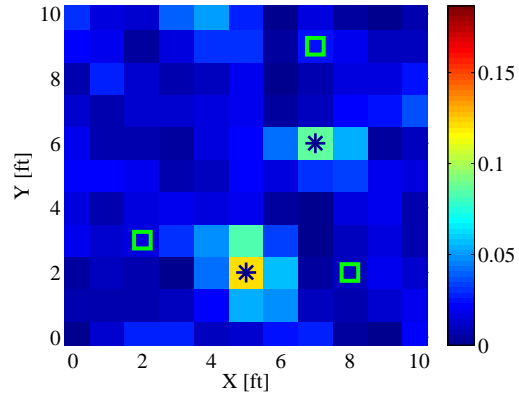
(a) $\epsilon_D = 2.74$ ft



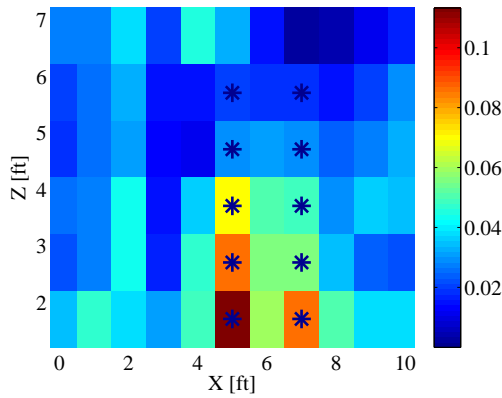
(b) $\epsilon_D = 3.13$ ft



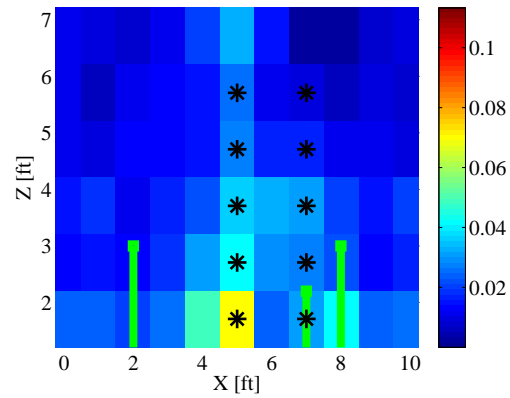
(c) Aerial View: $\hat{\mathbf{x}}_{(5,2)|(7,6)}$



(d) Aerial View: $\hat{\mathbf{x}}_{(5,2)|(7,6),O}$



(e) Lateral View: $\hat{\mathbf{x}}_{(5,2)|(7,6)}$



(f) Lateral View: $\hat{\mathbf{x}}_{(5,2)|(7,6),O}$

Figure 4.21: Comparison of 3-D position and 2-D attenuation images $\hat{\mathbf{x}}_{(5,2),(7,6)}$ (dB/ft) for the same two stationary targets standing at $(x, y)_{sT,1} = (5, 2)$ and $(x, y)_{sT,2} = (7, 6)$ ft with and without furniture within the area. Targets are 5'8" and 5'4" respectively. The first column has the results from the unobstructed network and the second column has the results from the obstructed network [$\alpha = 75.0$ | $\Delta_p = 1.0$ ft].

4.2 Motion Tracking

There were three categories of motion tracking experiments conducted each consisting of a single target. In the first set, there were no additional obstructions in the environment and the target walked a longer more comprehensive path covering a larger area. A walking pace was chosen using a metronome tempo trainer by comparing the subsequent results from these experiments. The next two sets of experiments included additional obstructions and covered shorter paths through the network so they were shorter in duration comparatively. The purpose of these experiments was to establish a baseline for the spatial pattern monitoring experiments. Table 4.3 shows the average normalized MSE_R of the aerial pseudo-attenuation images generated as a function of α from each experiment. The average normalized MSE_R was lowest when $\Delta_p = 1.0$ ft. There was very little dispersion in error across the range of α . Figure 4.22 further illustrates the little impact α has on the set of single target, motion tracking experiments. Experiments using path 2 had a lower average normalized MSE_R than experiments using path 1.

Table 4.3: Average normalized mean squared error, $\overline{NMSE_R}$ and standard deviation, $\sigma_{\overline{NMSE_R}}$ of single target motion tracking experiments using aerial pseudo-attenuation images evaluated over α .

Experiment Details			$\overline{NMSE_R}$		$\sigma_{\overline{NMSE_R}}$	
<i>Path</i>	$(x, y)_{mT}$	<i>Obstructions</i>	$\Delta_p = 0.5$ ft	$\Delta_p = 1.0$ ft	$\Delta_p = 0.5$ ft	$\Delta_p = 1.0$ ft
Triangle	(2,8)-(2,2)-(8,2)	No	0.23	0.067	0.00	0.00
Path 1	(3,4)-(7,8)	Yes	0.07	0.01	0.00	0.00
Path 2	(7,3)-(7,8)	Yes	0.07	0.00	0.00	0.00

Figures 4.23, 4.24, and 4.25 illustrate the pseudo-attenuation images generated after removing estimated pixel attenuation values less than 50% of the maximum attenuation value registered during the entire data set $\hat{\mathbf{x}}_p \leq 0.5\hat{\mathbf{x}}_{MAX}$ yielding a “clean-estimate”. The choice to remove estimates below 50% was made through visual inspection of various

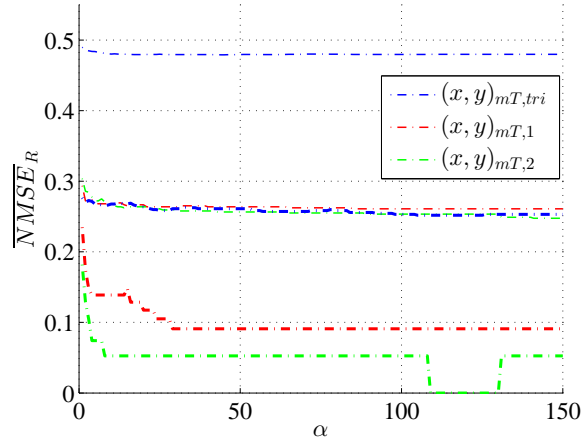
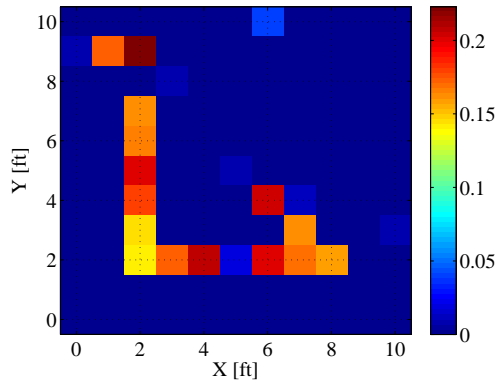


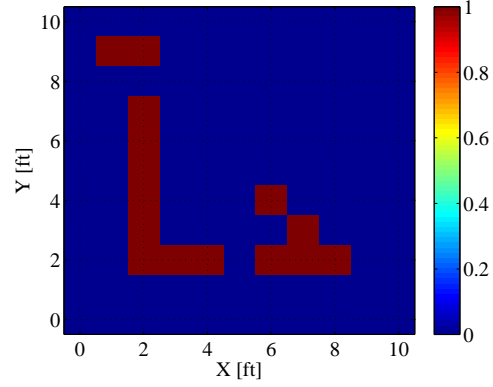
Figure 4.22: Average normalized mean squared error as a function of α and Δ_p of single target motion tracking experiments for each path. The bold lines represent $\Delta_p = 1.0$ ft, and the lighter lines represent $\Delta_p = 0.5$ ft. $\{\alpha = [1.0 : 1.0 : 150.0]\}$

experimental results. Estimates registering such low attenuation values in comparison to the strongest registered attenuation value were generally attributable to the sporadic nature of RTI when targets are moving and were not accurate position estimates.

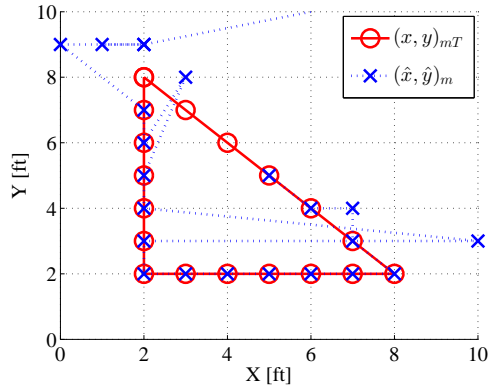
Figure 4.26 provides a comparison of the histograms illustrating the occupied pixel frequency over the course of the particular data collection set for each type of motion tracking experiment. As expected, the high traffic areas are evident because the corresponding pixels registered a target's presence during one frame or another. Additionally, the number of times a particular pixel was occupied is only on the order of single digits because the target was constantly moving and only traveled the path once in the case of $(x, y)_{mT, tri}$ and twice for paths 1 and 2. The values are not exactly even for each pixel likely due to a combination of the sporadic nature of RTI and the instances when a target was occupying two pixels during one frame of measurements.



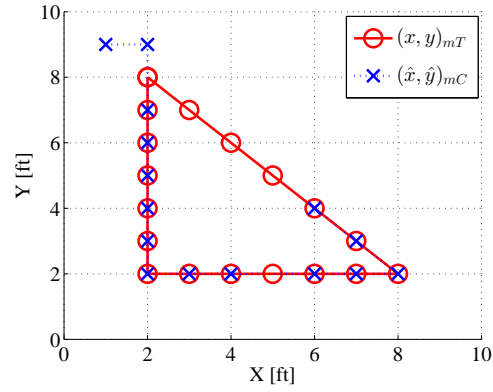
(a) $\hat{\mathbf{x}}_{p,MAX}$ per frame



(b) $\hat{\mathbf{x}}_{mC,tri} \mid NMS E_R = 0.06$

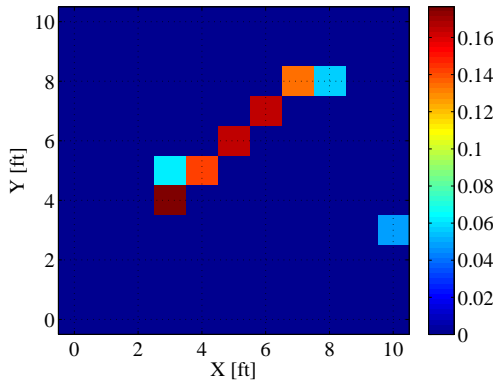


(c) Original path estimate

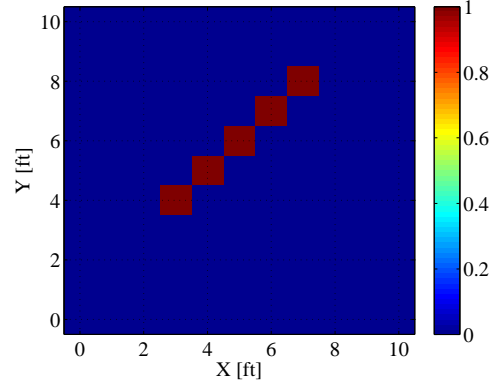


(d) Clean-path estimate

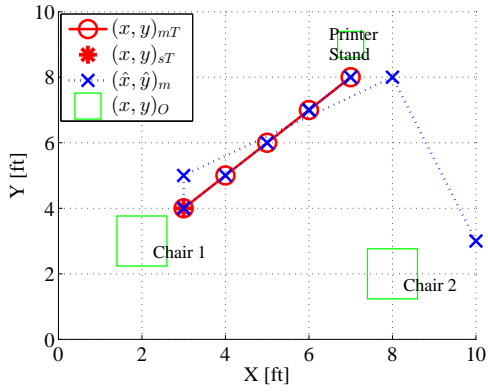
Figure 4.23: Pseudo-attenuation image estimate and path estimates of a single target traveling the path $(x, y)_{mT,tri} = (2, 8) - (2, 2) - (8, 2)$ ft. Clean estimates are a result of throwing out each $\hat{\mathbf{x}}_p \leq 0.5 \times \hat{\mathbf{x}}_{MAX}$. $\{\Delta_p = 1.0 \text{ ft} \mid \alpha = 75.0\}$



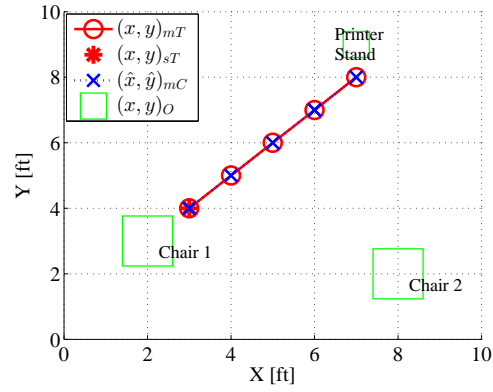
(a) $\hat{\mathbf{x}}_{p,MAX}$ per frame



(b) $\hat{\mathbf{x}}_{mC,1} \mid NMS E_R = 0.00$

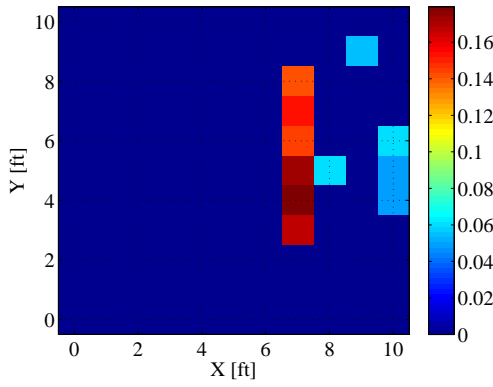


(c) Original path estimate

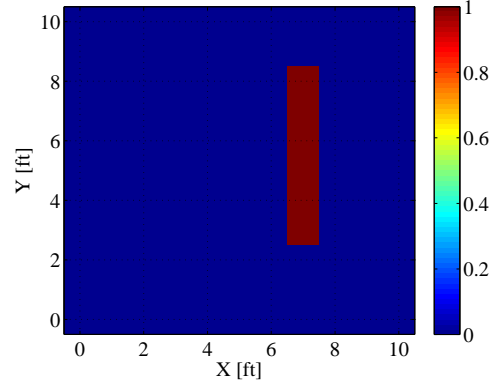


(d) Clean-path estimate

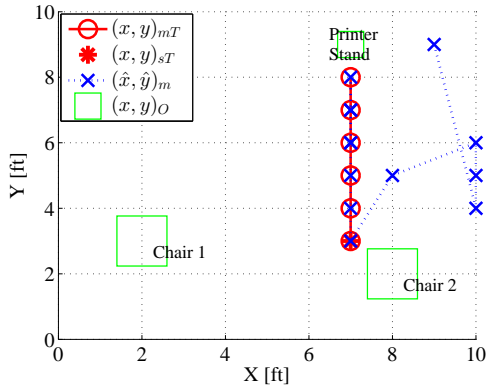
Figure 4.24: Pseudo-attenuation image estimate and path estimates of a single target traveling the path $(x, y)_{mT,2} = (3, 4) - (7, 8)$ ft. Clean estimates are a result of throwing out each $\hat{\mathbf{x}}_p \leq 0.5 \times \hat{\mathbf{x}}_{MAX}$. $\hat{\mathbf{x}}_p \leq 0.5 \times \hat{\mathbf{x}}_{MAX}$. $\{\Delta_p = 1.0 \text{ ft} \mid \alpha = 75.0\}$



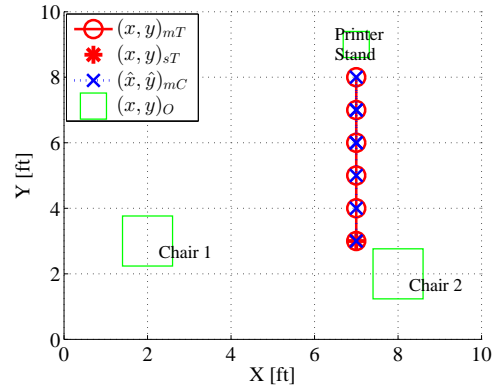
(a) $\hat{\mathbf{x}}_{p,MAX}$ per frame



(b) $\hat{\mathbf{x}}_{mC,1} \mid NMS E_R = 0.00$

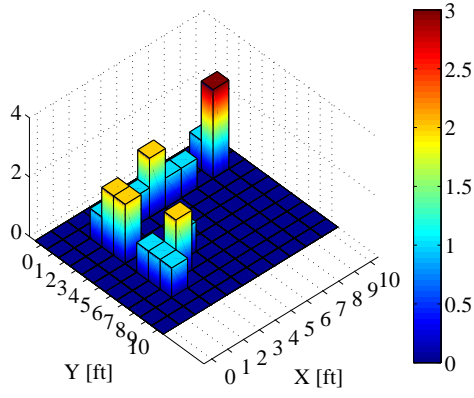


(c) Original path estimate

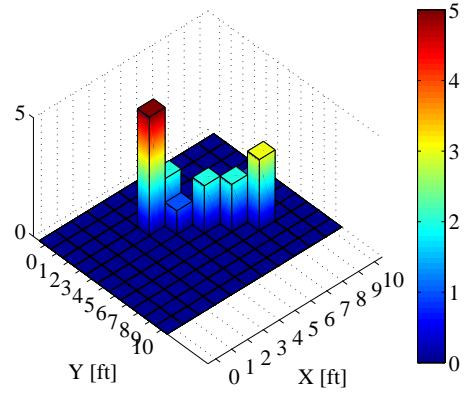


(d) Clean-path estimate

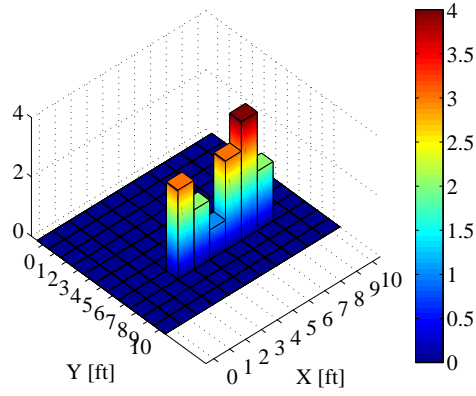
Figure 4.25: Pseudo-attenuation image estimate and path estimates of a single target traveling the path $(x, y)_{mT,2} = (7, 3) - (7, 8)$ ft. Clean estimates are a result of throwing out each $\hat{\mathbf{x}}_p \leq 0.5 \times \hat{\mathbf{x}}_{MAX}$. $\hat{\mathbf{x}}_p \leq 0.5 \times \hat{\mathbf{x}}_{MAX}$. $\{\Delta_p = 1.0 \text{ ft} \mid \alpha = 75.0\}$



(a) $(x, y)_{mT,tri} = (2, 8) - (2, 2) - (8, 2)$



(b) $(x, y)_{mT,2} = (3, 4) - (7, 8)$



(c) $(x, y)_{mT,2} = (7, 3) - (7, 8)$

Figure 4.26: Histograms results for short duration controlled motion tracking experiments of a single target where $\alpha = 75.0$ and $\Delta_p = 1.0$ ft.

4.3 Spatial Pattern Monitoring

The results of the previous series of experiments were used to provide an experimental method for choosing values for α and Δ . They also provided an avenue for verifying the ability of the established RTI network used in this research to accurately locate and track targets in a naturally obstructed environment. The results from the shorter duration motion tracking experiments provided insight into the expected outcome of spatial pattern monitoring experiments longer in duration which were similar in the selected primary positions and paths.

A set of single target spatial pattern monitoring experiments was conducted for each path where the number of times each path was traveled, λ_T , was varied. Each experiment lasted for 9 minutes. The purpose of these experiments was to show that the high traffic pattern illustrated in the histograms between two experiments with different λ_T would be distinguishable in scale but the paths would still be identifiable as the same.

Additionally, spatial pattern monitoring experiments with only one target were done prior to introducing the second target because it had already been shown that localizing and imaging two targets was generally more challenging than localizing and imaging a single target. The two-target spatial pattern monitoring experiments utilized the same paths as those in the single target spatial pattern monitoring experiments. The expectation was that the results between them would be similar with respect to the path traveled and λ_T .

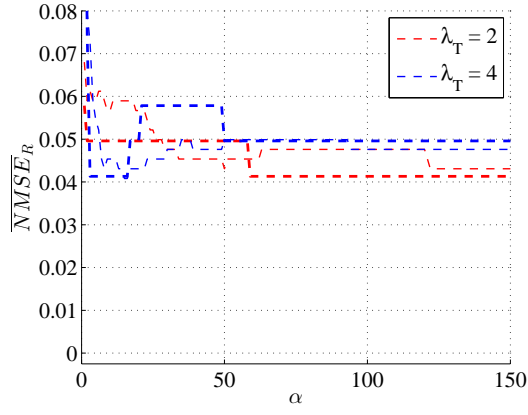
Figure 4.27 illustrates the average normalized MSE_R as a function of α , Δ_p , λ_T , and the path traveled. Varying each of these parameters for path 1 resulted in little change in the average normalized MSE_R . The impact of varying these parameters in the spatial pattern monitoring experiments for path 2 was clearer and more consistent. When $\lambda_T = 4$ there is more movement within the network over the entire data collection period; the target is moving more often than it is remaining stationary. As a result, the average normalized MSE_R is higher for experiments when the path is traveled more frequently because the

RTI network used in this research proved less effective at motion tracking as opposed to stationary localization.

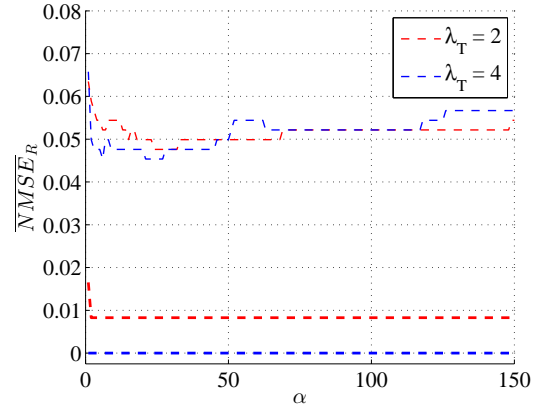
Figures 4.28 and 4.29 illustrate the time-averaged clean-path estimates and histograms from the single target spatial pattern monitoring experiments for each path as λ_T is varied. The histogram images for each experiment are very similar. The noticeable differences are the presence of more noise in the path 1 attenuation images, and the range of histogram values for each experiment as a function of λ_T . When the path is traveled less frequently, the primary position is occupied more often and therefore a higher value is present in that pixel. As λ_T is increased, the primary position value is reduced and the pixels that lie in the traveled path have higher values respectively. The final pixel at the end of each path, opposite of the primary position, has a higher value than the intermediate pixels because it is the target's turn around point.

Figure 4.30 introduces the average normalized MSE_R for the spatial pattern monitoring experiments of two targets. Even though λ_T is varied for each path between the two experiments, the total number of times any path is traveled between the two experiments is the same, so, as expected, the average normalized MSE_R is relatively consistent between them. Figure 4.31 compares the average normalized MSE_R of a single two-target spatial pattern monitoring experiment with the two corresponding single target spatial pattern monitoring experiments based on λ_T per path.

Figure 4.32 shows the clean, pseudo-attenuation images for each two-target spatial pattern monitoring experiment. As expected the images are also similar as were the average normalized MSE_R results presented in Figure 4.31. Figure 4.33 provides the final histogram results from two different viewpoints for the two spatial pattern monitoring experiments of two targets. The two paths are identifiable as high traffic areas, and their histogram values are representative of the value of λ_T . Path 1 is not as distinguishable as path 2 regardless of λ_T .

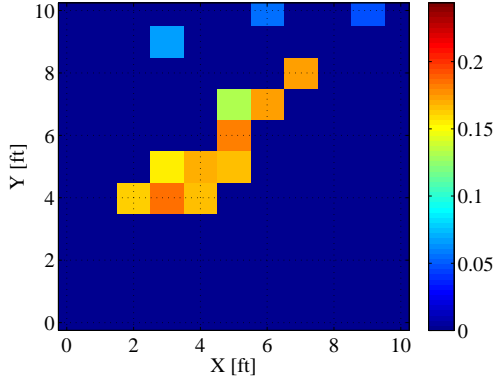


(a) $(x, y)_{mT,1} = (3, 4) - (7, 8)$

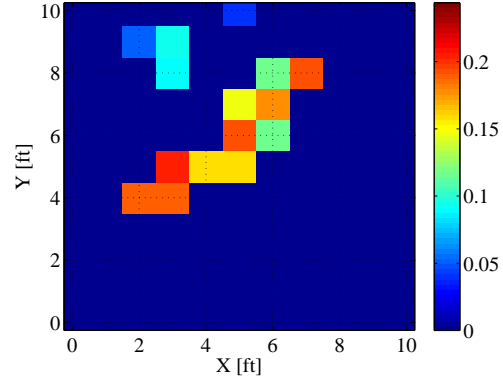


(b) $(x, y)_{mT,2} = (7, 3) - (7, 8)$

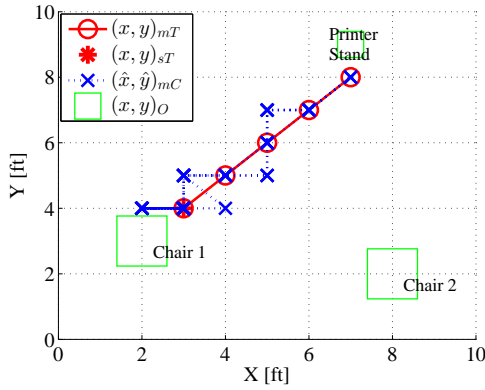
Figure 4.27: Average normalized mean squared error as a function of α and Δ_p of spatial pattern monitoring experiments with one target. Each figure illustrates the estimation error based on the path traveled, how often the path was traveled λ_T , and pixel size Δ_p . The bold lines represent $\Delta_p = 1.0$ ft, and the lighter lines represent $\Delta_p = 0.5$ ft. $\{\alpha = [1.0 : 1.0 : 150.0]\}$



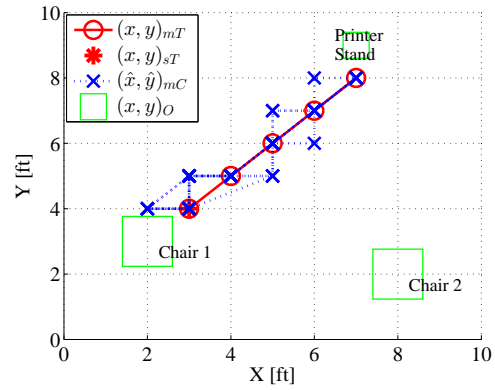
(a) $\hat{\mathbf{x}}_{p,MAX}$ per frame $|\lambda_{T,1} = 2$



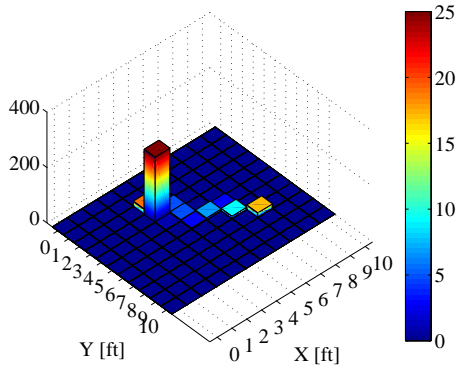
(b) $\hat{\mathbf{x}}_{p,MAX}$ per frame $|\lambda_{T,1} = 4$



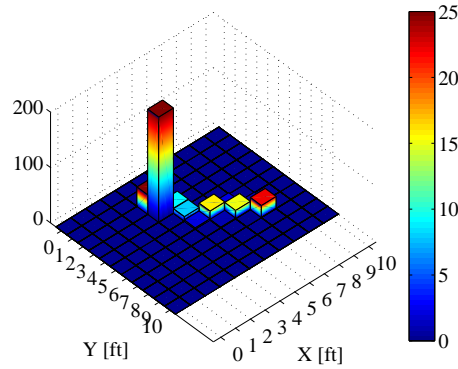
(c) Clean-path estimate $|\lambda_{T,1} = 2$



(d) Clean-path estimate $|\lambda_{T,1} = 4$

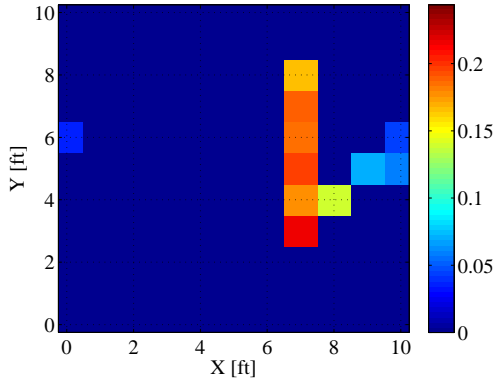


(e) $\lambda_{T,1} = 2$

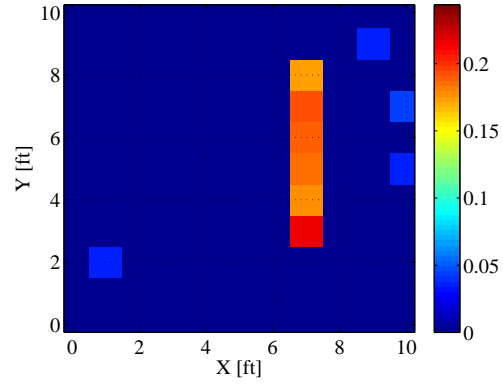


(f) $\lambda_{T,1} = 4$

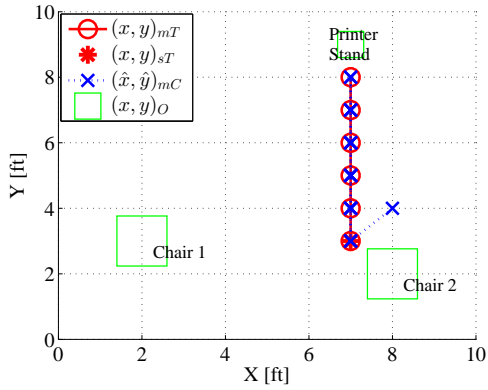
Figure 4.28: Clean-path estimates and histogram results for single target, spatial pattern monitoring with varied trip frequency λ_T over the path. Plotted values are scaled between 0 and 25 for visual clarity as shown on the colorbar. The z -axis illustrates true counts. $(x, y)_{mT,1} [\alpha = 75.0 | \Delta_p = 1.0 \text{ ft}]$.



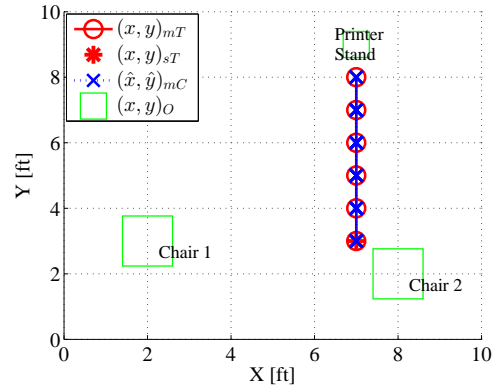
(a) $\hat{\mathbf{x}}_{p,MAX}$ per frame | $\lambda_{T,1} = 2$



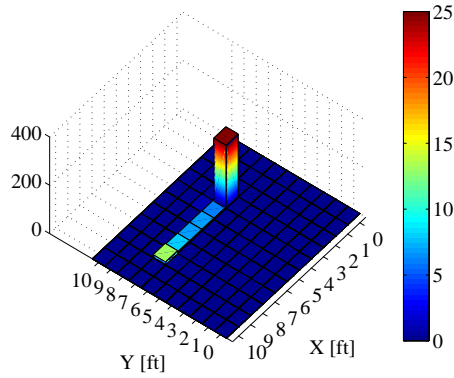
(b) $\hat{\mathbf{x}}_{p,MAX}$ per frame | $\lambda_{T,1} = 4$



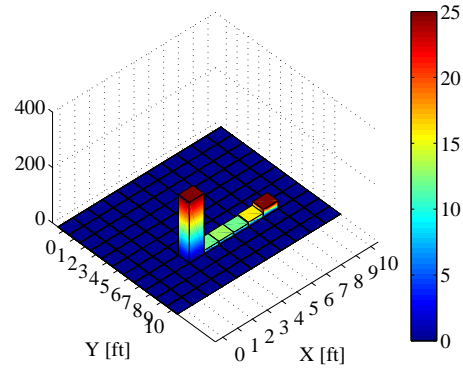
(c) Clean-path estimate | $\lambda_{T,2} = 2$



(d) Clean-path estimate | $\lambda_{T,2} = 4$



(e) $\lambda_{T,2} = 2$



(f) $\lambda_{T,2} = 4$

Figure 4.29: Clean-path estimates and histogram results for single target, spatial pattern monitoring with varied trip frequency λ_T over the path. Plotted values are scaled between 0 and 25 for visual clarity as shown on the colorbar. The z -axis illustrates true counts. $(x, y)_{mT,2}$ [$\alpha = 75.0$ | $\Delta_p = 1.0$ ft].

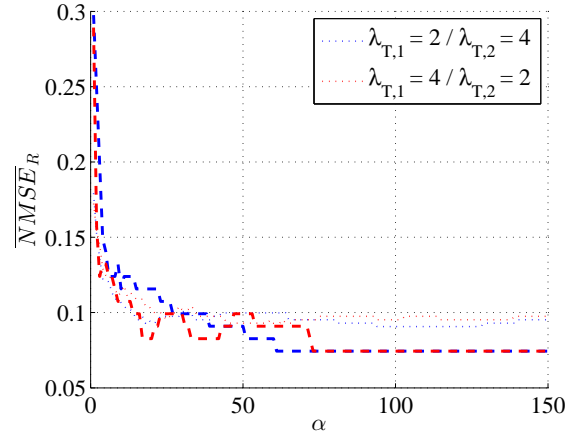
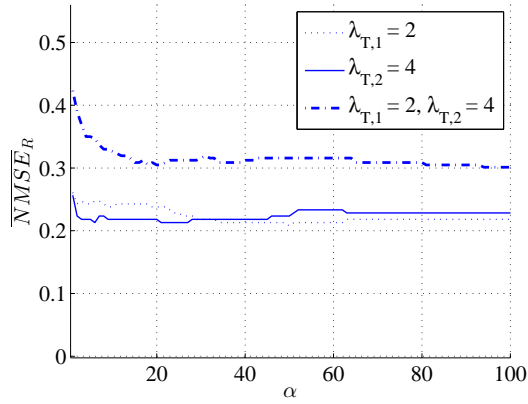
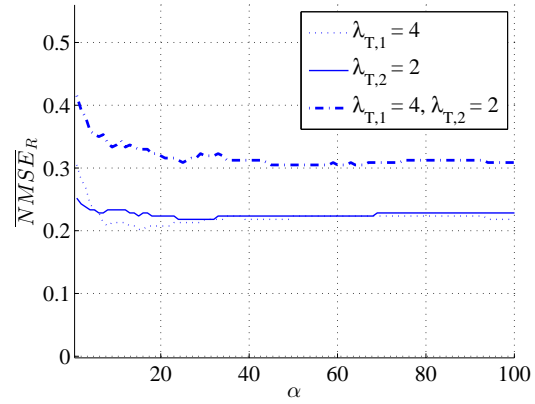


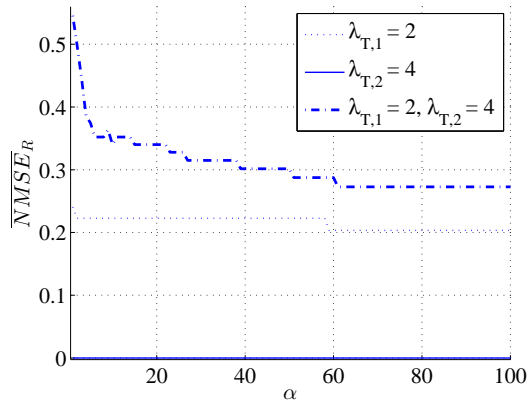
Figure 4.30: Average normalized mean squared error as a function of α and Δ_p of spatial pattern monitoring experiments with two targets. Illustrates the estimation error based on how often the respective path was traveled λ_T , and pixel size Δ_p . The bold lines represent $\Delta_p = 1.0$ ft, and the lighter lines represent $\Delta_p = 0.5$ ft. λ_T was varied between the two experiments.



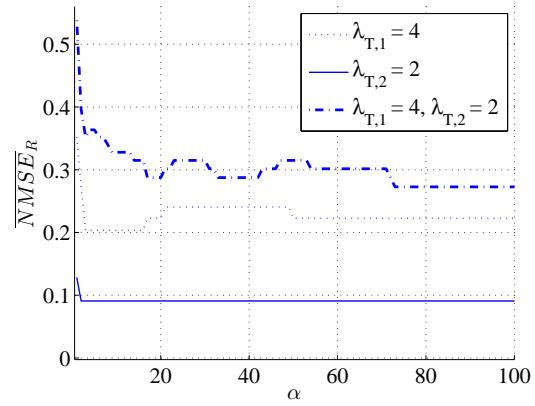
(a) $\Delta_p = 0.5$ ft.



(b) $\Delta_p = 0.5$ ft.

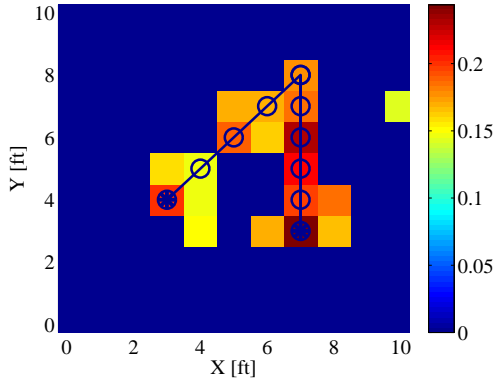


(c) $\Delta_p = 1.0$ ft.

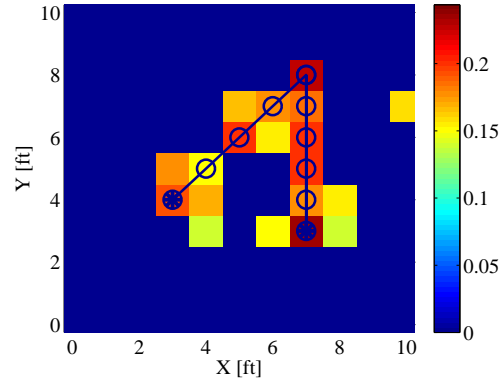


(d) $\Delta_p = 1.0$ ft.

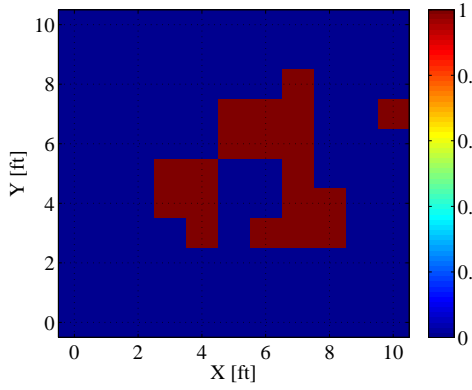
Figure 4.31: Average normalized mean squared error as a function of α and Δ_p of spatial pattern monitoring experiments. Each figure illustrates the estimation error based on the path traveled, how often the path was traveled λ_T , and the number of targets. The bold lines represent the experiments with two targets, and the lighter lines represent experiments with one target.



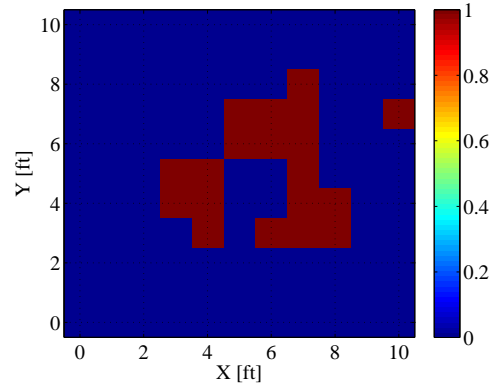
(a) $\hat{\mathbf{x}}_{p,MAX}$ per frame



(b) $\hat{\mathbf{x}}_{p,MAX}$ per frame

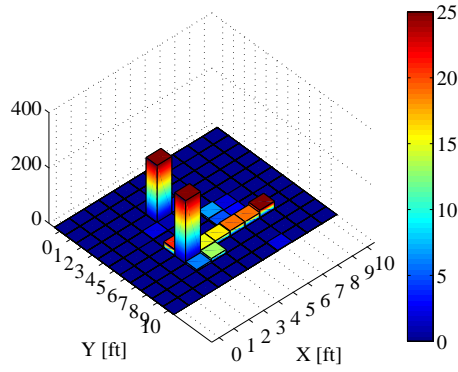


(c) $\hat{\mathbf{x}}_{mC} \mid NMS E_R = 0.07$

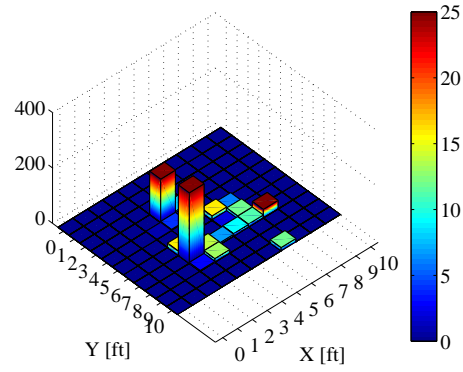


(d) $\hat{\mathbf{x}}_{mC} \mid NMS E_R = 0.1240$

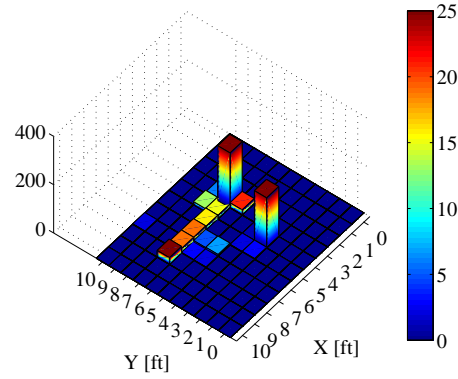
Figure 4.32: Estimates from two target, spatial pattern monitoring experiments with varied trip frequency λ_T per path. The first column contains the results for $\lambda_{T,1} = 2$ and $\lambda_{T,2} = 4$, and the second column contains the results for $\lambda_{T,1} = 4$ and $\lambda_{T,2} = 2$. [$\alpha = 75.0 \mid \Delta_p = 1.0$ ft]



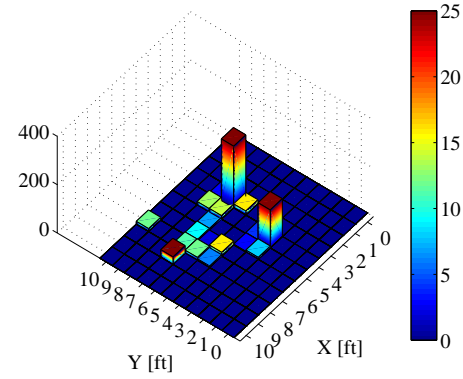
(a) $\lambda_{T,1} = 2 \mid \lambda_{T,2} = 4$



(b) $\lambda_{T,1} = 4 \mid \lambda_{T,2} = 2$



(c) $\lambda_{T,1} = 2 \mid \lambda_{T,2} = 4$



(d) $\lambda_{T,1} = 4 \mid \lambda_{T,2} = 2$

Figure 4.33: Multiple viewpoints of histogram results from spatial pattern monitoring experiments for two targets with varied trip frequency λ_T per path. Plotted values are scaled between 0 and 25 for visual clarity as shown on the colorbar. The z -axis illustrates true counts. [$\alpha = 75.0 \mid \Delta_p = 1.0$ ft]

4.4 Chapter Summary

This chapter presented results of various stationary localization, motion tracking, and spatial pattern monitoring experiments for one and two targets both in unobstructed and obstructed networks. The RTI network appeared most effective in single target, stationary localization. Introducing additional obstructions in the environment had little effect, as did the choice of the regularization parameter in position estimation. The choice of pixel size had more of an impact in localization accuracy especially for lower values of the regularization parameter.

V. Conclusion and Future Work

THIS chapter summarizes this thesis, presents research conclusions, and provides recommendations for future work. The growing field of DFL has sparked the exploration of WSNs constructed of small, inexpensive RFICs. Promising research exists in the application of WSN-based RTI for use in quality and inventory monitoring, surveillance, classification, and localization. RTI is especially useful in situations where there is a need for flexibility and privacy. Various models are used to form the entire RTI problem, including signal propagation, measurement, attenuation weighting, obstructions, and environment topography. Several models from each area were discussed in Chapter 2. As an inverse, ill-posed problem, RTI requires estimation and regularization techniques that can combat model sparsity effects in image reconstruction. Several common estimation and regularization techniques in the literature were also presented in Chapter 2.

This thesis explored a new application for RTI. A 3-D WSN consisting of 80 RFICs was constructed and used to monitor asset movement over a prolonged period of time in an indoor, moderately obstructed environment. Monitoring asset movement can be useful to identify high traffic patterns in an area such as an office, and thus can be used to effectively determine the placement of office equipment and furniture to maximize workplace comfort and efficiency. Preliminary stationary localization experiments were used to explore the ability of a 3-D RTI network to produce 3-D position and attenuation estimates, and furthermore, to determine if target features such as height, size, and density could be extracted from attenuation images.

In a series of controlled, coordinated spatial pattern monitoring experiments consisting of both a single target and two targets, position estimates from each data frame were used to build running totals of occupied pixels over time. The data from each spatial pattern monitoring experiment were presented in histograms to illustrate high traffic patterns and

frequently occupied positions. The results from the set of single target experiments were as expected. The primary positions and paths were identifiable, and the comparisons between similar experiments led to recognizable differences in the scale of the histogram based on λ_T .

The results from the two spatial pattern monitoring experiments with two targets produced identifiable high traffic patterns, but they weren't as clear or consistent as those from single target experiments. The two primary positions and paths were identifiable; however, path 1 was not as prominent as path 2 in both sets of results regardless of λ_T . It is likely the noise and multipath generated from two moving targets is the cause; however, more research would be needed to make that conclusion.

The results from this research provide a preliminary indication that an RTI WSN can be effectively used to monitor the usage of a space by identifying high traffic patterns used by assets within a sensed area. In a fully functioning office environment there will be an increased number of assets to track, significantly more furniture constructed of a variety of materials, and possibly the inclusion of walls. Therefore there is still more research needed to fully vet the capability of an RTI WSN in this capacity.

The 2-D lateral and 3-D attenuation images from a series of experiments where the target's position remained constant and target height was varied illustrated the feasibility of using RTI to identify significant target features. It was determined that smooth, higher resolution images achieved by regularization and small voxel sizes would be necessary to achieve accurate feature estimation within specified tolerances. It is also likely that higher node density and link coverage would be necessary. Minimizing multipath from reflections off of the floor would also provide more accurate estimates. A list of recommendations for future research that would be beneficial for both of the research objectives considered in this thesis is featured below.

WSN Self-Localization. In this research, the physical locations of each wireless node were manually set in the data collection program. Determining mote location manually can introduce additional measurement error which can lead to inaccurate estimates as attenuation weighting is dependent on the distance between nodes. Investigating WSN self-localization algorithms that enable motes to determine their respective position based on known locations of a few seed nodes will limit the amount of human induced measurement error, and will present the opportunity to employ ad-hoc networks [15, 23–25, 28].

Optimizing Topology. This research utilized a 3-D network with 80 wireless motes in a 100 sqft area; however, in a real-world application it is more cost effective to employ networks covering larger areas with the fewest number of motes possible, while remaining effective and accurate. Optimizing the network's topology to minimize the number of motes needed to provide effective link coverage will provide more efficient network structures for implementation [1, 67].

Through-wall, Office Environment. The network in this research was employed indoors with very limited furniture obstructions in a 100 sqft area. This is not representative of common office environments which contain considerably more furniture in addition to walls or structural obstructions. Implementing an experimental RTI network in more representative environments will help determine the effects and explore methods to combat those effects.

Multiple Targets. This research used at most two targets. The results showed that introducing a second target resulted in noisier images, and in the experiments where the targets were moving, the second target is often unidentifiable when in-line with the first target. Recommend further research on the impacts of increasing the number of targets tracked within the network, and how to combat any negative effects seen in the imagery [10, 56].

Measurement Model. This research used link RSS measurements on a single channel from each frame of data. Recommend exploring the use of channel diversity and fade-

level in the measurement model to minimize the effect of multipath and possibly improve measurement reliability [17, 56].

Weighting Model. This research used the *Line Model* to determine pixel attenuation weights from link RSS measurements. There are many weighting models presented in the literature that have not been demonstrated in the application of RTI for spatial pattern monitoring. Recommend exploring additional models and comparing the outcomes in a spatial pattern monitoring capacity [11, 17, 27, 51, 54, 55].

Image Estimation and Regularization. This research employed a weighted MLE using *Tikhonov Regularization* with a difference matrix operator to reconstruct the image. There are many possible estimation techniques that exist in the literature in addition to those that have been demonstrated in RTI. Exploring various image estimation and regularization techniques may lead to more accurate RTI-based motion tracking and spatial pattern monitoring systems.

Image De-noising and Obstruction Modeling. This research did not utilize any specific image de-noising techniques. Inaccurate position estimates were identified based on their registered RSS attenuation magnitude in comparison to the maximum attenuation value measured in that data set; however, this is a simple approach. Applying image de-noising and more realistic target obstruction models such as a *Gaussian Filter* will improve localization accuracy and more accurate spatial pattern monitoring results [56].

Kalman Filter Tracking. This research required knowledge about the number of targets present in the network in order to estimate multiple target positions. Implementing estimation techniques to estimate the number of targets present in a network through thresholding and clustering can further automate an RTI system making it more relevant [56]. Tracking multiple, unknown targets in an RTI network using *Kalman Filter* tracking has been shown to improve target tracking and thus could be used to improve the accuracy of spatial pattern monitoring [17, 44, 48, 56].

3-D RTI. This research explored the capabilities of 3-D RTI networks to generate 3-D attenuation image estimates, and to determine the level of fidelity that can be achieved; such as the ability to determine a target height. To date, the demonstration of an RTI network in a 3-D capacity does not exist in the literature. The only research that approaches the subject is [7], which employs an RTI network with two layers of motes in the vertical axis to provide fall-detection. When larger attenuation values are registered in the lower layer of the network, they are attributed to a fallen target. 3-D imagery was not demonstrated. Improving the capabilities of 3-D RTI can lead to higher 3-D image fidelity for possible feature recognition (i.e., target height and size).

Bibliography

- [1] C. Huang and Y. Tseng, "The Coverage Problem in a Wireless Sensor Network," *Mobile Networks and Applications*, vol. 10, no. 4, pp. 519–528, 2005.
- [2] T. Pham, B.M. Sadler, and H. Papadopoulos, "Energy-Based Source Localization via Ad-hoc Acoustic Sensor Network," in *Proc. Workshop on Statistical Signal Processing*. IEEE, 2003, pp. 387–390.
- [3] O. Kaltiokallio and M. Bocca, "Real-Time Intrusion Detection and Tracking in Indoor Environment Through Distributed RSSI Processing," in *Proc. Seventeenth Int'l Conf. on Embedded and Real-Time Computing Systems and Applications (RTCSA)*. IEEE, 2011, vol. 1, pp. 61–70.
- [4] S.F. Midkiff and C.W. Bostian, "Rapidly-Deployable Broadband Wireless Networks for Disaster and Emergency Response," in *Proc. First Workshop on Disaster Recovery Networks (DIREN)*, 2002.
- [5] O. Kaltiokallio, M. Bocca, and N. Patwari, "Enhancing the Accuracy of Radio Tomographic Imaging using Channel Diversity," in *Proc. Ninth Int'l Conf. on Mobile Adhoc and Sensor Systems (MASS)*. IEEE, 2012, pp. 254–262.
- [6] J. Wilson and N. Patwari, "RF Sensor Networks for Device-Free Localization: Measurements, Models, and Algorithms," *Proceedings of the IEEE*, vol. 98, no. 11, pp. 1961–1973, 2010.
- [7] B. Mager, *Fall Detection Using RF Sensor Networks*, Ph.D. thesis, University of Utah, 2013.
- [8] O. Kaltiokallio, M. Bocca, and N. Patwari, "Follow @grandma: Long-Term Device-Free Localization for Residential Monitoring," in *Proc. Thirty-Seventh Conf. on Local Computer Networks Workshops (LCN Workshops)*. IEEE, 2012, pp. 991–998.
- [9] M. Bocca, O. Kaltiokallio, and N. Patwari, "Radio Tomographic Imaging for Ambient Assisted Living," in *Evaluating AAL Systems Through Competitive Benchmarking*, pp. 108–130. Springer, 2013.
- [10] S. Nannuru, Y. Li, M. Coates, and B. Yang, "Multi-Target Device-Free Tracking using Radio Frequency Tomography," in *Proc. Seventh Int'l Conf. on Intelligent Sensors, Sensor Networks and Information Processing (ISSNIP)*. IEEE, 2011, pp. 508–513.
- [11] M. Kanso and M.G. Rabbat, "Efficient Detection and Localization of Assets in Emergency Situations," *Proc. Thirty-Seventh Int'l Sym. Medical Info. Commun. Tech.*, vol. 1, pp. 1, 2009.

- [12] J. Wilson and N. Patwari, "Radio Tomographic Imaging with Wireless Networks," *Transactions on Mobile Computing*, vol. 9, no. 5, pp. 621–632, 2010.
- [13] M. Youssef, M. Mah, and A. Agrawala, "Challenges: Device-Free Passive Localization for Wireless Environments," in *Proc. Thirteenth Int'l Conf. on Mobile Computing and Networking*. ACM, 2007, pp. 222–229.
- [14] D. Zhang, J. Ma, Q. Chen, and L.M. Ni, "An RF-Based System for Tracking Transceiver-Free Objects," in *Proc. Fifth Int'l Conf. on Pervasive Computing and Communications (PerCom)*. IEEE, 2007, pp. 135–144.
- [15] N. Patwari, J.N. Ash, S. Kyperountas, Spyros, A.O. Hero III, R.L. Moses, and N.S. Correal, "Locating the Nodes: Cooperative Localization in Wireless Sensor Networks," *Signal Processing Magazine*, vol. 22, no. 4, pp. 54–69, 2005.
- [16] F. Santos, "Localization in Wireless Sensor Networks," .
- [17] O. Kaltiokallio, M. Bocca, and N. Patwari, "A Fade Level-Based Spatial Model for Radio Tomographic Imaging," *Transactions on Mobile Computing*, vol. PP, no. 99, pp. 1–1, 2013.
- [18] J. Wilson and N. Patwari, "A Fade-Level Skew-Laplace Signal Strength Model for Device-Free Localization with Wireless Networks," *Transactions on Mobile Computing*, vol. 11, no. 6, pp. 947–958, 2012.
- [19] H. Hashemi, "The Indoor Radio Propagation Channel," *Proc. of the IEEE*, vol. 81, no. 7, pp. 943–968, 1993.
- [20] P. Agrawal and N. Patwari, "Correlated Link Shadow Fading in Multi-hop Wireless Networks," *Wireless Communications*, vol. 8, no. 8, pp. 4024–4036, 2009.
- [21] L. Geng, M Bugallo, A. Athalye, and P.M. Djuric, "Indoor Tracking With RFID Systems," *Journal of Selected Topics in Signal Processing: Special Issue on Non-Cooperative Localization Networks*, vol. 8, no. 1, 2014.
- [22] Y. Ji, S. Biaz, S. Wu, and B. Qi, "Impact of Building Environment on the Performance of Dynamic Indoor Localization," in *Proc. Annual Wireless and Microwave Technology Conference (WAMICON)*. IEEE, 2006, pp. 1–5.
- [23] R. Stoleru and J.A. Stankovic, "Probability Grid: A Location Estimation Scheme for Wireless Sensor Networks," in *Proc. First Conf. on Sensor and Ad Hoc Communications and Networks (SECON)*. IEEE, 2004, pp. 430–438.
- [24] H. Wymeersch, J. Lien, and M.Z. Win, "Cooperative Localization in Wireless Networks," *Proc. of the IEEE*, vol. 97, no. 2, pp. 427–450, 2009.
- [25] L. Hu and D. Evans, "Localization for Mobile Sensor Networks," in *Proc. Tenth Int'l Conf. on Mobile Computing and Networking*. ACM, 2004, pp. 45–57.

- [26] D. Niculescu and B. Nath, “DV Based Positioning in Ad-hoc Networks,” *Telecommunication Systems*, vol. 22, no. 1-4, pp. 267–280, 2003.
- [27] Y. Li, X. Chen, M. Coates, and B. Yang, “Sequential Monte Carlo Radio-Frequency Tomographic Tracking,” in *Proc. Int’l Conf. on Acoustics, Speech and Signal Processing (ICASSP)*. IEEE, 2011, pp. 3976–3979.
- [28] G. Mao, B. Fidan, and B. Anderson, “Wireless Sensor Network Localization Techniques,” *Computer networks*, vol. 51, no. 10, pp. 2529–2553, 2007.
- [29] Y. Zhao and N. Patwari, “Robust Estimators for Variance-Based Device-Free Localization and Tracking,” *Submitted for publication*, 2011.
- [30] M. Seifeldin, A. Saeed, A. Kosba, A. El-Keyi, and M. Youssef, “Nuzzer: A Large-Scale Device-Free Passive Localization System for Wireless Environments,” *Transactions on Mobile Computing*, vol. 12, no. 7, pp. 1321–1334, 2012.
- [31] M. Seifeldin and M. Youssef, “A Deterministic Large-Scale Device-Free Passive Localization System For Wireless Environments,” in *Proc. Third Int’l Conf. on Pervasive Technologies Related to Assistive Environments (PETRA)*. ACM, 2010, p. 51.
- [32] Thoma, RS and Hirsch, Ole and Sachs, Jürgen and Zetik, Rudolf, “UWB Sensor Networks for Position Location and Imaging of Objects and Environments,” in *Antennas and Propagation, 2007. EuCAP 2007. The Second European Conference on*. IET, 2007, pp. 1–9.
- [33] Y. Kilic, H. Wymeersch, A. Meijerink, M.J. Benthum, and W.G. Scanlon, “Device-Free Person Detection and Ranging in UWB Networks,” *Journal of Selected Topics in Signal Processing: Special Issue on Non-Cooperative Localization Networks*, vol. 8, no. 1, 2014.
- [34] C. Chang and A. Sahai, “Object Tracking In a 2D UWB Sensor Network,” in *Proc. Thirty-Eighth Conf. on Signals, Systems and Computers*. IEEE, 2004, vol. 1, pp. 1252–1256.
- [35] B. Sobhani, E. Paolini, A. Giorgetti, M. Mazzotti, and M. Chiani, “Target Tracking for UWB Multistatic Radar Sensor Networks,” *Journal of Selected Topics in Signal Processing: Special Issue on Non-Cooperative Localization Networks*, vol. 8, no. 1, 2014.
- [36] J.J. Robles, M. Deicke, and R. Lehnert, “3D Fingerprint-Based Localization for Wireless Sensor Networks,” in *Proc. Seventh Workshop Positioning Navigation and Communication (WPNC)*. IEEE, 2010, pp. 77–85.
- [37] N. Swangmuang and P. Krishnamurthy, “An Effective Location Fingerprint Model for Wireless Indoor Localization,” vol. 4, no. 6, pp. 836–850, 2008.

- [38] A.K.M.M. Hossain, H.N. Van, Y. Jin, and W. Soh, "Indoor Localization using Multiple Wireless Technologies," in *Proc. Int'l Conf. on Mobile Adhoc and Sensor Systems (MASS)*. IEEE, 2007, pp. 1–8.
- [39] P. Mirowski, H. Steck, P. Whiting, R. Palaniappan, M. MacDonald, and T.K. Ho, "KL-Divergence Kernel Regression for Non-Gaussian Fingerprint Based Localization," in *Proc. Int'l Conf. on Indoor Positioning and Indoor Navigation (IPIN)*. IEEE, 2011, pp. 1–10.
- [40] F. Viani, L. Lizzi, P. Rocca, M. Benedetti, M. Donelli, and A. Massa, "Object Tracking Through RSSI Measurements in Wireless Sensor Networks," *Electronics Letters*, vol. 44, no. 10, pp. 653–654, 2008.
- [41] G. Oliveri D. Trinchero F. Viani, P. Rocca and A. Massa, "Localization, Tracking, and Imaging of Targets in Wireless Sensor Networks: An Invited Review," *Radio Science*, vol. 46, no. 5, pp. RS5002, 2011.
- [42] H.D. Griffiths and C.J. Baker, "Fundamentals of Tomography and Radar," in *Advances in Sensing with Security Applications*, pp. 171–187. Springer, 2006.
- [43] N. Patwari and P. Agrawal, "Effects of Correlated Shadowing: Connectivity, Localization, and RF Tomography," in *Proc. Int'l Conf. on Information Processing in Sensor Networks (IPSN)*. IEEE, 2008, pp. 82–93.
- [44] J. Wilson and N. Patwari, "See-Through Walls: Motion Tracking using Variance-Based Radio Tomography Networks," *Transactions on Mobile Computing*, vol. 10, no. 5, pp. 612–621, 2011.
- [45] J. Wilson and N. Patwari, "Through-Wall Tracking Using Variance-Based Radio Tomography Networks," *submitted for publication*, 2009.
- [46] C.R. Anderson, R.K. Martin, T.O. Walker, and R.W. Thomas, "Radio Tomography for Roadside Surveillance," *Journal of Selected Topics in Signal Processing: Special Issue on Non-Cooperative Localization Networks*, vol. 8, no. 1, 2014.
- [47] N. Patwari and P. Agrawal, "NeSh: A Joint Shadowing Model for Links in a Multi-hop Network," in *Proc. Int'l Conf. on Acoustics, Speech and Signal Processing (ICASSP)*. IEEE, 2008, pp. 2873–2876.
- [48] Y. Zhao and N. Patwari, "Noise Reduction for Variance-Based Device-Free Localization and Tracking," in *Proc. Eighth Conf. on Sensor, Mesh and Ad Hoc Communications and Networks (SECON)*. IEEE, 2011, pp. 179–187.
- [49] R.K. Martin, C. Anderson, R.W. Thomas, and A.S. King, "Modelling and Analysis of Radio Tomography," in *Proc. Fourth Int'l Workshop on Computational Advances in Multi-Sensor Adaptive Processing (CAMSAP)*. IEEE, 2011, pp. 377–380.

- [50] R.K. Martin, A. Folkerts, and T. Heinl, “Accuracy vs. Resolution in Radio Tomography,” in *IEEE Signal Process. Lett. submitted for publication*, Sep. 2012.
- [51] M.A. Kanso and M.G. Rabbat, “Compressed RF Tomography for Wireless Sensor Networks: Centralized and Decentralized Approaches,” in *Proc. Fifth Int’l Conf. on Distributed Computing in Sensor Systems (DCOSS)*, pp. 173–186. Springer, 2009.
- [52] Y. Mostofi and A. Gonzalez-Ruiz, “Compressive Cooperative Obstacle Mapping in Mobile Networks,” in *Proc. Conf. on Military Communications (MILCOM)*. IEEE, 2010, pp. 524–530.
- [53] Y. Mostofi, “Compressive cooperative sensing and mapping in mobile networks,” *Transactions on Mobile Computing*, vol. 10, no. 12, pp. 1769–1784, 2011.
- [54] B.R. Hamilton, “Applications of Bayesian Filtering in Wireless Networks: Clock Synchronization, Localization, and RF Tomography,” *Ph.D. Dissertation*, 2012.
- [55] B.R. Hamilton, X. Ma, B.J. Baxley, and S.M. Matechik, “Propagation Modeling for Radio Frequency Tomography in Wireless Networks,” *Journal of Selected Topics in Signal Processing: Special Issue on Non-Cooperative Localization Networks*, vol. 8, no. 1, 2014.
- [56] M. Bocca, O. Kaltiokallio, N. Patwari, and S. Venkatasubramanian, “Multiple Target Tracking with RF Sensor Networks,” *Transactions on Mobile Computing*, 2013.
- [57] M. Bocca, A. Luong, N. Patwari, and T. Schmid, “Dial It In: Rotating RF Sensors to Enhance Radio Tomography,” 2013.
- [58] J. Wilson, N. Patwari, and F.G. Vasquez, “Regularization Methods for Radio Tomographic Imaging,” in *Proc. Virginia Tech Symposium on Wireless Personal Communications*, 2009.
- [59] S. Kabanikhin, “Definitions and Examples of Inverse and Ill-posed Problems,” *Journal of Inverse and Ill-Posed Problems*, vol. 16, no. 4, pp. 317–357, 2008.
- [60] A. Ribes and F. Schmitt, “Linear Inverse Problems in Imaging,” *Signal Processing Magazine*, vol. 25, no. 4, pp. 84–99, July 2008.
- [61] R. Sundaram, R.K. Martin, and C. Anderson, “Regularization in Radio Tomographic Imaging,” in *Proc. Eighth Conf. on Wireless Sensing, Localization, and Processing*. International Society for Optics and Photonics, 2013, vol. 8753.
- [62] Memsic Technologies, “TelosB TPR2420 Mote Platform Datasheet,” Webpage, http://www.memsic.com/userfiles/files/Datasheets/WSN/telosb_datasheet.pdf, 2013.
- [63] Y. Selkowitz et al C. Fylor, C. Vinschen, “Cygwin Project Home Page,” Webpage, <http://www.cygwin.com/>, 2013.

- [64] Stanford Research Community, “TinyOS Home Page,” Webpage, <http://www.tinyos.net>, 2007-13.
- [65] Neal Patwari; University of Utah, “SPAN Home Page,” Webpage, <http://span.ece.utah.edu>, 2013.
- [66] Texas Instruments, “CC2420 Inverted F Antenna Design Note DN0007,” Webpage, <http://www.ti.com/lit/an/swru120b/swru120b.pdf>, 2008.
- [67] F. Pedraza, A.L. Medaglia, and A. Garcia, “Efficient Coverage Algorithms for Wireless Sensor Networks,” in *Proc. Systems and Information Engineering Design Symposium*. IEEE, April 2006, pp. 78–83.

REPORT DOCUMENTATION PAGE					Form Approved OMB No. 0704-0188	
The public reporting burden for this collection of information is estimated to average 1 hour per response, including the time for reviewing instructions, searching existing data sources, gathering and maintaining the data needed, and completing and reviewing the collection of information. Send comments regarding this burden estimate or any other aspect of this collection of information, including suggestions for reducing this burden to Department of Defense, Washington Headquarters Services, Directorate for Information Operations and Reports (0704-0188), 1215 Jefferson Davis Highway, Suite 1204, Arlington, VA 22202-4302. Respondents should be aware that notwithstanding any other provision of law, no person shall be subject to any penalty for failing to comply with a collection of information if it does not display a currently valid OMB control number. PLEASE DO NOT RETURN YOUR FORM TO THE ABOVE ADDRESS.						
1. REPORT DATE (DD-MM-YYYY) 27-03-2014		2. REPORT TYPE Master's Thesis			3. DATES COVERED (From — To) Aug 2012–Mar 2014	
4. TITLE AND SUBTITLE Identifying High-Traffic Patterns in the Workplace With Radio Tomographic Imaging in 3D Wireless Sensor Networks					5a. CONTRACT NUMBER 5b. GRANT NUMBER 5c. PROGRAM ELEMENT NUMBER 5d. PROJECT NUMBER 5e. TASK NUMBER 5f. WORK UNIT NUMBER 	
6. AUTHOR(S) Danella, Thea S., Captain, USAF					8. PERFORMING ORGANIZATION REPORT NUMBER AFIT-ENG-14-M-24	
7. PERFORMING ORGANIZATION NAME(S) AND ADDRESS(ES) Air Force Institute of Technology Graduate School of Engineering and Management (AFIT/EN) 2950 Hobson Way WPAFB, OH 45433-7765					10. SPONSOR/MONITOR'S ACRONYM(S) Air Force office of Scientific Research (AFOSR)/RTC 11. SPONSOR/MONITOR'S REPORT NUMBER(S)	
9. SPONSORING / MONITORING AGENCY NAME(S) AND ADDRESS(ES) AFOSR (Attn: Dr. Tristan Nguyen, AFOSR/RTC) Comm. Phone: (703) 696-7796 / DSN: 426-7796 / Fax: (703) 696-7360 Email: tristan.nguyen@afosr.af.mil 875 North Randolph Street, Suite 325, Room 3112, Arlington, VA 22203-1768					12. DISTRIBUTION / AVAILABILITY STATEMENT DISTRIBUTION STATEMENT A: APPROVED FOR PUBLIC RELEASE; DISTRIBUTION UNLIMITED	
13. SUPPLEMENTARY NOTES This material is declared a work of the U.S. Government and is not subject to copyright protection in the United States.						
14. ABSTRACT The rapid progress of wireless communication and embedded micro-sensing electro-mechanical systems (MEMS) technologies has resulted in a growing confidence in the use of wireless sensor networks (WSNs) comprised of low-cost, low-power devices performing various monitoring tasks. Radio Tomographic Imaging (RTI) is a technology for localizing, tracking, and imaging device-free objects in a WSN using the change in received signal strength (RSS) of the radio links the object is obstructing. This thesis employs an experimental indoor three-dimensional (3-D) RTI network constructed of 80 wireless radios in a 100 square foot area. Experimental results are presented from a series of stationary target localization and target tracking experiments using one and two targets. Preliminary results demonstrate a 3-D RTI network can be effectively used to generate 3-D RSS-based images to extract target features such as size and height, and identify high-traffic patterns in the workplace by tracking asset movement.						
15. SUBJECT TERMS Radio Tomographic Imaging, RTI, wireless sensor network, localization, RSS, DFL, RF, spatial pattern, WSN, passive						
16. SECURITY CLASSIFICATION OF:			17. LIMITATION OF ABSTRACT		18. NUMBER OF PAGES	
a. REPORT	b. ABSTRACT	c. THIS PAGE	UU		151	
U	U	U	19a. NAME OF RESPONSIBLE PERSON Dr. Richard K. Martin (ENG)			
						19b. TELEPHONE NUMBER (include area code) (937) 255-3636 x4625 richard.martin@afit.edu